

The Pennsylvania State University

The Graduate School

College of Engineering

**TIME VARIATION OF SHEAR STRESS
MEASUREMENTS AT THE BASE
OF RECTANGULAR PIERS**

A Thesis in

Civil Engineering

by

Michael W. Horst

Copyright 2004 Michael W. Horst

Submitted in Partial Fulfillment
of the Requirements
for the Degree of

Doctor of Philosophy

August 2004

The thesis of Michael W. Horst has been reviewed and approved* by the following:

Arthur C. Miller
Professor of Civil Engineering
Thesis Advisor
Chair of Committee

David F. Hill
Assistant Professor of Civil Engineering

Peggy A. Johnson
Professor of Civil Engineering

Virendra M. Puri
Professor of Agricultural Engineering

Kornel Kerenyi
Applied Hydraulics Researcher
Federal Highway Administration
Special Member

Andrew Scanlon
Professor of Civil Engineering
Head of the Department of Civil and Environmental Engineering

* Signatures are on file in the Graduate School

ABSTRACT

Time variations of shear stress measurements have been made at the base of a rectangular pier for the purpose of ascertaining a better understanding of the local scouring phenomenon. Measurements were made using a force-displacement sensor which was mounted vertically and placed flush with the channel bottom. Statistical analysis of the data shows the horseshoe vortex, previously shown to be present, to be oscillatory in nature. Peak shear measurements vary from 2.5 to 4 times the approach flow undisturbed shear value. Average shear intensities vary from 1.5 to 4 times the approach flow value. The duration during which a clump of shear values exceeded the approach value was computed and showed to range from 1 to 3 seconds, with longer durations found for smaller Froude numbers. The probabilities that the pier-induced shear values will exceed the approach flow shear value and the time percentage of exceedence are both 100 percent, indicating a constant presence of the vortex. A wide pier phenomenon which results in the vortex system not fully developing is observed once the depth of flow to pier width ratio falls below 0.6. The overall results of the study show the scouring mechanism can not be initiated solely by increases of shear stress on the channel bottom due to the vortex. Instead, scour most likely is initiated by a combination of a downward flow component reflecting off the pier, normally impacting the channel bottom which reduces the pressure field holding the particles in place, and an increase in shear stress felt on the channel bottom due to the formation of a set of vortices known as the horseshoe vortex system.

TABLE OF CONTENTS

	<u>Page</u>
LIST OF TABLES	vi
LIST OF FIGURES	vii
ACKNOWLEDGMENTS	x
Chapter 1 INTRODUCTION	1
1.1 Importance of the Problem	1
Chapter 2 REVIEW OF LITERATURE	5
2.1 Definition of Scour	5
2.2 History of Scour Studies.....	5
2.3 Flow Field Around a Scour Hole	10
2.4 Numerical Model Simulations	18
2.5 Local Scour Predictions	22
Chapter 3 HYPOTHESIS	25
3.1 Statement of Problem	25
3.2 Hypothesis	28
3.3 Hypothesis Verification.....	29
Chapter 4 EXPERIMENTAL SETUP	30
4.1 Experimental Equipment	30
Chapter 5 IDENTIFICATION OF FLUID FORCES	36
5.1 Initial Offset Adjustment	36
5.2 Dynamic Calibration	39
5.2.1 Determination of Dynamic Properties	44
5.2.1.1 Stiffness/Damping.....	44
5.2.1.2 Natural Frequency/Mass.....	49
Chapter 6 DATA COLLECTION	52
6.1 Autocorrelation Function/Correlation Length.....	52
6.2 Data Collection Procedure	54
6.3 Data Collection Errors	55
6.3.1 Equipment Error.....	56
Chapter 7 UNOBSTRUCTED FLOW.....	58
7.1 Results	58
7.2 Analysis	60
7.2.1 Comparison to Theoretical Predictions	64

Chapter 8	OBSTRUCTED FLOW	69
8.1	Pier Size	69
8.2	Shear Threshold	70
8.3	Shear Measurements.....	71
8.4	Level Crossing Statistics	72
8.4.1	Spectral Density Function/Frequency Content	73
8.4.1.1	Analysis	75
8.4.2	Probability of Exceedence.....	78
8.4.2.1	Analysis	81
8.4.3	Percent of Time Threshold is Exceeded	84
8.4.3.1	Analysis	86
8.4.4	Mean Clump Time.....	87
8.4.4.1	Analysis	88
8.5	Shear Amplification	89
8.5.1	Analysis.....	95
8.5.2	Shear Amplification – Sensor Offset Adjustment	96
8.5.2.1	Analysis	100
8.5.3	Comparison to Historical Results	100
8.5.3.1	Melville and Raudkivi (1977).....	100
8.5.3.2	Mendoza-Cabralles (1993)	103
8.5.3.3	Ahmed and Rajaratnam (1998).....	104
8.5.3.4	Ali and Karim (2002)	105
8.5.3.5	Jones (2002).....	106
8.6	Discussion of Results.....	108
Chapter 9	CONCLUSIONS	113
9.1	Unobstructed Flow/Shear Sensor	113
9.2	Obstructed Flow	114
9.3	Engineering Significance/Recommendations	116
9.4	Future Work	117
	REFERENCES	119
	APPENDIX A – Unobstructed Flow Summary Tables	127
	APPENDIX B – Obstructed Flow Summary Tables	132

LIST OF TABLES

	<u>Page</u>	
Table 5.1	Depth of flow vs. voltage – Calibration data	38
Table 5.2	Shear vs. voltage – In-air stiffness determination data.....	46
Table 5.3	Shear vs. voltage – Aquatic stiffness determination data.....	48
Table 7.1	Unobstructed flow results	58
Table 7.2	Hydraulic parameters used for shear stress predictions	67
Table 8.1	Obstructed flow hydraulic conditions with time percentage of threshold exceedence	85
Table 8.2	Peak shear and average intensity shear amplifications with corresponding uncertainties.....	94
Table 8.3	Adjusted threshold, peak, and average intensity shear values	98
Table 8.4	Adjusted peak shear and average intensity shear Amplification with corresponding uncertainty	99

LIST OF FIGURES

	<u>Page</u>	
Figure 2.1	Representation of the three vortex systems which form around a pier	6
Figure 2.2	Typical scour hole profile depicting the formation of the three slopes which form in the scour hole as well as the groove generated by the diving current	8
Figure 2.3	Representation of the mechanisms responsible for the development of a scour hole	11
Figure 4.1	Shear stress measuring device	30
Figure 4.2	Flume support structure	32
Figure 4.3	Tank/pump/motor controller/support dolly	33
Figure 4.4	Carriage system used to house velocity probe	34
Figure 4.5	Experimental setup showing tank/pump/motor controller/flume/carriage system	35
Figure 5.1	Aluminum rod protruding from top of sensor	36
Figure 5.2	Rubber membrane located at base of well in sensor	37
Figure 5.3	Calibration curve with corresponding best fit equation used to adjust voltage signal offset caused by weight of water displacing sensor rod	39
Figure 5.4	Graphical representation of shear sensor plate with pivoting rod and associated stiffness and damping	40
Figure 5.5	Variation of dynamic amplification factor with frequency	41
Figure 5.6	Flow chart depicting procedure used for determining force delivered by flow to sensor	43
Figure 5.7	Phillips frequency converter used to capture voltage signal delivered by shear sensor	44
Figure 5.8	Static calibration technique using known vertical forces and moment arm lengths to determine tangential forces	45
Figure 5.9	Determination of stiffness of sensor by exposure to tangential shearing forces in air	46
Figure 5.10	Schematic of calibration weight/measuring plate used for stiffness determination under aquatic conditions	48
Figure 5.11	Determination of stiffness of sensor when exposed to tangential shearing forces in water	49
Figure 5.12	Typical response of flow induced structure in frequency domain depicting peak amplitude at natural frequency of the structure	50
Figure 5.13	Amplitude spectrum of response measurements of sensor at various flow depths, showing a natural frequency of 9.0 Hz	51
Figure 6.1	Autocorrelation function of test run with highest variance used to determine minimum sampling frequency	53

Page

Figure 7.1	Graphical display of results of shear vs. Froude number with corresponding error bars obtained from the unobstructed flow analysis	60
Figure 7.2	Standard deviation of shear values vs. depth of flow for unobstructed flow trials	62
Figure 7.3	Variation of depth with Froude number showing depths of flow less than 1 Inch for Froude numbers > 0.52	63
Figure 7.4	Predicted shear from Equations (10) and (14) plus measured shear from sensor vs. Froude number	63
Figure 7.5	Comparison of predicted shear values from Equations (10) and (14) to shear measured from sensor, with a hypothetical increase in shear of 0.20 Pa added to each theoretical equation	68
Figure 8.1	Graphical depiction of flow fields with (a) no side-wall contraction effects and (b) side-wall contraction effects	69
Figure 8.2	Graph and corresponding best fit trend line with equation and R^2 showing data used from Chapter 7 in order to determine a shear threshold used for statistical analysis	70
Figure 8.3	Typical time variation of shear stress in front of pier	71
Figure 8.4	Frequency content from each data set vs. approach flow Froude number	74
Figure 8.5	(a) Hypothetical depiction of the vortex at the base of a pier oscillating back and forth and never shedding downstream; (b) associated time variation of shear stress due to vortex as read by sensor resulting in a frequency content of 0	76
Figure 8.6	(a) Hypothetical depiction of the diving current and a quasi-periodic vortex at the base of a pier moving upstream then shedding downstream; (b) associated time variation of shear stress due to diving current and vortex, as read by shear sensor, resulting in a frequency content greater than 0 but less than 1	76
Figure 8.7	(a) Hypothetical depiction of the diving current and vortex not felt on the channel bottom thereby not leading to any significant variation in shear stress with time; (b) associated time variation of shear stress as read by shear sensor, resulting in a frequency content of 1	77
Figure 8.8	Histogram of a representative data set showing a typical normal distribution with corresponding mean and standard deviation	79
Figure 8.9	Probability that a single shear measurement from each data set will exceed the approach flow shear threshold	81

Figure 8.10	Probability that a single shear measurement will exceed the approach flow shear threshold as a function of depth	82
Figure 8.11	Probability of exceedence of one measurement exceeding the threshold as a function of the length ratio of depth of flow to pier width, showing the presence of the wide pier phenomenon to occur at $Y/B < 0.6$	83
Figure 8.12	The percentage of time that the approach flow shear stress threshold was exceeded during each experiment as a function of the approach flow Froude number	86
Figure 8.13	Typical data set showing how the total average duration of a clump of measurements above the threshold was obtained	87
Figure 8.14	Average duration of all clumps from each individual experiment as a function of the approach flow Froude number	88
Figure 8.15	Hypothetical schematic of the variation of shear stress with time showing the differences between peak shear, average shear intensity, shear fluctuation above the threshold and shear threshold	91
Figure 8.16	Visual representation of method used to determine the typical peak shear for each trial	91
Figure 8.17	Typical peak shear amplification and average shear intensity amplification of each trial as a function of the approach flow Froude number	92
Figure 8.18	Average shear intensity amplification with corresponding uncertainty	93
Figure 8.19	Peak shear amplification with corresponding uncertainty	93
Figure 8.20	Adjusted average shear intensity amplification with corresponding uncertainty	97
Figure 8.21	Adjusted peak shear amplification with corresponding uncertainty	97
Figure 8.22	Developing velocity profile due to the formation and oscillation of a vortex	103

ACKNOWLEDGMENTS

A great many individuals have given both help and support towards the completion of this research project. I would like to express my sincere appreciation to all those involved. In particular I would like to thank my committee members for their suggestions and guidance, the machine shop personnel at the Federal Highway Administration (Bill and Dave) for their mechanical expertise and help in constructing necessary laboratory equipment, and Holger Dauster for his expertise in data acquisition and computer programming.

A special thank you goes to Kornel Kerenyi for his insightful suggestions and genuine desire to have me succeed and accomplish this goal, as well as to Sterling Jones for his financial support and allowing me to complete my experiments in his lab at the Federal Highway Administrations' hydraulics research lab.

Finally, I would like to offer my sincerest appreciation to Dr. Arthur C. Miller, my academic advisor and friend. Dr. Miller has been a shining example of what all teachers should strive to become. Through his guidance, mentorship and influence I feel that I have become a better person. Additionally, many of my future goals can be directly attributed to the impact which he has had on my life.

This work is dedicated to my family, in particular my mother and sister, for their never-ending support and dedication in helping me to succeed and accomplish my goals.

CHAPTER 1

INTRODUCTION

1.1 Importance of the Problem

Bridges provide a necessary means of vehicle transport for our fast-growing societies. Therefore, proper design for both structural and hydraulic considerations is essential to maintain safety. While structural analysis and design of bridges are well understood, the uncertainties of hydraulic predictions often lead to over-design resulting in additional costs, or under-design and possibly failure.

As of 1995 it was estimated that approximately 84 percent of the 575,000 bridges in the National Bridge Inventory are built over waterways (Richardson et al. 1995). Of these bridges, approximately 121,000 are considered to be scour susceptible and of those 121,000, approximately 13,000 are considered to be scour critical (Jones 1993). A study completed by the Transportation Research Board in 1984 estimates that an average of 150 bridges in the United States fail each year due to sediment transport and local scouring of piers or abutments (Davis 1984).

Between the years 1985 and 1987, a total of 90 bridges were destroyed in New York, Pennsylvania, Virginia and West Virginia due to either pier or abutment failure. In 1994 the state of Georgia experienced over 500 bridge failures due to scour caused by Hurricane Alberto (Jones 2002).

On April 5, 1987, the potential problems associated with pier scour received national awareness when two spans of the New York State Thruway

(I-90) bridge over the Schoharie Creek fell about 80 feet into the creek after a pier, which partially supported two spans of roadway decking, collapsed. Ninety minutes after the initial collapse, a second pier failed and a third span collapsed. Four passenger cars and one tractor-semi-trailer plunged into the creek, and 10 people were killed (NTSB 1987). An evaluation of the collapse conducted by the National Transportation Safety Board (NTSB) revealed that the failure most likely was due to scouring at the footing of the pier. As a result of this catastrophe, the Federal Highway Administration was commissioned to develop a set of guidelines and protocol for evaluating the susceptibility of bridges for all types of bridge scour, specifically natural degradation of the stream, contraction scour, local scour at piers and abutments, and lateral stream migration. The result of this study was the Federal Highway Administration's Hydraulic Engineering Circular No. 18, "Evaluating Scour at Bridges" (Richardson et al. 1995).

Other major catastrophes due to pier scour in the U.S. include (Jones 2002): Cardova Street Bridge over the Santa Cruz River in Phoenix, Arizona in 1985 – 0 fatalities; Walker Bridge over Hatchie River near Memphis, Tennessee in 1989 – 8 fatalities; and I-5 over Los Gatos Creek near Coalinga, CA in 1995 – 7 fatalities. In addition to loss of life, Brice and Blodgett (1978) reported that the cost of scour damage to bridges and highways from some regional floods was up to \$100 million per event.

It is apparent that failures of bridges have brought significant life and financial losses. To ensure public safety and minimize the losses of bridge failures, more extensive studies on scour at bridge crossings are necessary. In

particular, comprehensive studies deciphering the mechanisms themselves which initiate scour should be at the forefront of any current or future research. Until these initiating mechanisms are well understood, the potential for scour around bridge support structures could prove to be a major concern for bridge design engineers.

The following chapters contain the details of a series of experiments conducted for the purpose of obtaining a better understanding of the scouring mechanism. Specifically:

- Chapter 2 presents a literature review of investigations pertaining to the scour problem, both experimental and numerical;
- Chapter 3 defines the objective and underlying hypothesis of this work;
- Chapter 4 discusses the experimental equipment used as well as the laboratory setup;
- Chapter 5 gives a detailed explanation of the procedure used to identify the fluid forces creating displacements of the shear sensor;
- Chapter 6 involves data collection procedures and error sources;
- Chapter 7 presents the baseline shear measurements obtained from an unobstructed flow as well as how the sensor performs when compared to two theoretical equations;
- Chapter 8 presents the results and discusses the shear measurements taken in front of the pier and how they compare to

the baseline results from Chapter 7, as well as historical measurements presented in the literature;

- Chapter 9 lists conclusions drawn from this work as well as future research needs.

CHAPTER 2

REVIEW OF LITERATURE

2.1 Definition of Scour

Water flow in a channel has the capability to transport sediments. While scour occurs naturally in erodible streams, the existence of an obstruction increases the potential of scour. As concluded in HEC-18 (Richardson et al. 1995), total scour at a highway crossing is comprised of three components: (a) long-term aggradation and degradation, (b) contraction scour, and (c) local scour. Long-term aggradation and degradation are due to natural or man-induced causes such as dams, reservoirs, changes in watershed land use, channelization, and cutoffs of meander bends. Contraction scour occurs when the flow area is constricted by a bridge or other natural causes. Reduction in flow area directly results in increasing flow velocity and bed shear stress through the contraction. Contraction scour can be either clear-water or live-bed, as defined in Section 2.2. Local scour is observed at the boundary where the structure meets the channel bottom. It is caused by an acceleration of flow and resulting vortices induced by the flow obstruction. Local scour also can be either clear-water or live-bed.

2.2 History of Scour Studies

Yarnell and Nagler (1931) were among the first researchers to study the causes of pier scour. Their analysis showed that the depth of pier scour was directly related to the size and location of the pier itself, leading them to believe

that it was the pier acting as an obstruction in the flow path which caused scour to begin. Yarnell and Nagler's experiments dealt with the shape of the pier, as well as the effects which different sizes and geometries have on the maximum depth of scour. They found that for large blunt-shaped piers, the maximum depth of scour occurred at the upstream face of the pier, whereas for sharp-nosed piers, the maximum scour depth appeared at the downstream face.

Shen et al. (1969) found three types of vortex systems which can lead to scour: trailing, horseshoe, and wake vortex systems (Figure 2.1).

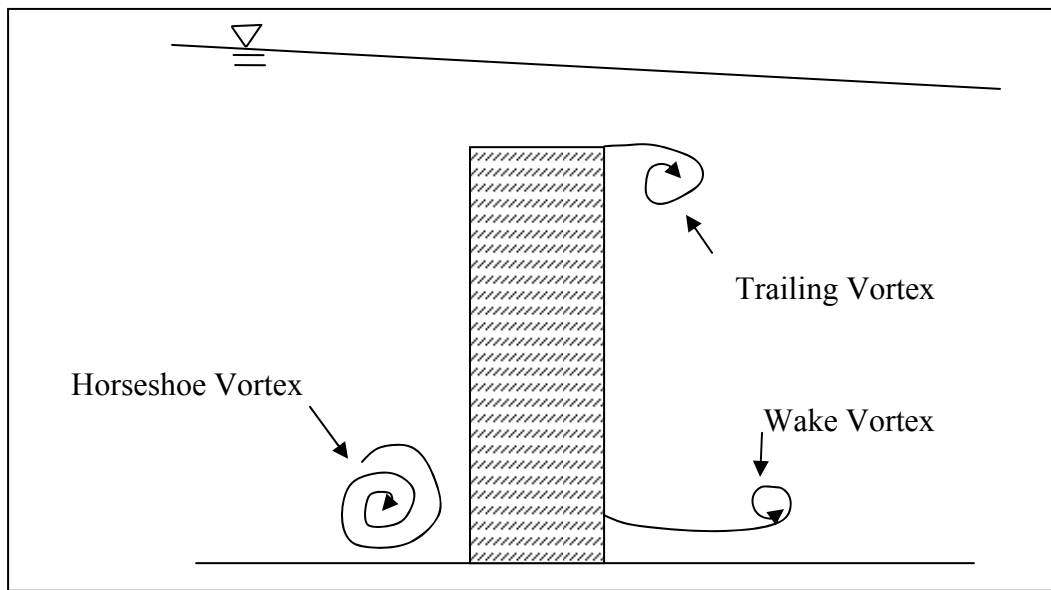


Figure 2.1 – Representation of the three vortex systems which form around a pier

The trailing vortex system usually occurs on completely submerged piers and is thought to have little effect on creating scour. The horseshoe vortex system triggers the scouring process by trapping sediment dislodged from the

bed by a downward flow reflecting off the pier. The wake vortex system acts like a vacuum cleaner in transporting bed material initially scoured by the horseshoe vortex system. The material is carried downstream, usually as suspended sediment, by eddies shedding from the pier.

Raudkivi and Ettema (1983) performed experiments to study the effects of sediment grading, time, relative grain size, flow depth, and pier size on the equilibrium scour depth. They found that for non-uniform sediment gradations, an armor layer will develop which impedes the scour hole development. The time development of the scour hole undergoes three phases. Initially, scour commences due to the downflow of water reflecting off the pier. This produces rapid scouring. At an intermediate phase, the horseshoe vortex which settles into the scour hole dominates the dislodging of bed particles and transports them downstream. The third phase is characterized by full development of the scour hole. Their analysis also showed that as the particle size distribution increases, the effects of the horseshoe vortex diminish and scour is caused mainly by the downflow. The relative effect of grain size is based on the ratio of the pier width (D) to the median grain size diameter (d_{50}) as follows:

- 1) $D/d_{50} \geq 130$, the sediment is entrained from the groove (Figure 2.2) by the downflow and from the slope of the horseshoe vortex until equilibrium is reached;
- 2) $130 > D/d_{50} \geq 30$, the sediment is entrained mainly from the groove with only a limited entrainment under the horseshoe vortex;

- 3) $30 > D/d_{50} \geq 8$, the effects of the horseshoe vortex disappear and scour is due to the downflow;
- 4) $D/d_{50} < 8$, the sediment is so large that erosion does not occur.

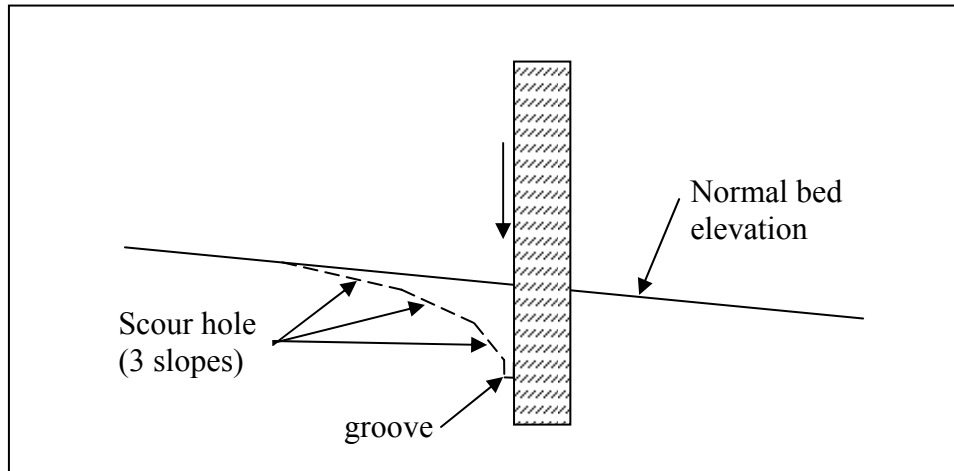


Figure 2.2 – Typical scour hole profile depicting the formation of the three slopes which form in the scour hole as well as the groove generated by the diving current

Dargahi (1990) provided a graphical representation of the developing vortices and resulting scour hole. He found that scour initially begins at the sides of the pier due to the wake vortex development and then quickly moves (experimental time scale – 20 seconds) to the front face of the pier once the horseshoe vortex system fully develops. At its completion, the scour hole exhibits three main slopes (Figure 2.2), with the deepest slope being equal to the angle of repose of the sediment. From his analysis, Dargahi concluded that scour at the upstream face of an object is caused by the following factors:

- 1) the rotational velocity and fluctuating movement of the vortices;

- 2) the impact of high-momentum fluid induced by the downflow on the bed material, which reduces the local pressure around the sediment particles and thereby ejects them from the bed;
- 3) the high turbulence level associated with the horseshoe vortices making the scour phenomenon quasi periodical.

Johnson (1995) compared seven commonly used bridge pier scour equations using a large set of field data for both live-bed and clear-water conditions. She concluded that while the CSU equation best envelops the predicted scour depths compared to the observed depths, no one equation yields consistently good results. Additionally, she stated that further research is needed for cases in which the approach velocity is at or near critical velocity, as well as for wide piers in relatively shallow water.

Briaud et al. (1999) reported that the depth of maximum scour, for a given approach velocity, is a constant and is independent of bed material. The rate at which the scour hole reaches its ultimate depth is drastically different based on material size, but the final depth is the same. Li et al. (2002) analyzed the work of Briaud et al. (1999) from a shear stress approach. They combined maximum scour depth results from experimental studies with maximum shear stress values from numerical simulations, in order to simulate a time history of scour development. Li et al. found that the shape of the shear stress decay model has a reverse curvature with depth. Accordingly, they argued that the work of Briaud et al. was inconsistent with their findings and that different soils will have different depths of maximum scour at the same approach velocity.

Ansari et al. (2002) developed a mathematical model to predict the temporal variation of scour depths in cohesive sediments. The model was based on one previously used by Kothyari et al. (1992) for cohesion-less sediments. Ansari et al. calculated coefficients for their equations through data analysis of laboratory experiments. They found that the location of maximum scour is dependent on the clay and moisture content of the soil before scouring begins. For soils with high moisture or high clay content, maximum scour occurs at the sides of the pier, where Ansari et al. believed the bed shear stress to be 10 times the approach flow shear stress. For lower moisture content or clay content soils, maximum scour occurred at the pier nose due mainly to a combination of the downflow and horseshoe vortex. Ansari et al. believed that the bed shear stress at the pier nose was four times the approach flow shear stress.

2.3 Flow Field Around a Scour Hole

The flow field in the vicinity of a blunt-nosed vertical obstruction is complicated and dominated by a system of vortices. Much research has attempted to ascertain a complete understanding of the mechanisms which lead to the system of vortices. Some of the more prominent contributions made by various investigators are discussed below.

Shen et al. (1966a) performed an extensive analysis of the mechanisms which lead to pier scour at a blunt-nosed pier. They concluded that an adverse pressure gradient is created at the pier which in turn causes a three-dimensional separation of the boundary layer. A stagnation point occurs at approximately

three-quarters the depth of the pier, above which the water has zero velocity. Below the stagnation point, a strong downward flow is produced. The downflow is thought to have a velocity equal in magnitude to the approach velocity. Once the downflow impacts the channel bed, it rolls back onto itself, forming a vortex. The vortex is forced in an upstream direction due to the momentum of the downflow, and is eventually turned around to the normal direction of flow once the momentum of the normal flow is sufficiently strong to overcome the downflow momentum (Figure 2.3). The vortex then sheds from either side of the pier to form the horseshoe vortex system.

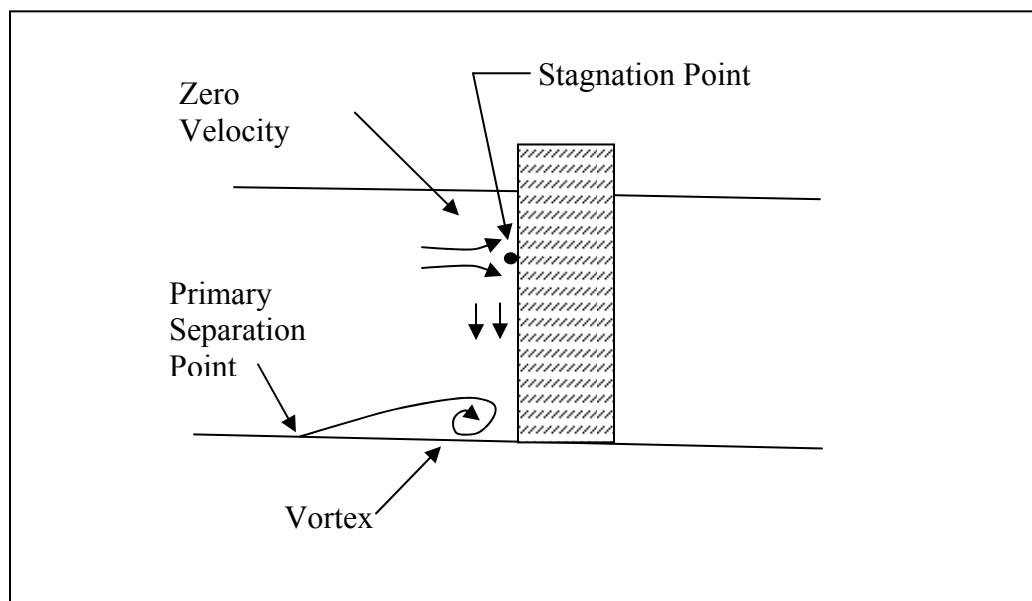


Figure 2.3 – Representation of the mechanisms responsible for the development of a scour hole

Shen et al. (1966a) also analyzed the mechanics of the vortex and concluded that it is the pier acting as an obstruction which concentrates the vorticity already present in the flow. Upon presenting an extensive mathematical

analysis, they stated that the horseshoe vortex can be considered to possess a core which rotates as a rigid body. Additionally, they showed that the strength of the vortex core is proportional to the pier Reynolds number. Finally, through experimental analysis, Shen et al. confirmed that the primary vortex is unsteady and moves up the scoured slope while its rotational velocity increases, and eventually sheds downstream.

Melville and Raudkivi (1977) presented results of the flow field, turbulence intensity distributions and boundary shear stresses in the scour zone of a circular pier under clear water conditions. They used a hydrogen bubble technique to trace the flow patterns in the scour hole. They observed the formation of the horseshoe vortex system due to the downflow reflecting off the pier, as well as an increase in vortex size as the scour hole grows deeper. Estimates of mean bed shear stresses were made at 2 mm from the bottom using Newton's equation for viscosity. Melville and Raudkivi state that maximum shear stress occurs at the sides of the pier, which also coincides with the location where scour commences. Because of the difference in location of maximum shear and that of maximum scour depth, they concluded that scour must be caused by the downflow impacting on the bed, thereby dislodging the particles which eventually are carried downstream by the horseshoe vortex.

Rajaratnam (1980) studied the effects of vertical jets on an erodible non-cohesive bed. He found that the vertical jet creates a scour hole which is highly dependent on the velocity of the flow as it impinges on the bed.

Baker (1980) used dye visualization to show that the vortex circulation at the base of a pier remains constant even as the vortex grows in size while settling into the scour hole. Therefore, as the vortex grows, its tangential velocity decreases and thus the shear beneath the vortex also decreases.

Raudkivi (1986) used laboratory analysis to show that a downflow exists on the upstream face of a pier. The downflow is generated by a decreasing pressure gradient from the water surface to the channel bottom. He showed that the downflow has a velocity distribution with a maximum value occurring at 0.02 to 0.05 cylinder diameters upstream of the cylinder, being closer to the cylinder nearer to the channel bed. The maximum velocity of the downflow reaches about 80 percent of the mean approach flow velocity. The horseshoe vortex develops as a result of the downflow impacting on the channel bottom and Raudkivi believed it to be a consequence of scour, not the cause of it. Raudkivi stated that the downflow is the primary scouring agent and acts as a vertical jet which loosens and dislodges sediment particles.

Dargahi (1987, 1989) analyzed the mechanics of the flow field in the vicinity of a circular cylinder through hydrogen bubble visualization. He found that the vortices are generated within the main separated region of the flow as a result of several local separations. For most Reynolds numbers of practical value (8,400 – 46,000), the vortices show a quasi-periodical nature. The frequency of the vortex shedding does not change during the scouring process.

Dargahi (1987, 1989)

$$Re = \frac{vd}{\nu} \quad (1)$$

where: Re = Reynolds number
v = Velocity of flow (m/s)
d = Diameter of pier (m)
 ν = Kinematic viscosity of water (N^*s/m^2)

Roshko (1961) conducted experiments with flow at high Reynolds numbers in a wind tunnel. He found that as the Reynolds number increases, the Strouhal number also increases, indicating a boost in vortex shedding frequency.

$$St = \frac{\omega l}{v} \quad (2)$$

where: St = Strouhal number
 ω = Oscillation frequency (Hz)
l = Characteristic length (m)
v = Velocity of flow (m/s)

Maull and Young (1973) used a wind tunnel to study vortex shedding frequency around bluff bodies. They reported that the Strouhal number does not change along the length of the obstruction, implying that the shedding frequency varies continuously in a shear flow. They also reported that the shedding frequency at each location along the obstruction remains constant for a given flow. Breusers et al. (1977) reported that Vautier (1972) measured flow characteristics around vertical piers in two separate flumes of different widths, with the same approach flow conditions. They found that the pier nose vortex shedding frequencies were between 0.25 and 0.50 cycles per second, with no

significant difference in either the autocorrelation function or the spectral density function for flow velocity measurements.

Grecco (1990) observed that a horseshoe vortex system undergoes the following stages as the pier Reynolds number increases: steady single and multiple vortex regimes, simple oscillation, irregular unsteady motion, transition and turbulence. The critical Reynolds number from transition to turbulence is 4750. Eckerle and Awad (1991) defined a dimensionless parameter $(Re_D)^{1/3}(D/\delta)$, where Re_D = Reynolds number, D = depth of flow, and δ = boundary layer thickness, for a turbulent boundary layer flow. When this parameter is less than 1000, one horseshoe vortex system exists in the plane of symmetry; when this parameter is greater than 1000, no vortex is present.

Wen et al. (1993) made comparisons between the vortex systems that form on a rigid bed at the intersection of the bed and cylinder, and at the intersection of the cylinder and bed in a scour hole. They found that at the flat bed (before scour would commence), the vortex system consists of multiple strong primary (clockwise) vortices as well as weak secondary (counter-clockwise) vortices. The vortices oscillate upstream then back downstream before shedding around the pier. The frequency of shedding becomes unstable as the Reynolds number is increased. The vortex system within a scour hole generally consists of one vortex which is comparable to the size of the scour hole. The vortex rotates very slowly, and hence produces a weaker bed shear stress than in the flat bottom situation. The position of the vortex changes little, but oscillates slightly for higher Reynolds numbers.

Dey et al. (1995) developed a series of equations for velocity profile predictions in the x, y, and z directions in the upstream, downstream, and in the scour hole. The circulating and oscillating nature of the flow within the scour hole made measurements difficult, thereby questioning the applicability of the equations in this vicinity. Additionally, Dey et al. remarked that because of the downflow at the front face of the pier impacting the bed, the no-slip condition cannot be applied, resulting in the disappearance of a boundary layer.

Ahmed and Rajaratnam (1998) analyzed the effects of bottom bed material on the resulting flow field in the vicinity of cylindrical piers. Three bed conditions were analyzed: smooth, rough (rigid), and mobile. They found that for all bed conditions, the effect of the pier on the approaching velocity distribution can be felt for approximately 2.5 pier diameters in the upstream direction. The velocity decreases gradually as the cylinder is approached. Near the bed, the velocity diminished steadily to a point of negativity, which is due to the formation of the vortex system at the base of the pier. The pressure rises gradually as the pier is approached. However, the point at which the pressure begins to rise varies according to the approach flow velocity, suggesting that the presence of the pier is felt further upstream during flows with higher velocities. Also, larger piers produced higher pressure values at the face of the pier. Ahmed and Rajaratnam also found that the downflow produced by the presence of the pier exhibits a uniform velocity distribution. The maximum downflow velocity was measured to be as much as 95 percent of the maximum approach flow velocity once the scour hole was formed. This result was also discovered by Ettema

(1980). The maximum downflow velocity before the initiation of a scour hole reached about 35 percent of the approach flow velocity.

Ali and Karim (2002) reported on the principal features of the flow field which lead to pier scour. In summary, the flow decelerates as it approaches the cylinder, coming to rest at the face of the pier. The associated stagnation pressures are highest near the surface, where the deceleration is greatest, and decrease downwards. In response to the downwards pressure gradient at the pier face, the flow reaches a maximum just below the bed level. Ali and Karim claim that it is this downflow impinging on the bed which is the main scouring agent. The downflow acts like a vertical jet eroding a trench in front of the pier; the eroded material then is transported downstream by the development of the horseshoe vortex. The combination of the downflow and the horseshoe vortex provides the dominant scour mechanism. They also noted that the scour hole development commences at the sides of the pier with the two holes rapidly propagating upstream around the perimeter of the cylinder to meet on the centerline. Dargahi (1990) noted that the initiation of scour at the sides of the pier is due to the increased velocities of the flow at the sides of the pier, but that maximum scour is a result of the downflow and horseshoe vortex which form at the upstream face of the pier.

Graf and Istiarto (2002) experimentally investigated the flow field in a scour hole using an Acoustic Doppler Velocity Profiler (ADVP). At the upstream side of the cylinder, the following results were observed: (1) approaching the cylinder, the (longitudinal) u-component of velocity diminishes over the entire

depth, and begins to show negative values close to the bed; (2) in the approach region, the (vertical) w-component of velocity remains negligible, but grows considerably and reaches a value equal to roughly 60 percent of the approach flow mean velocity; and (3) the (lateral) v-component of velocity remains negligible but has some small values close to the bed, indicating three-dimensional flow. In regard to the vorticity of the flow field, they observed: (1) a positive vorticity is strong at the brink of the scour hole, leading to a weak counter-clockwise vortex; (2) directly upstream of the cylinder a strong clockwise vortex is developed; and (3) in the remaining part of the scour hole, the vorticity is weak and is of the same order as the approach flow vorticity. Shear stress measurements also were calculated based on the velocity profile and corresponding Reynolds stresses. The resulting values in the scour hole were less than the critical values of shear stress presented by Shields (1936), implying no sediment movement. Turbulence intensities were observed to be very strong at the foot of the cylinder on the upstream side.

2.4 Numerical Model Simulations

With advancements in computer technology, detailed mathematical simulation of the flow field in the vicinity of vertical obstructions has become feasible. Numerical approximations of the Navier-Stokes equations based on finite difference, finite element, or finite volume solutions have been incorporated into computer algorithms and used to analyze the mechanics of the scour problem. Estimations of bottom shear stress, turbulence intensities, and the

formation of the vortex systems have been a primary area of focus. The use of these programs has allowed researchers to analyze the effects of subtle adjustments to flow variables, which could not be accomplished easily during laboratory experiments.

Olsen and Melaaen (1993) used a three-dimensional numerical model to simulate the development of a scour hole. The simulation was based on the results of a physical model. The scour hole was only partially developed. The model was completed through 10 iterations of the changing bathymetry of the scour hole. Although they received encouraging results, Olsen and Melaaen warned that because the numeric model can not simulate the transient nature of the oscillating vortices in front of the pier, it may prove faulty for maximum scour depth predictions.

Mendoza-Cabral (1993) used the $k-\epsilon$ turbulence closure model to ascertain the bottom shear stress distribution on a rigid bed in front of a circular cylinder. His geometric data and flow variables were identical to those used by Melville and Raudkivi (1977) for a laboratory flume experiment. His results showed large discrepancies from values measured by Melville and Raudkivi. Mendoza-Cabral concluded that the $k-\epsilon$ turbulence closure model is inadequate for determining the flow field and associated shear stresses in front of cylindrical objects due to: (1) the inability of the model to handle anisotropic turbulence of three-dimensional curved flows, (2) the deficiency in representing the negative contributions to the generation of the kinetic energy of turbulence, (3) the inability to express the dependency of each component of the Reynolds-

stress tensor on one component of the mean strain rate tensor, and (4) the inability to account for Reynolds-stress relaxation.

In an attempt to produce better results than Mendoza-Cabral (1993), Richardson and Panchang (1998) used the Computational Fluid Dynamics model FLOW-3D to simulate the flow field around a circular pier, based on the experiments of Melville and Raudkivi (1977). The FLOW-3D model is based on the solution of the transient three-dimensional Navier Stokes equations by the volume-of-fluid method. In addition, the model can handle turbulence closure through a number of accepted schemes, including: Prandtl's mixing length theory, eddy viscosity model, two equation k- ϵ model, and the renormalized group (RNG) theory. The results of the simulation showed that with proper calibration of input variables, a flow field similar to the one reported by Melville and Raudkivi (1977) can be obtained. Shear stress distributions, however, were said to vary drastically but were not reported. No explanation was given for the discrepancy. Richardson and Panchang (1998) further showed that by tracking a single fluid particle at the bottom of a scour hole, predictions could be made as to a maximum depth of scour by noticing when the particle becomes trapped in the scour hole. They warned that this may not be a viable method for predicting a maximum scour depth, unless an accurate representation of geometric data can be simulated.

Karim and Ali (2000) investigated the suitability of using FLUENT CFD to model the flow field and corresponding bed shear stress values on a rigid open channel bed as well as in a non-pier induced scour hole. The geometric model

and flow conditions used were based on conditions presented by Ali and Lim (1986) and Wu and Rajaratnam (1995). The flow field and bottom shear stress results showed close correlation to the experimental results presented by the investigators previously mentioned. However, bottom shear stress measurements were for a location 8 mm above the channel bed. No predictions of shear on the actual channel surface were made.

Ali and Karim (2002) used the FLUENT CFD computer program to model the flow structure at a cylindrical pier. Bed shear stresses also were predicted using the model. Various simulations were performed, representing different time steps at the development of a scour hole. The geometric and flow conditions were based on experimental data provided by Yanmaz and Altinbilek (1991). Analysis of the results showed favorable comparison to the experimental results of the flow field. However, there was only a fair agreement between the bed shear stresses predicted by FLUENT and those calculated from the experimental velocities. This is most likely due to the fact that FLUENT gives on-bed predictions for shear stress, whereas the ones reported by Yanmaz and Altinbilek (1991) were at a distance of 8 mm above the bed. While the results obtained by Ali and Karim are acceptable, they state that using a numerical model such as FLUENT CFD can not produce truly accurate results due to its inability to model certain phenomenon such as turbulent bursts or the oscillating nature of the horseshoe vortex.

2.5 Local Scour Predictions

For streams characterized as being on gravel beds, scour depths from local scour can be much larger than from other scour, i.e., the long-term degradation and contraction scour. Therefore, for design purposes, maximum scour depth due to local scour predicted around structures, particularly piers, is the criteria used for determining the minimum depth at which supporting foundations are placed. Prediction formulas for local scour depth around piers are numerous. Some formulas are for clear-water scour, some for live-bed scour, and some are intended to serve for both. But, due to the complexity of the problem, most formulas were developed from the limited knowledge of factors and empirical relations based mostly on laboratory data. A great deal of discrepancy and even contradictions exist among these formulas. An accurate prediction using these formulas can be expected only for the cases that are similar to those utilized to develop the formulas.

The Schoharie Creek Bridge failure in 1987 prompted the development of a national set of guidelines which is to be used to predict scour depths in the vicinity of bridges. After the collapse of the bridge, which led to 10 fatalities, the Federal Highway Administration was commissioned by the federal government to review any prior studies, either experimental or through field observation, and based on the results of these studies recommend a series of universal equations which are to be used to compute the various forms of scour (pier, abutment, contraction). The result of the study was the creation of HEC-18. This manual provides national guidelines by which all existing and future federally supported

highway bridges are to be evaluated or designed based on scour susceptibility.

The initial pier scour equation utilized in HEC-18 is a variation of the one developed at the Colorado State University and is based on a set of dimensionless parameters.

Modified CSU Equation (Richardson et al. 1995) for both clear-water and live-bed scour:

$$\frac{y_s}{y_1} = 2.0K_1K_2K_3K_4 \left[\frac{a}{y_1} \right]^{0.65} Fr_1^{0.43} \quad (3)$$

Where: y_s = Scour depth (m)
 y_1 = Flow depth directly upstream of pier (m)
 K_1 = Correction factor for pier nose shape
 K_2 = Correction factor for angle of attack of flow
 K_3 = Correction factor for bed condition
 K_4 = Correction factor for armoring by bed material size
 a = Pier width (m)
 Fr_1 = Froude number upstream of pier = $V_1/(gy_1)^{1/2}$
 V_1 = Mean velocity of flow upstream of pier (m/s)
 g = Acceleration of gravity (m/s^2)

One parameter not included in Equation (3) is the bed shear stress generated at the upstream face of a blunt-nosed pier due to the horseshoe vortex. This omission is noticeable when considering several investigators have reported in the literature their belief that the horseshoe vortex creates an estimated increase of shear stress on the bed of 2 to 14 times that of the upstream approach flow, which in turn drives the scouring process. The exclusion of shear stress was necessary because in most cases reliable measurements at the beginning and final stages of the scouring process were

not possible due to the limitations of the measuring equipment and its inability to accurately measure the desired quantities. The goal of this research is to analyze the time variation of bed shear stress measurements at the base of a rectangular pier. Based on the results a conclusion will be drawn as to whether an increase in shear stress is indeed responsible for the initiation of scour around piers and subsequently if further research is warranted which will lead to the inclusion of a shear stress parameter in the equations used to predict pier scour.

CHAPTER 3

HYPOTHESIS

3.1 Statement of Problem

An increase in shear stress on the channel bottom beneath the horseshoe vortex has been cited by some researchers to be the primary mechanism for inducing local scour in non-cohesive soils (Shen 1966a, Breusars et al. 1977, Baker 1980, Froehlich 1988, Dey et al. 1995, etc.). Much research has been done in an attempt to quantify an exact value at which the shear is amplified when compared to the approach flow value, but the results of numerous studies are not consistent when compared to one another and range from amplifications in the approach flow shear stress values of 2 to 14 times.

The earliest studies of shear stress magnification were attributed to Chabert and Engeldinger (1956), who showed that before scour begins, the shear stress at the pier nose is approximately four times the value in the approach flow. This is based on the fact that regardless of pier size, scour at the pier nose begins when $U*/U_{*c} \geq 0.5$, where $U*$ = shear velocity and U_{*c} = critical shear velocity for particle movement. Schwind (1962) performed an extensive study of the horseshoe vortex and estimated that the shear stress under it is at least 12 times the undisturbed value.

Parola (1991) conducted a study of riprap sizes necessary to protect bridge piers against scour. He concluded that the effective velocity at the base of a pier must be approximately 1.5 to 1.7 times the approach velocity. Since shear stress is related to the velocity squared, it follows that Parola's effective shear

stress was 2.2 to 2.9 times the shear stress in the approach. Pagan (1991) conducted a study similar to Parola's, and found that the maximum effective shear stress at the base of abutments represented an amplification of approximately four times the average shear stress in the approach flow.

Johnson and Jones (1992) used marbles in a scour hole to indirectly measure the shear stress at the base of a pier at various scour depths. They concluded that the effective shear stress at the base of a pier varied from 2.8 to 14 times the shear stress in the approach flow, depending on the depth of scour.

Ahmed and Rajaratnam (1998) approximated shear stress measurements on the channel bottom at the pier using two three-tubed yaw probes. They measured an average increase of bed shear stress of 10-12 times, with a maximum of 13.5, the amount in the approach flow for rigid and mobile beds. However, for the smooth bed experiments, the amplification was much less (6 times) and also was confined to a smaller area around the pier. They also found that once the scour hole begins its formation, the distribution of shear stress decreased substantially at the sides of the pier, while increasing upstream of the pier.

Annandale (1999) proposed an erodibility index method for estimating scour limits in rock formations based on average stream power. He found that the approach stream power is amplified by 7.6 to 12.6 based on pier shape. Assuming that the shear stress is proportional to the stream power raised to the 2/3 power, it follows that the corresponding shear stress amplifications range from 3.9 to 5.4.

Jones (2002) performed experiments using sand particles and Shield's criteria for critical shear stress to estimate the amount of shear stress amplification at the base of a pier. He plotted a dimensionless shear stress parameter vs. a dimensionless depth parameter in order to develop a relationship of how shear stress varies according to scour depth. By extrapolating his data to a point of zero scour, he found that shear stress generally is amplified at the base of a pier by six times the amount in the approach flow. He then performed experiments on a rigid boundary using Particle Image Velocimetry (PIV) to ascertain the shear stress amounts. PIV has the ability to solve for shear stress directly using the definition of total shear stress based on Newton's law of viscosity and the Reynolds turbulent stresses. Using PIV, Jones found that the shear stress in front of a pier is amplified by 6.2. However, he cautioned that the results of the PIV analysis were very subjective as amplification values could have ranged from less than one up to 95.

Other researchers disagree in the assumption that an increase in shear stress induces pier scour and believe that the driving mechanism of scour is the downflow reflecting off the pier which subsequently impacts the channel bottom and erodes the soil; the horseshoe vortex system is only responsible for transporting the sediment once it is no longer attached to the bed (Melville 1975, Ettema 1980, Rajaratnam 1980, Raudkivi and Ettema 1983, etc.). The reason for such differences of opinion is that no actual physical measurements have ever been made of the shearing forces at the base of a blunt-nosed pier. In each

of the studies noted previously, assumptions were made about shear stress values through the measurement of more quantifiable variables.

This research, through the use of a force-displacement sensor which was calibrated to yield shear stress values, investigated the temporal variation of shear stress values generated at the base of rectangular piers. The results are used to ascertain a better understanding of the mechanisms which lead to local scour around vertical obstructions.

3.2 Hypothesis

Several investigators (Chabert and Engeldinger 1956, Shen 1966a, Melville 1975, Raudkivi and Ettema 1983, etc.) have shown pier scour will not commence until the approach shear velocity has reached half the critical shear velocity for incipient motion. Because shear is directly proportional to the shear velocity squared, it follows that the shear in front of a pier theoretically should be approximately four times the approach flow shear.

$$\tau_o = u_*^2 \rho \quad (4)$$

Where: τ_o = Average boundary shear stress (Pa)
 u_* = Shear velocity (m/s)
 ρ = Density of water = 1000 (kg/m³)

The underlying hypothesis for this research project is: scour is initiated by an increase of bed shear stress at the base of a pier of at least four times the approach flow shear stress.

$$\tau_{pier(\text{maximum})} \geq 4\tau_o \quad (5)$$

where: $\tau_{pier(\text{maximum})}$ = Maximum peak shear (Pa)
 $4\tau_o$ = Four times the average approach shear (Pa)

3.3 Hypothesis Verification

“Level Crossing Statistics” (explained in Chapter 8) are used to verify the proposed hypothesis. In particular, the magnitude and duration of the shear values above the approach flow shear stress are analyzed. Additionally, the periodicity and frequency of the measurements are found and used to determine if the vortex is “felt” on the channel bottom and responsible for the measured shear peaks.

CHAPTER 4

EXPERIMENTAL SETUP

4.1 Experimental Equipment

All experiments were conducted in a rectangular recirculating flume approximately 2.75 m long, .46 m wide and .30 m deep. A shear stress measuring device (Figure 4.1), designed by Mr. Hans Prechtl (2002), was used to measure all shear stress values. The device has the advantage of measuring actual forces which are captured through an electrical carrier signal. The electrical signal was calibrated to yield an applied shear stress. The specifications of the shear stress measuring device follow:

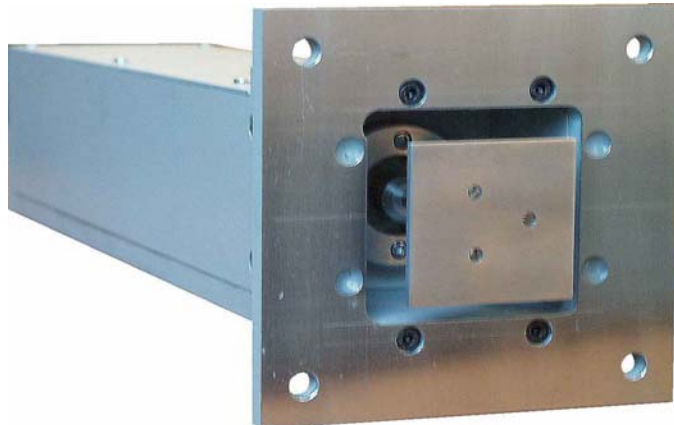


Figure 4.1 - Shear stress measuring device

Principles of Operation - The sensor consists of a stable aluminum case with a shaft (~ 300 mm) in it, which is ball-beared about 100 mm from the top. On the top of the shaft a carrier is mounted, on which the segments under test are attached. The force of the flowing water excites the segment under test to max +/- 1 mm displacement from its quiescent state.

About 100 mm under the pivot two bronze-springs are fixed. The deviation of the shaft is transferred to the springs by a highly flexible tension-band. So, each deviation of the shaft bends the resistance strain gauge, which gives in consequence an electrical signal to the connected carrier bridge. The force, which is necessary to bend the bronze-springs +/- 1 mm, is called Narrow Span. In the existing sensor the Narrow Span is about +/- 0.06 N.

To increase the measurement-range, a tension spring is mounted at the lower end of the shaft: pulling this spring will increase the force for the same amount of deviation (+/- 1 mm). A log-scale on the micrometer screw enables the user to set a predefined measurement-range for the sensor. In the existing design the final range was set to ~ 1N. Moreover the final range depends mainly on the spring-factor, whereby it may be adapted to the experimental arrangement by exchanging this spring.

The installation on the channel-floor is done very simply by some mounting-holes for the flange and one center-hole of 15 mm diameter, for the carrier. To compensate for various thicknesses of the channel wall, the carrier is moveable on the shaft to about +/- 10 mm.

At the carrier, the segments under test can be easily exchanged by loosening 3 small screws. The sensor has to be mounted vertically on the channel floor. To compensate for aberrations from this state, adjustment facilities are also provided on the sensor.

The constructive design makes the sensor in a wide range insensitive against temperature changes, assembling works at the segment and the carrier, water-level and water impurities. (Prechtl 2002)

The panel exposed to the fluid used to measure the applied force is rectangular in shape, approximately 5 cm per side. The device itself yields only an average shear stress over this area. Calibration of the device was achieved both statically and dynamically (see Chapter 5 for a detailed description of the

calibration process and identification of fluid forces). At its lowest setting, in a static case, the device can measure shear stresses ranging from 0 to 2 Pa (results from this study ranged from -0.3 to 0.5 Pa). Due to the sensitive nature of the measuring device (i.e. – fluctuations due to surrounding air disruptions) a new support structure was designed and built for the flume to make it sturdier and less prone to vibrations (Figure 4.2). The support structure consists of rigid I-beam steel construction with four legs .45 m high welded to floor plates; two .51 m beams at either end of the structure are used to connect the legs in the lateral direction, and two 2.64 m beams are used to connect the legs in the lengthwise direction.



Figure 4.2 - Flume support structure

A water tank approximately 1 m cubed was fabricated out of 1.9 cm thick clear plexi-glass and was used to store water supplied to the flume. A Chemflo Type 3 378 LPM pump with an impeller diameter of .133 m made of stainless steel construction was used to drive the water from the tank to the flume. The pump has a suction diameter of 5 cm and a discharge diameter of 3.8 cm. A Safrtronics Rapidpac GP-10, variable torque, variable speed control unit, pulse with modulating variable frequency drive was used to control the speed of the pump and hence the overall discharge. A dolly made of steel construction approximately 1 m wide by 1.5 m long was used as a platform to secure the tank and pump, making it external from the flume. This was necessary to reduce inherent vibrations caused by the pumping system (Figure 4.3).



Figure 4.3 - Tank/pump/motor controller/support dolly

A Kobold Turbine Flow Sensor with 0-10 VDC output signal and a range of 20-333 LPM (+/- 1%) was used to measure the flow entering the flume. The depth of water in the flume was controlled using a 10 cm CPEX true union ball valve placed externally at the exit of the flume. Water depth was measured to within an accuracy of 0.3 mm using a Baumer Electric Depth meter. The velocity distribution of the approach flow was measured using a Marsh-McBirney Electro-Magnetic Water Current Meter. A mobile carriage system built of ITEM CONSTRUCTION pieces was assembled and used to house the flow depth meter and velocity probe. The carriage system allowed for three degrees of freedom of the velocity probe (Figure 4.4).



Figure 4.4 - Carriage system used to house velocity probe

The piping system consisted of 5 cm PVC pipe going from the water tank to the pump, and 3.75 cm PVC pipe from the pump to the flow meter and then into the flume. A 10 cm PVC pipe carried the water from the exit of the flume, through the control valve and back into the water tank.



Figure 4.5 - Experimental setup showing tank/pump/motor controller/flume/carriage system

CHAPTER 5

IDENTIFICATION OF FLUID FORCES

5.1 Initial Offset Adjustment

The shear measuring device has an aluminum rod which extends out of the sensor casing and is topped with a flat plate which is exposed to water flowing over the sensor and through the flume (Figure 5.1). A very thin rubber membrane surrounds the aluminum rod and is used as a border separating the inner casing of the sensor and the outer environment (Figure 5.2). The membrane is flexible in allowing the rod to move when exposed to a tangential force applied over the flat plate, but secure enough to not allow any water to leak into the sensor casing which contains the strain gages and electrical components.



Figure 5.1 - Aluminum rod protruding from top (right) of sensor

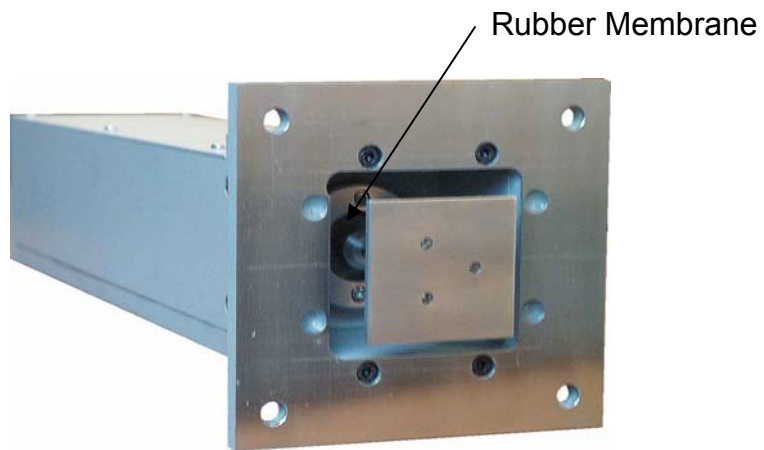


Figure 5.2 - Rubber membrane located at base of well in sensor

Because the membrane is flexible in allowing the rod to move, but also secure in that it stays fastened to the rod and surrounding casing, any force applied to the membrane also will cause displacements to the rod. When in a normal state, not exposed to any water, the sensor can be balanced to yield a zero voltage produced from the strain gages. However, when ponding water is applied to the sensor and its inner well, the membrane flexes due to the applied normal force of the water and hence causes deviations in the vertical rod alignment. Therefore, calibration was performed in order to develop a rating curve of an applied downward force due to the weight of the water vs. plate (or rod) displacement. This calibration was achieved by ponding water at various depths and recording subsequent voltage readings produced from the inner strain gages. The calibration was performed at the beginning, end, and various midpoint intervals during each day of experimentation. Each trial produced nearly identical calibration equations, which ultimately were used to filter out the effects of sensor displacement due to the weight of the water acting normally

over the sensor plate. A total of 15 trials were completed. Tables 5.1 lists the results of one such calibration. Figure 5.3 shows the corresponding trend line with best fit equation and R^2 value used for the adjustment.

Table 5.1 – Depth of flow vs. voltage - calibration data

depth (cm)	voltage
8.4	-1.25
8.03	-1.23
7.54	-1.17
7.15	-1.11
6.75	-1.06
6.38	-0.99
6	-0.93
5.63	-0.87
5.24	-0.81
4.82	-0.74
4.48	-0.69
4.04	-0.62
3.68	-0.56
3.31	-0.49
2.95	-0.44
2.6	-0.38
2.26	-0.32
2	-0.28
1.72	-0.24
0	0.05

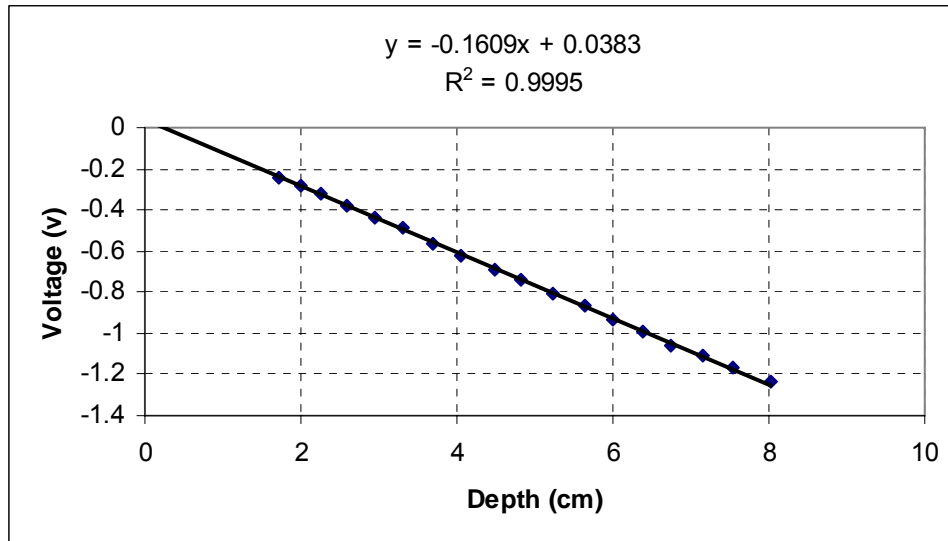


Figure 5.3 – Calibration curve with corresponding best fit equation used to adjust voltage signal offset caused by weight of water displacing sensor rod

5.2 Dynamic Calibration

The shear sensor used as part of this research can be considered a Flow Induced Structure with corresponding stiffness and damping (Figure 5.4). For a flow induced system operating at a low frequency ($\omega \ll \omega_n$) such that it may be considered quasi-static, the structural response of the system can be approximated to be proportional to the instantaneous exciting force exerted by the flow. However, if the force driving the system is operating at or near a frequency equal to that of the resonance of the system, the system may respond non-linearly (Figure 5.5). Because the voltage signal reported as output from the sensor, and used to determine an applied shear stress over the sensor, is directly related to the displacement of the sensor and not the driving force of the

flow, a dynamic calibration of the sensor is necessary in order to determine the actual shear generated by the flow.

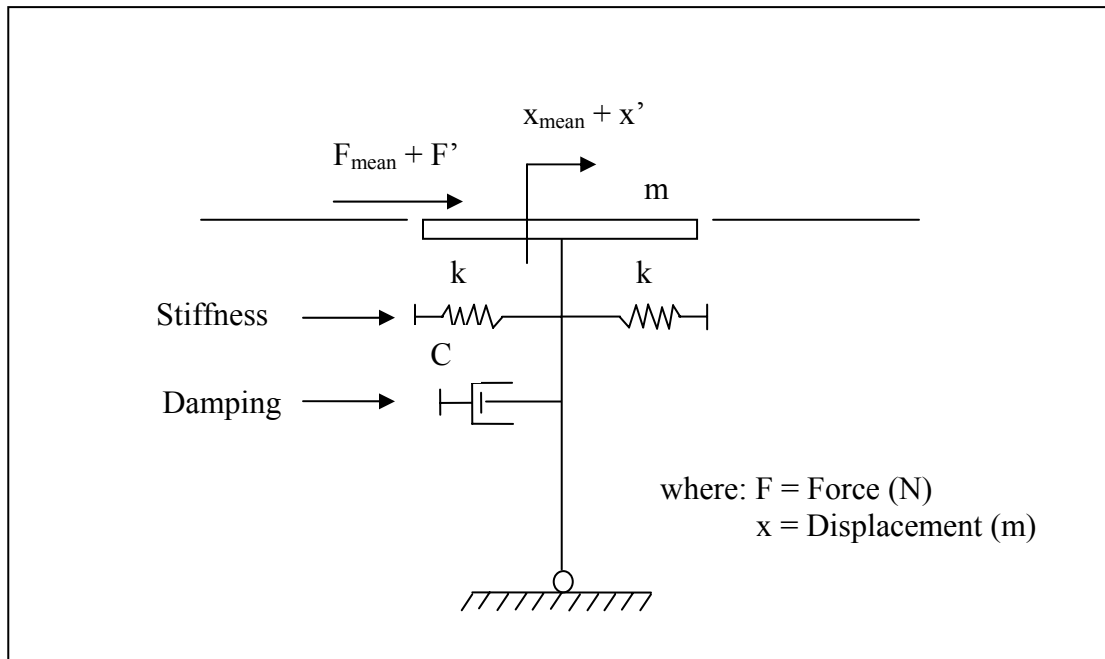


Figure 5.4 - Graphical representation of shear sensor plate with pivoting rod and associated stiffness and damping

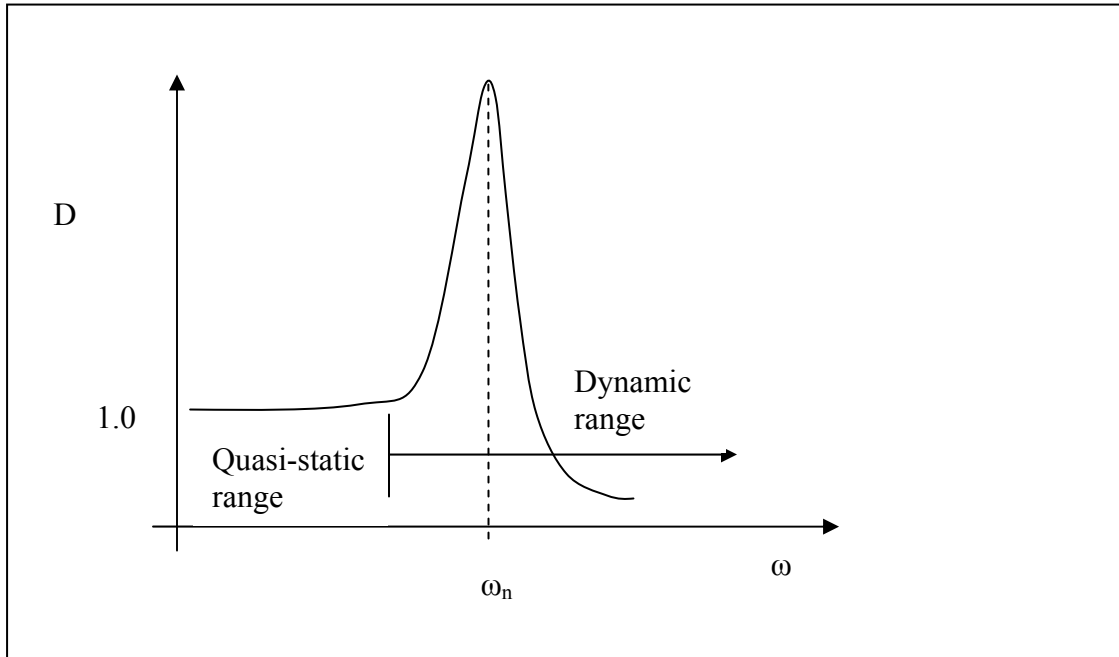


Figure 5.5 – Variation of dynamic magnification factor with frequency

A dynamic calibration can be completed once the stiffness, damping, and natural frequency of the sensor are known. The above properties are used to determine the unit impulse response function which then is used in combination with the response signal of the sensor to determine the input signal supplied by the flow as follows (Naudascher and Rockwell 1994):

$$S(\omega_i) = H(\omega_i) \cdot G(\omega_i) \quad (6)$$

where:

- $S(\omega_i)$ = Response signal of sensor in the frequency domain (Hz)
- $H(\omega_i)$ = Unit impulse response function of sensor in the frequency domain (Hz)
- $G(\omega_i)$ = Input signal supplied by flow in frequency domain (Hz)

Equation (6) can be rearranged to yield the input signal and hence driving force of the flow as follows:

$$G(\omega_i) = \frac{S(\omega_i)}{H(\omega_i)} \quad (7)$$

The unit impulse response function of the sensor in the time domain is determined from Equation (8):

$$h(t) = \frac{1}{m\omega} \sin(\omega t) \exp(-\xi\omega t) \quad (8)$$

where:
 $h(t)$ = Unit impulse response function (V)
 m = Mass of system (kg)
 ω = Natural frequency of sensor (Hz)
 t = Time (s)
 ξ = Damping (%)

The procedure used to determine the driving force of the flow is:

- a) The unit impulse response function of the sensor is calculated based on the dynamic properties of the sensor (Equation 8).
- b) The unit impulse response function is converted from the time domain to the frequency domain using a FFT.
- c) The response signal from the sensor is obtained through experimental measurements.
- d) The response signal of the sensor is converted to the frequency domain using a FFT.

- e) The response signal in the frequency domain is divided by the unit impulse response function in the frequency domain (Equation 7).
- f) An inverse FFT is performed on the resulting signal from step (e) to give the driving force of the flow in the time domain.

The flow chart in Figure 5.6 describes the overall process used to determine the driving force of the flow.

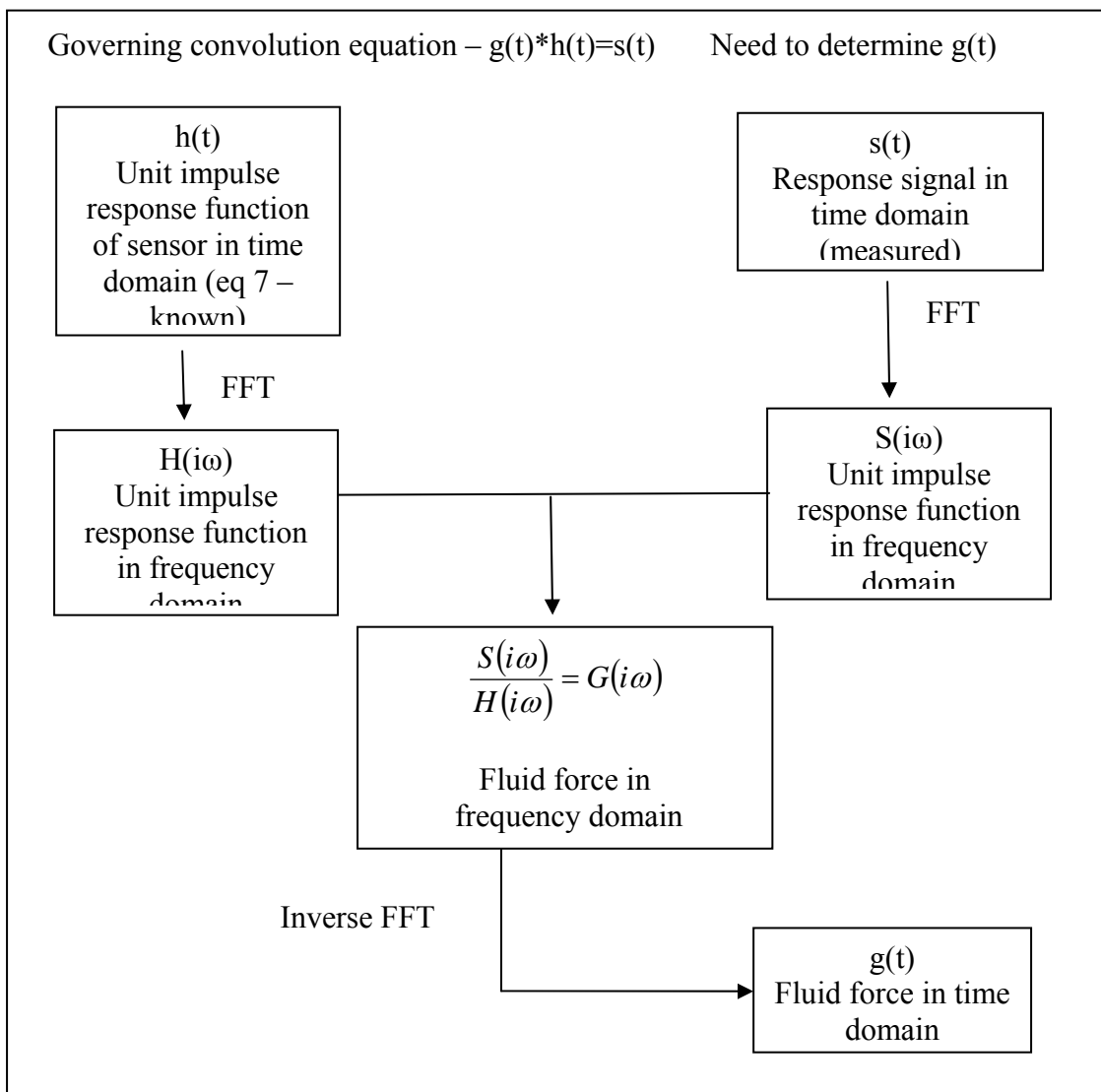


Figure 5.6 – Flow chart depicting procedure used for determining force delivered by flow to sensor

5.2.1 – Determination of Dynamic Properties

5.2.1.1 - Stiffness/Damping

The stiffness of the sensor can be obtained through a static calibration measurement of Force vs. Displacement. When exposed to tangential forces, the shear measuring device yields a voltage signal produced by a series of four strain gages and electrical resistors and wires used to transmit the signal. The voltage signal is captured by a Phillips Bridge Supply Frequency Converter (Figure 5.7).



Figure 5.7 - Phillips frequency converter used to capture voltage signal delivered by shear sensor

A calibration curve was created by exposing the sensor to a series of increasing vertical forces and recording the electrical response of the strain gages in terms of voltage. A moment analysis of the system (Figure 5.8) then was used to convert the vertical forces to an applied horizontal force. A

relationship then was developed between the applied horizontal force divided by the plate area, and the electrical response of the strain gages in terms of voltage.

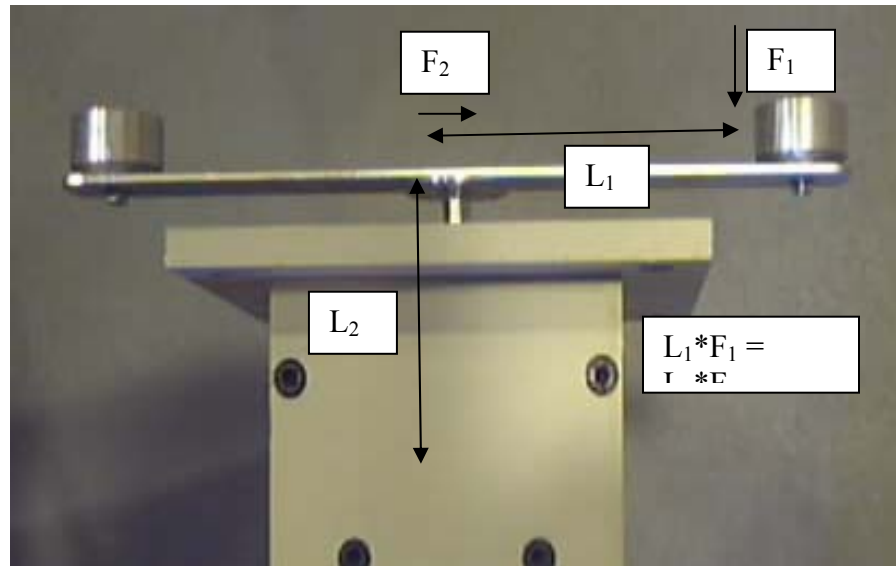


Figure 5.8 – Static calibration technique using known vertical forces and moment arm lengths to determine tangential forces

A total of six curves were produced, three representing an applied force in the positive direction and three in the negative direction. Each curve produced nearly identical results. Table 5.2 lists the results of one such calibration. Figure 5.9 shows the corresponding trend line with best fit linear equation and R^2 value. The best fit linear equation will be used later as part of the error analysis of the system (Section 6.3). The stiffness of the device is then equal to the slope of the calibration curve, after adjusting for Force vs. Displacement in lieu of Shear vs. Voltage. The stiffness in air was found to equal 4.5 N/m.

Table 5.2 –Shear vs. voltage - In-air stiffness determination data

Shear (Pa)	Voltage (V)
.03	.010
.07	.035
.12	.059
.24	.120
.36	.189
.48	.290
.60	.351
.72	.419
.85	.480
.97	.545
1.09	.607
1.21	.679
1.33	.742
1.45	.807
1.57	.877
1.70	.936
1.82	1.00
1.93	1.06

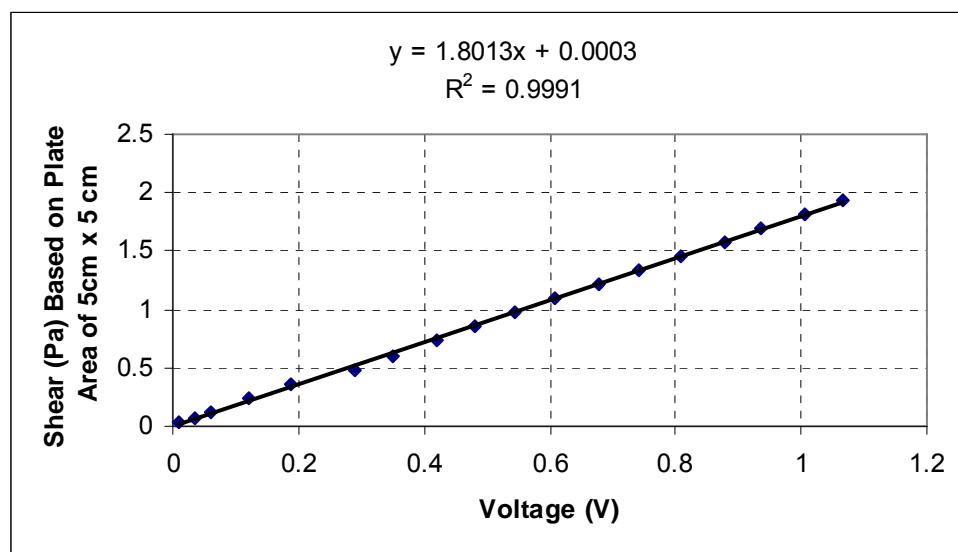


Figure 5.9 – Determination of stiffness of sensor by exposure to tangential shearing forces in air

It next was necessary to determine if the stiffness of the device changed under aquatic conditions. In order to determine the stiffness, weights of known densities and volumes were created and used to measure the forces in a similar manner as when in air. A total of three weights were manufactured, composed of steel with a specific weight of $76,700 \text{ N/m}^3$. The weights had a peg-like shape and their volumes varied from $9.8 \times 10^{-9} \text{ m}^3$ to $2.4 \times 10^{-7} \text{ m}^3$.

Two holes were drilled on the ends of the shear measuring plate and used to position the calibration weights (Figure 5.10). The location of the holes was recorded to within .5 mm of their length to the center of the shear plate. Both the measured distances of the drilled holes and the known volume and weight of the pegs were used in a moment analysis similar to that explained previously. A total of 12 measurements were taken, varying the depth of water for each set of trials in order to ascertain if the depth of water added any additional resistance while calibrating. Each trial produced nearly identical results, indicating that the depth of water did not affect the amount of resistance encountered. Table 5.3 lists the results of one such calibration. Figure 5.11 shows the corresponding trend line with best fit linear equation and R^2 value. Adjusting the curve for Force vs. Displacement shows the stiffness under water equal to approximately 5.5 N/m . This stiffness is slightly higher than the one found in air; however, the range of forces used to compute the stiffness was not complete and only accounted for small displacements of the sensor. Because the sensor is expected to operate under the full range of displacement, a stiffness of 4.5 N/m was used as part of

the sensor calibration process. The possible affect of using this stiffness in place of the measured stiffness under water is discussed in Section 6.3.

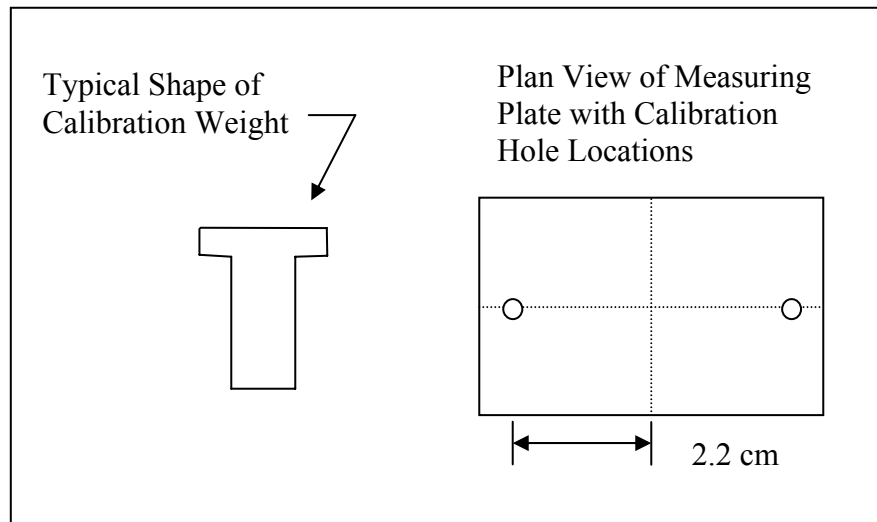


Figure 5.10 – Schematic of calibration weight/measuring plate used for stiffness determination under aquatic conditions

Table 5.3 –Shear vs. voltage - aquatic stiffness determination data

Shear (Pa)	Voltage (V)
0.00	0.00
0.258	0.12
.483	0.22

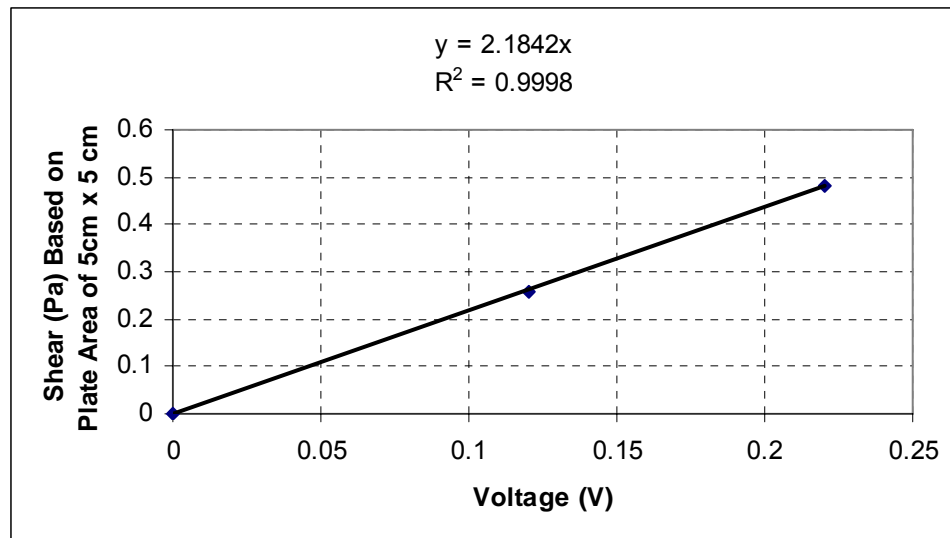


Figure 5.11 – Determination of stiffness of sensor when exposed to tangential shearing forces in water

The damping of the sensor is a measure of how the sensor will decay after a sudden excitation. This value was determined by the manufacturer and reported to equal 8 percent.

5.2.1.2 – Natural Frequency/Mass

If a flow induced structure is excited by a turbulent signal, it will respond around its natural frequency in spite of the fact that the natural frequency may not coincide with the dominant frequency of the excitation. This can be shown when plotting the amplitude spectrum of the response signal (Naudasher and Rockwell 1994) (Figure 5.12).

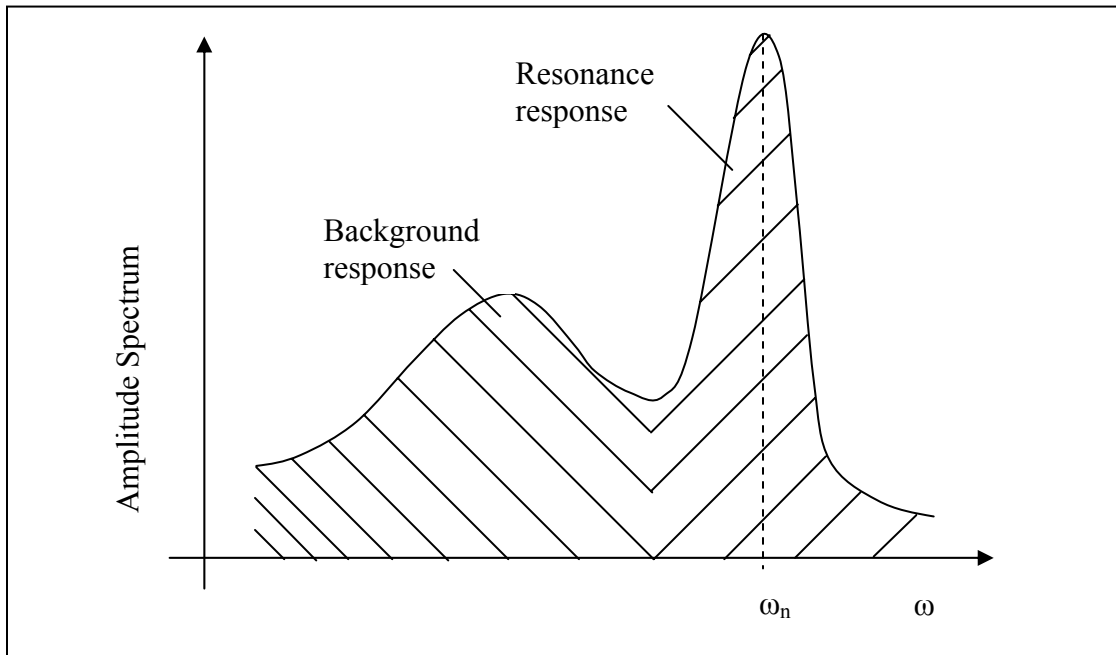


Figure 5.12 – Typical response of flow induced structure in frequency domain depicting peak amplitude at natural frequency of the structure

The shear sensor was allowed to respond freely under dynamic conditions induced by free surface flow moving across the sensor, at various depths. The response of the sensor was ascertained and then converted to the frequency domain using a Fast Fourier Transform of the data as shown in Figure 5.13. Based on the results of the various tests, the sensor is found to have a natural frequency equal to 9.0 Hz.

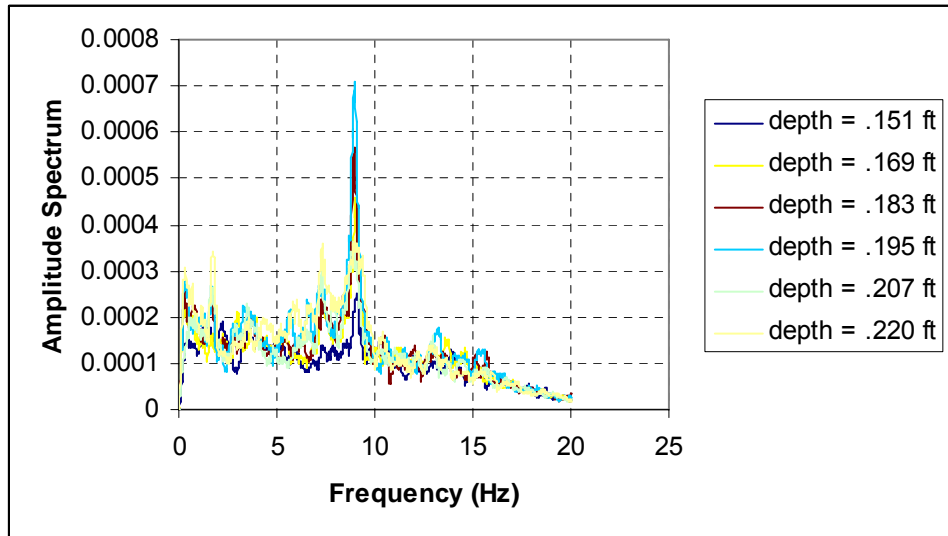


Figure 5.13 – Amplitude spectrum of response measurements of sensor at various flow depths, showing a natural frequency of 9.0 Hz

With a natural frequency of 9.0 Hz and a stiffness of 4.5 Hz, the mass of the system responding in the direction of flow can be determined by Equation (9):

$$\omega^2 = \frac{K}{m} \quad (9)$$

where: ω^2 = Natural frequency of sensor = 9.0 Hz
 K = Stiffness of sensor = 4.5 N/m
 m = Mass of sensor (kg)

Rearranging and solving Equation (9) shows a mass of .0014kg. With known mass, stiffness, damping, and natural frequency, Equation (7) is used in combination with the response signal of the sensor, according to the procedure outlined in Figure 5.6, to determine the fluid forces causing the sensor to displace.

CHAPTER 6

DATA COLLECTION

6.1 Autocorrelation Function/Correlation Length

A sufficient number of samples need to be collected in order to ensure statistical independence from adjacent measurements. The number of samples and frequency of measurements are determined by analyzing the autocorrelation function of a long time series of measurements at a very high sampling rate (Ermshaus 1985). Once the measurement is taken, the variance of the data is determined and used in conjunction with a predetermined statistical tolerance in order to determine the number of samples, also known as the correlation length. The precision chosen for the measurements was 0.005 Pa at 2 standard deviations, or a 96 percent confidence interval. The number of samples then is determined by use of the following equation:

$$N = \frac{\sigma_x^2}{\sigma_{x^2}^{-2}} \quad (10)$$

where: N = Number of samples for statistical independence from adjacent measurements

σ_x^2 = Variance of measurement

$\sigma_{x^2}^{-2}$ = Precision of measurement at 2 standard deviations

$$= \left(\frac{.005}{2} \right)^2 = .00000625$$

A long time series of shear measurements was taken at the base of a pier with a shallow depth and high Froude number in order to determine the maximum number of samples needed for the remaining experiments. The

combination of shallow and fast moving water produced the greatest variance of 0.06. Using this value of 0.06 in Equation (10) yields an upper limit of 10,400 samples to ensure statistical independence from adjacent measurements. A safety factor of over 10 percent was added, resulting in a total of 12,000 samples taken for each trial.

The frequency of the data measurements also is determined via the autocorrelation function (Ermshaus 1985). The autocorrelation function for the trial with the highest variance is shown in Figure 6.1.

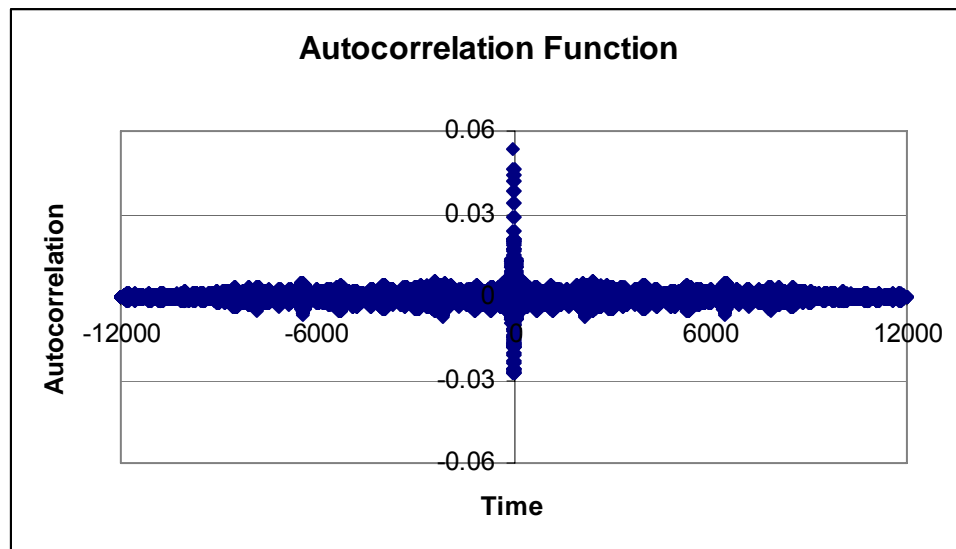


Figure 6.1 - Autocorrelation function of test run with highest variance used to determine minimum sampling frequency

In order to determine the minimum frequency for data collection, the correlation coefficient was found and then integrated. The correlation coefficient is equal to the autocorrelation function divided by the variance of the data string. The frequency then is determined by calculating the reciprocal of the area obtained through integration. A minimum frequency of 40 Hz was determined using this procedure. Since a large aspect of this research is analyzing the peak shear values of the measurements, the frequency of data collection was increased 200 Hz for all trials. This increase insured that all peaks were captured during data measurements.

6.2 Data Collection Procedure

Several trials were completed with Froude numbers varying between 0.1 - 0.56 for unobstructed flow and 0.13 – 0.45 for obstructed flow. The flow conditions were set by increasing or decreasing the speed on the variable frequency drive, used to control the speed of the pump. A minimum speed on the drive associated with 40 Hz was set as the lower limit. This speed led to flow depths of .065 ft and Froude numbers of 0.56. A minimum of three trials was run at this drive setting and the results were recorded. The drive then was increased in speed in increments of 5 Hz, and data collected. A total of 69 trials for unobstructed flow and 60 trials with a pier were completed.

6.3 Data Collection Errors

The possibility of obtaining an error in the data collected during any laboratory experiment is high. Two types of error typically are encountered: human error and equipment error. The possible human errors present in this work stem primarily from the initial calibration of the data collection equipment, i.e., depth sensor, flow sensor, shear sensor, etc. During the calibration of each of the measuring devices, human judgment was necessary. Specifically, human errors could have resulted during the following tasks:

- Calibration of the flow depth sensor – depths of flow needed to be measured using a length scale (ruler) and then cross-correlated with voltages read by the sensor. Calibration curves then were created relating the human-read depths and applied voltages. The human read measurements are estimated to be within 2 mm. Errors associated with the flow depth sensor have a direct influence on Froude number computations used for data analysis. The reported Froude numbers are calculated based on collected data and are accurate to within 0.02.
- Initiation of shear sensor – before any measurements were taken with the shear sensor, the sensor needed to be zeroed according to the analog voltage display frequency converter (Figure 5.9). The only way to zero this device is through a voltage adjustment knob on the face of the frequency converter. The knob was turned until the needle displaying the voltage was in a nearly completely vertical position, indicating a zero reading. A digital display device was used to verify the analog reading of

the frequency converter at several points during the calibration process.

The digital display showed actual voltages ranging from 0 to +/- 0.02 Volts.

When using an initial offset of +/- 0.02 Volts in the static calibration equation developed under aquatic conditions (Figure 5.13) an error in shear of 0.04 Pa is produced.

- Improper sensor stiffness coefficient – The effect of changing the stiffness coefficient from 4.5 N/m to 5.5 N/m was determined by changing the value input as part of the calibration procedure and re-calculating the results.

The outcome indicates a change in shear output ranging from .005 Pa at lower Froude numbers to .010 Pa at higher Froude numbers.

6.3.1 Equipment Error

All of the data collection equipment used for this study was based on the principle of an electrical voltage signal being given by the device which would then correspond to some physical quantity (depth, flow, shear, etc.). For some of the equipment (flow meter, depth meter, shear sensor), a minimum voltage needed to be obtained before the output of the device could be considered accurate. The flows and depths used throughout this study were above the minimum voltage requirement (as suggested by the manufacturer); therefore, the errors produced by these devices should lie within the error bounds supplied by the equipment manufacturer – 0.3 mm for the depth meter, one percent of total flow for the flow meter. For the shear sensor, however, no such minimum voltage requirement was supplied by the manufacturer; therefore, the amount of

error generated by the sensor had to be calculated based on calibration curves relating the voltage signal to an applied shear stress. As mentioned in Section 5.2.1.1, a total of six curves were created relating the voltage signal to an applied shear stress. Each curve was derived using the same calibration weights; therefore, in an ideal situation all six curves would be identical. The results of each calibration showed slight discrepancies in the final calibration equation. However, these discrepancies were small and in the range of only +/- 0.005 Pa for any particular voltage reading.

Combining human and equipment error, the sensor is considered to be accurate to within +/- 0.05 Pa.

CHAPTER 7

UNOBSTRUCTED FLOW

7.1 Results

A total of 69 experiments were completed using the shear measuring device. The purpose of the experiments was to ascertain a relationship between the uniform flow Froude number and an applied shear stress over the measuring plate. The relationship will be later used to ascertain an “approach flow shear stress” and how this value compares to a time series of shear measurements in front of a vertical obstruction. The results are listed in Table 7.1 and displayed graphically with corresponding error bars in Figure 7.1.

Table 7.1 – Unobstructed flow results

Trial Name	Q (lps)	Depth (cm)	Velocity (cm/s)	Froude #	Shear avg	Shear St. Dev.
40_1H	2.0	5.2	0.3	0.12	0.23	0.02
40_2H	2.0	5.2	0.3	0.12	0.22	0.02
40_3H	2.0	5.2	0.3	0.12	0.22	0.02
40_1L	2.2	2.0	0.8	0.56	0.57	0.07
40_2L	2.2	2.0	0.8	0.55	0.51	0.06
40_3L	2.2	2.0	0.8	0.56	0.53	0.06
45_1L	2.6	2.2	0.8	0.55	0.52	0.05
45_2L	2.6	2.2	0.8	0.55	0.53	0.04
45_3L	2.6	2.2	0.9	0.55	0.53	0.04
50_1H	2.8	5.6	0.4	0.14	0.24	0.02
50_2H	2.8	5.6	0.4	0.14	0.24	0.02
50_3H	2.8	5.6	0.4	0.14	0.24	0.02
50_2L	2.9	2.4	0.9	0.53	0.47	0.05
50_4L	2.9	2.5	0.9	0.52	0.38	0.11
50_5L	2.9	2.5	0.8	0.51	0.46	0.09
50_6L	2.9	2.5	0.9	0.53	0.38	0.11
55_1L	3.3	2.8	0.8	0.47	0.35	0.05
55_2L	3.3	2.8	0.8	0.48	0.32	0.05
55_3L	3.2	2.9	0.8	0.46	0.32	0.05
55_6L	3.2	2.8	0.8	0.48	0.38	0.08
60_1H	3.5	6.0	0.4	0.16	0.26	0.03
60_2H	3.5	5.9	0.4	0.16	0.26	0.02
60_4H	3.5	5.9	0.4	0.16	0.26	0.02

Trial Name	Q (lps)	Depth (cm)	Velocity (cm/s)	Froude #	Shear avg	Shear St. Dev.
60_5H	3.5	6.0	12.9	0.17	0.26	0.03
60_1L	3.6	3.1	25.0	0.45	0.33	0.04
60_2L	3.6	3.1	24.8	0.45	0.33	0.05
60_3L	3.6	3.2	24.3	0.43	0.33	0.04
60_4L	3.5	3.2	24.2	0.43	0.32	0.04
65_1L	3.9	3.4	25.1	0.44	0.39	0.08
65_2L	3.9	3.4	24.7	0.43	0.37	0.08
65_3L	3.9	3.4	24.7	0.43	0.37	0.08
67_1L	4.0	4.0	21.9	0.35	0.35	0.02
67_2L	4.0	3.8	23.0	0.38	0.36	0.02
67_3L	4.0	3.8	22.9	0.37	0.36	0.02
70_1H	4.1	6.3	14.2	0.18	0.28	0.02
70_2H	4.1	6.3	14.3	0.18	0.28	0.02
70_3H	4.1	6.3	14.1	0.18	0.28	0.02
70_4H	4.1	6.3	14.1	0.18	0.28	0.04
70_1L	4.2	3.2	28.6	0.51	0.36	0.08
70_2L	4.2	3.2	28.7	0.51	0.38	0.10
70_3L	4.1	3.4	26.6	0.46	0.39	0.08
75_4L	4.4	3.4	28.7	0.50	0.36	0.07
75_5L	4.4	3.4	28.7	0.50	0.37	0.07
75_6L	4.4	3.4	28.9	0.50	0.34	0.07
75_7L	4.4	3.4	29.0	0.51	0.35	0.07
80_1H	4.7	6.6	15.7	0.19	0.28	0.02
80_2H	4.7	6.6	15.7	0.19	0.28	0.03
80_8H	4.7	6.6	15.6	0.19	0.28	0.02
80_9H	4.7	6.6	15.5	0.19	0.29	0.03
80_10H	4.7	6.8	15.2	0.19	0.27	0.03
80_11H	4.7	6.6	15.5	0.19	0.27	0.02
80_1L	4.7	3.9	26.7	0.43	0.35	0.04
80_2L	4.7	3.9	26.7	0.43	0.36	0.04
80_3L	4.7	3.9	26.7	0.43	0.35	0.04
85_1L	5.0	5.0	21.8	0.31	0.32	0.03
85_2L	5.0	5.8	19.0	0.25	0.31	0.03
85_3L	5.0	5.0	22.1	0.32	0.32	0.04
90_1H	5.3	7.3	15.9	0.19	0.29	0.03
90_2H	5.3	7.3	15.8	0.19	0.29	0.02
90_3H	5.3	7.3	15.8	0.19	0.29	0.03
90_1L	5.3	5.9	19.7	0.26	0.32	0.04
90_2L	5.3	5.9	19.6	0.26	0.30	0.04
90_3L	5.3	6.0	19.2	0.25	0.31	0.04
94_1H	5.5	7.5	16.0	0.19	0.30	0.03
94_2H	5.5	7.6	15.9	0.18	0.29	0.03
94_3H	5.5	7.5	16.0	0.19	0.29	0.03
94_1L	5.5	6.8	17.8	0.22	0.31	0.04
94_2L	5.5	6.5	18.6	0.23	0.31	0.04
94_3L	5.5	6.3	19.1	0.24	0.33	0.04

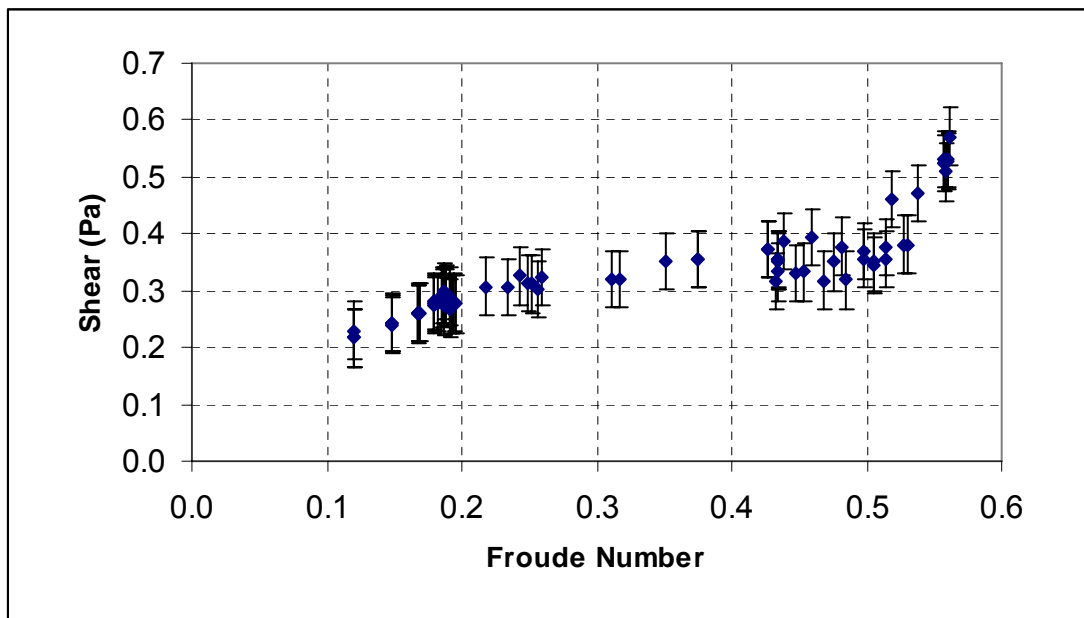


Figure 7.1 – Graphical display of results of shear vs. Froude number with corresponding error bars (+/- .05 Pa) obtained from the unobstructed flow analysis

7.2 Analysis

For Froude numbers ranging from 0.1 - 0.4, there is an increase of shear with Froude number. This increase is expected when considering that the bed shear on a channel bottom is directly proportional to the shear velocity squared (Equation 4), and the shear velocity is proportional to the coordinate velocity of the flow (Equation 11) (assuming a logarithmic velocity distribution of the flow). Additionally, the Froude number is also directly proportional to the mean velocity of the flow (Equation 12); therefore, an increase in mean velocity which leads to an increase in Froude number should translate into an increase in bed shear.

$$\frac{u}{u_*} = \frac{1}{k} \ln\left(\frac{u_* y}{\nu}\right) + B \quad (11)$$

where:
 u = Coordinate velocity (m/s)
 u_* = Shear velocity (m/s)
 k = Prandtl's constant = 0.4
 y = Depth (m)
 ν = Kinematic viscosity (m^2/s)
 B = Constant of integration

$$Fr_{rect_channel} = \frac{\bar{u}}{\sqrt{gy}} \quad (12)$$

where:
 Fr = Froude number in a rectangular channel
 \bar{u} = Mean velocity of flow (m/s)
 g = Constant of gravity = $9.8 m/s^2$
 y = Depth of flow (m)

For Froude numbers ranging from 0.40-0.52 the increasing trend ceases, a lot of scatter is present, and shear appears to be independent of Froude number. The hydraulic conditions of the flow were checked at these Froude numbers and it was noticed that the depths of flow ranged from approximately 1.0 to 1.5 inches. Additionally, it was observed during the experiments that for the trials executed at shallow water depths (< 1.5 inches), noticeable surface waves were present; whereas for higher water depths, a nearly uniform flow was achieved (according to visual observation). The existence of these surface waves produces a non-uniform flow resulting in greater fluctuations in the shear values reported by the sensor. These fluctuations should be identifiable in the standard deviation of shear measurements from each trial (Figure 7.2).

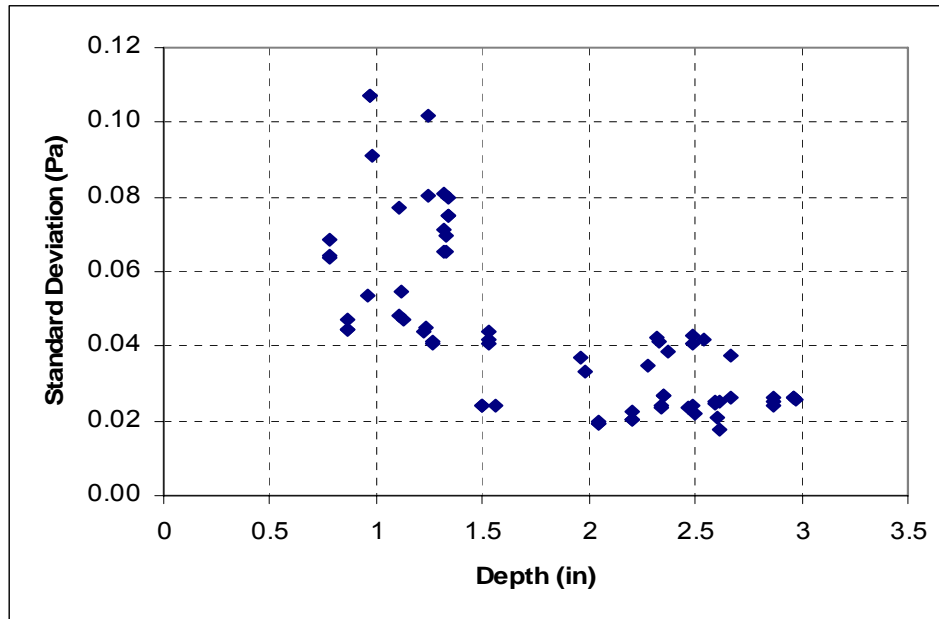


Figure 7.2 – Standard deviation of shear values vs. depth of flow for unobstructed flow trials

The standard deviation of each trial with depths of flow greater than 1.5 inches consistently falls in the range of 0.02 – 0.04 Pa. However once the depth of flow drops below 1.5 inches a sudden, non-uniform increase of standard deviation is observed. This increase supports the visual observation of surface waves present in the flow, and further strengthens the previous argument that the fluctuations in average shear values for Froude numbers ranging from 0.4 – 0.52 are due to non-uniform flow and surface waves.

For Froude numbers greater than 0.52, an almost asymptotic increasing parabolic trend is observed. This trend was not expected and required investigation. For each of the trials performed with Froude numbers greater than 0.52, the depth of flow was less than 1 inch (Figure 7.3).

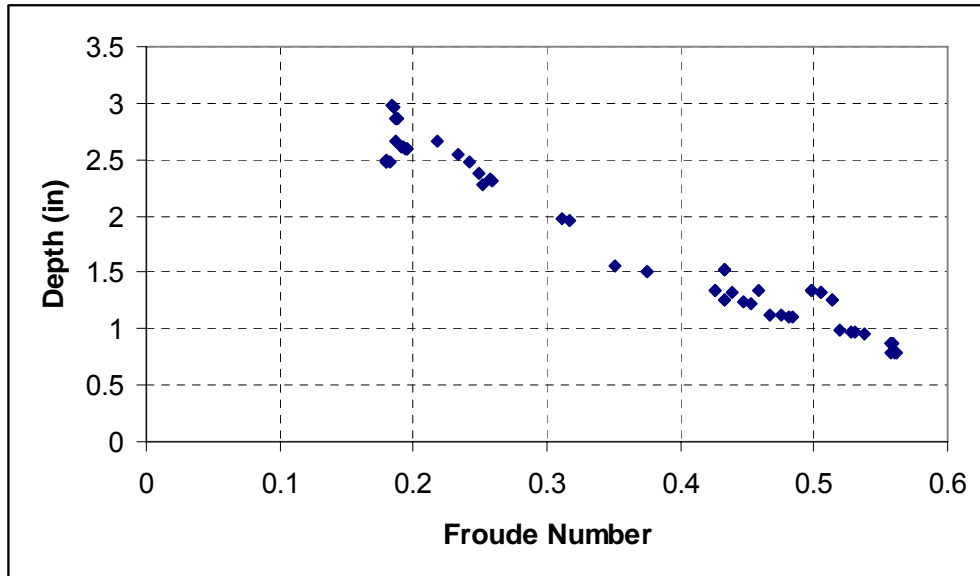


Figure 7.3 – Variation of depth with Froude number showing depths of flow less than 1 Inch for Froude numbers > 0.52

Because of the shallow water depth, additional forces on the channel bottom may be introduced due to surface tension which would not be present at the larger depths. These forces can be analyzed through the Weber number, which is a ratio of forces attributed to fluid inertia and surface tension. Once the Weber number falls below 100, surface tension effects start to become important (Ettema 2000). The Weber numbers were calculated for the trials with Froude numbers greater than 0.52 and ranged in value from 16 to 21.

$$We = \frac{\rho U_o^2 L}{\sigma} \quad (13)$$

where:

We =	Weber number
ρ =	Density of water = 1000 (kg/m ³)
U_o =	Mean velocity (m/s)
L =	Characteristic length (depth) (m)
σ =	Surface tension strength of water (N/m)

Additionally, Ettema (2000, p 63) states, “Whereas surface tension exerts negligible influence in most free-surface flows of civil engineering importance, it cannot be neglected for very shallow flows, such as those in physical models. Based on a comparison of propagation speeds of gravity waves and capillary waves, it can be shown that water depths in models of such channels should not be less than approximately 1 inch.” Based on the work of Ettema (2000) and the calculation of Weber numbers less than 100, a conclusion is made that the increasing parabolic trend reported by the sensor at Froude numbers greater than 0.52 is due to an introduction of surface tension forces between the fluid and sensor plate.

7.2.1 Comparison to Theoretical Predictions

The results obtained through the shear measuring device for Froude numbers ranging from 0.1 – 0.4 were compared to two theoretical methods for predicting bed shear stress. Froude numbers greater than 0.4 were not compared to the theoretical equations due to the shallow depths of flow and presence of surface waves, which possibly could create erroneous measurements which would not be accurately accounted for by the theoretical equations. The first theoretical consideration is the shear equation derived from a control volume approach given in Equation (14).

$$\tau = \gamma R S \quad (14)$$

Where:

τ	= Average shear stress (Pa)
γ	= Specific weight (N/m^3)
R	= Hydraulic radius (m)
S	= Average friction slope (m/m)

In order to solve this equation, the friction slope must be known. This parameter was calculated through Manning's Equation (15), using an accepted "n" value for plexiglass of 0.01.

$$V = \frac{1.0}{n} R^{\frac{2}{3}} S_f^{\frac{1}{2}} \quad (15)$$

where:
 V = Average velocity (m/s)
 n = Roughness coefficient
 R = Hydraulic radius (m)
 S_f = Friction slope (m/m)

The average velocity was calculated based on the continuity equation with known flow and depth. The hydraulic radius is a ratio of the flow area to the wetted perimeter of the channel and was calculated based on a channel width of .46 m. Equation (15) then was rearranged and solved for the friction slope, which was then used in Equation (14) to solve for a predicted shear stress on the channel bottom.

The second theoretical consideration was based on Equations (4) and (11), presented earlier (Section 7.2). Equation (11) can be used to solve for the shear velocity on the channel bottom if the coordinate velocity is known at a specific depth. Because velocity distributions were not measured over the sensor for each trial, only the mean velocity can be calculated from the continuity equation. This velocity was assumed to occur at approximately four tenths (0.4) of the depth from the channel bottom (Chaudhry 1993). This assumption is widely considered to be valid by the engineering community. Using the average

velocity and assuming it occurs at four tenths of the depth, Equation (11) was solved to yield the shear velocity. This shear velocity then was used in Equation (4) to solve for the boundary shear stress. Table 7.2 lists the hydraulic properties used to solve Equations (4), (11), (14) and (15), as well as resulting shear stress values.

The shears predicted from Equations (4) and (14) show very good agreement, but under-predict the shear values measured from the sensor by an average value of 0.20 Pa (Figure 7.4). This value (0.20 Pa) falls outside the error bars of 0.05 Pa for the sensor. It is interesting to note that the trends predicted from both Equations (4) and (14) agree favorably to that measured from the shear sensor, as can be seen in Figure 7.5, which displays a hypothetical increase of shear of 0.2 Pa to both theoretical equations.

The fact that both theoretical equations agree well with each other tends to indicate that the shear measured from the sensor, if accurate, should correspond closely to the predicted values. Unfortunately, this is not the case, as is seen in Figure 7.4. However, the general trend of the shear measured from the sensor corresponds to the predicted trend from the theoretical equations, and implies that the sensor has an initial offset which leads to a constant error. Because the flow field in front of a pier is different from that of an unobstructed flow, it may not be appropriate to adjust the shear values by the offset noticed from the unobstructed flow results. However, since the offset does seem to be consistent an argument can be made that the sensor calibration is off and therefore all of the results (unobstructed and unobstructed) should be adjusted.

Therefore, two analyses were completed for the peak shear ratios, one without the 0.2 Pa adjustment and one with the adjustment.

Table 7.2 – Hydraulic parameters used for shear stress predictions

Name	Flow (lps)	Depth (cm)	Velocity (cm/s)	Fr #	S _f	Shear (Pa) Eq (14)	Critical Velocity (cm/s)	Shear (Pa) Eq (10)
40_2H	2.0	5.2	8.6	0.12	5E-05	0.02	0.5	0.03
40_3H	2.0	5.2	8.6	0.12	5E-05	0.02	0.5	0.03
40_1H	2.0	5.2	8.6	0.12	5E-05	0.02	0.5	0.03
50_1H	2.8	5.6	11.0	0.15	7E-05	0.03	0.6	0.04
50_2H	2.8	5.6	11.0	0.15	8E-05	0.03	0.7	0.04
50_3H	2.8	5.6	11.0	0.15	8E-05	0.03	0.6	0.04
60_4H	3.5	5.9	12.8	0.17	9E-05	0.04	0.7	0.05
60_1H	3.5	6.0	12.8	0.17	1E-04	0.04	0.7	0.05
60_5H	3.5	6.0	12.9	0.17	1E-04	0.04	0.7	0.05
60_2H	3.5	5.9	12.9	0.17	1E-04	0.05	0.7	0.06
70_3H	4.1	6.3	14.1	0.18	1E-04	0.05	0.8	0.06
70_4H	4.1	6.3	14.1	0.18	1E-04	0.05	0.8	0.06
70_1H	4.1	6.3	14.2	0.18	1E-04	0.05	0.8	0.06
70_2H	4.1	6.3	14.3	0.18	1E-04	0.05	0.8	0.07
94_2H	5.5	7.6	15.9	0.18	1E-04	0.06	0.9	0.08
94_3H	5.5	7.5	16.0	0.19	1E-04	0.06	0.9	0.08
94_1H	5.5	7.5	16.0	0.19	1E-04	0.06	0.9	0.08
80_10H	4.7	6.8	15.2	0.19	1E-04	0.06	0.8	0.07
90_3H	5.3	7.3	15.8	0.19	1E-04	0.06	0.9	0.08
90_2H	5.3	7.3	15.8	0.19	1E-04	0.06	0.9	0.08
90_1H	5.3	7.3	15.9	0.19	1E-04	0.06	0.9	0.08
80_11H	4.7	6.6	15.5	0.19	1E-04	0.06	0.9	0.07
80_9H	4.7	6.6	15.5	0.19	1E-04	0.06	0.9	0.07
80_8H	4.7	6.6	15.6	0.19	1E-04	0.06	0.9	0.07
80_2H	4.7	6.6	15.7	0.19	1E-04	0.06	0.9	0.08
80_1H	4.7	6.6	15.7	0.19	1E-04	0.06	0.9	0.08
94_1L	5.5	6.8	17.8	0.22	2E-04	0.08	1.0	0.09
94_2L	5.5	6.5	18.6	0.23	2E-04	0.09	1.0	0.10
94_3L	5.5	6.3	19.1	0.24	2E-04	0.10	1.0	0.11
90_3L	5.3	6.0	19.2	0.25	2E-04	0.10	1.1	0.11
85_2L	5.0	5.8	19.0	0.25	2E-04	0.10	1.0	0.11
90_2L	5.3	5.9	19.6	0.26	2E-04	0.10	1.1	0.12
90_1L	5.3	5.9	19.7	0.26	2E-04	0.10	1.1	0.12
85_1L	5.0	5.0	21.8	0.31	3E-04	0.13	1.2	0.15
85_3L	5.0	5.0	22.1	0.32	3E-04	0.14	1.2	0.15
67_1L	4.0	4.0	21.9	0.35	4E-04	0.15	1.3	0.16
67_3L	4.0	3.8	22.9	0.37	5E-04	0.16	1.3	0.17
67_2L	4.0	3.8	23.0	0.38	5E-04	0.16	1.3	0.17

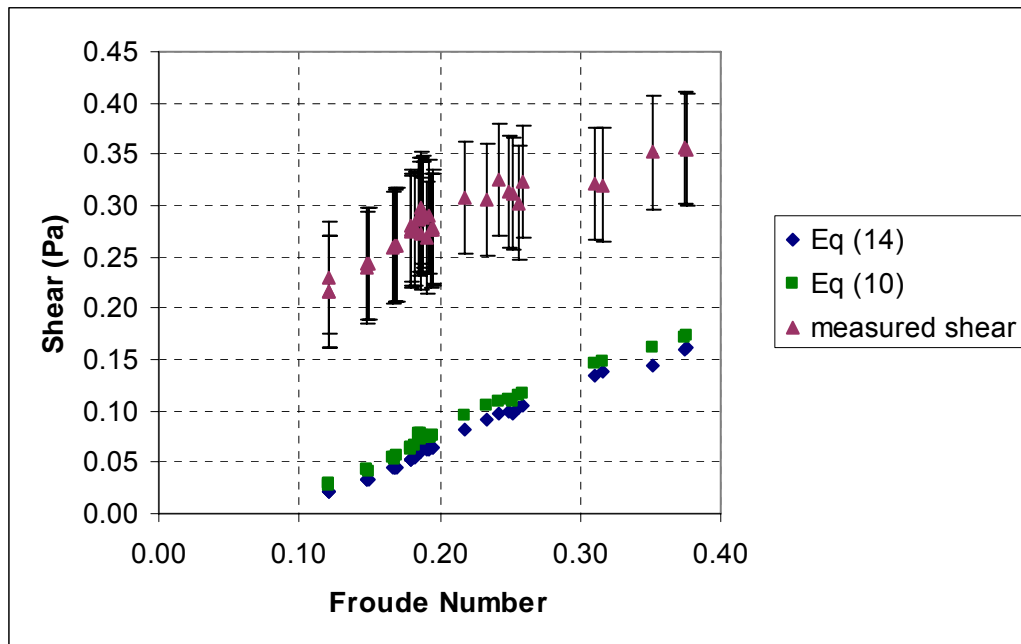


Figure 7.4 – Predicted shear from Equations (10) and (14) plus measured shear from sensor vs. Froude number

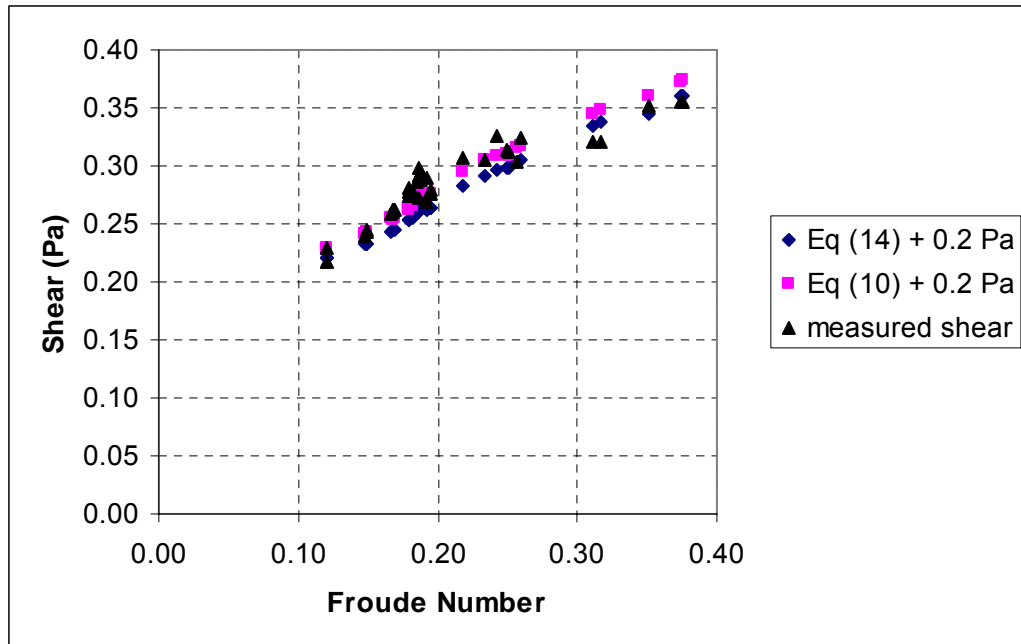


Figure 7.5 – Comparison of predicted shear values from Equations (10) and (14) to shear measured from sensor, with a hypothetical increase in shear of 0.20 Pa added to each theoretical equation

CHAPTER 8

OBSTRUCTED FLOW

8.1 Pier Size

A pier width of sufficient size was necessary in order to produce as large a vortex as possible and therefore maximize the effectiveness of the shear sensor. The shear sensor will perform optimally if the vortex formed at the base of the pier completely encapsulates the entire area of the sensor. This would ensure that the entire shear being measured by the sensor is created solely by the vortex and not by the increasing velocities of the flow as it moves around the sides of the obstruction. Ettema (1980) showed the minimum allowable flume width to pier width ratio in order to eliminate sidewall contraction effects is 6.25:1 (Figure 8.1). Based on the ratio noted above and the flume width of 46 cm, a pier width of 7.5 cm was used for all trials involving a pier.

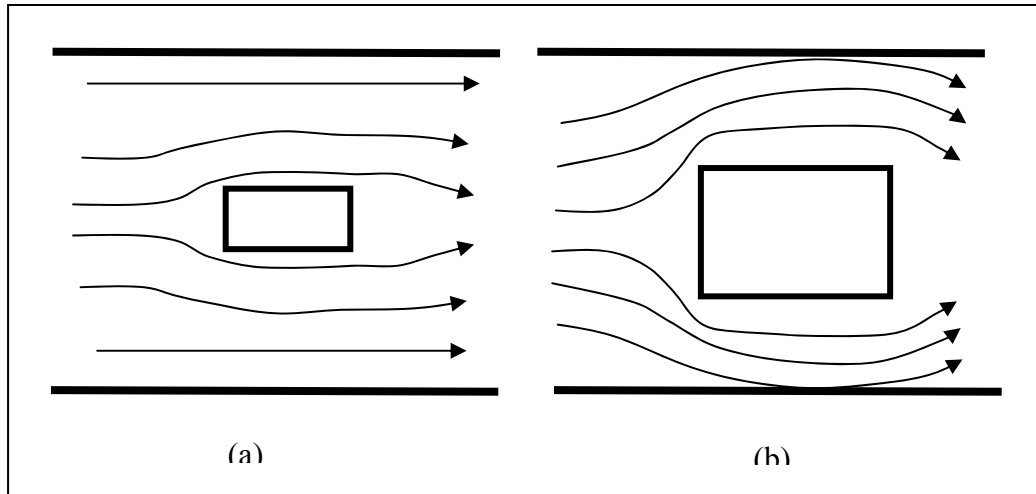


Figure 8.1 – Graphical depiction of flow fields with (a) no side-wall contraction effects and (b) side-wall contraction effects

8.2 Shear Threshold

The basis of this work is to determine the differences in shear measurements on the channel bed in a uniform flow with no obstruction, and in front of a pier. The results are used to quantify the effect of shear stress in initiating scour. In order to accomplish this, a shear threshold or what would be considered an approach flow shear stress was determined (Chapter 7). A best fit trend line and corresponding equation was developed for Froude numbers ranging from 0.10 to 0.40 Pa, relating shear stress to Froude number (Figure 8.2). Results for Froude numbers greater than 0.4 were not used in developing the threshold equation due to the reasons mentioned previously (Section 7.2). The trend line with equation was necessary so that a shear threshold could be ascertained for the obstructed flow experiments based on the results of the non-obstructed flow at any Froude number.

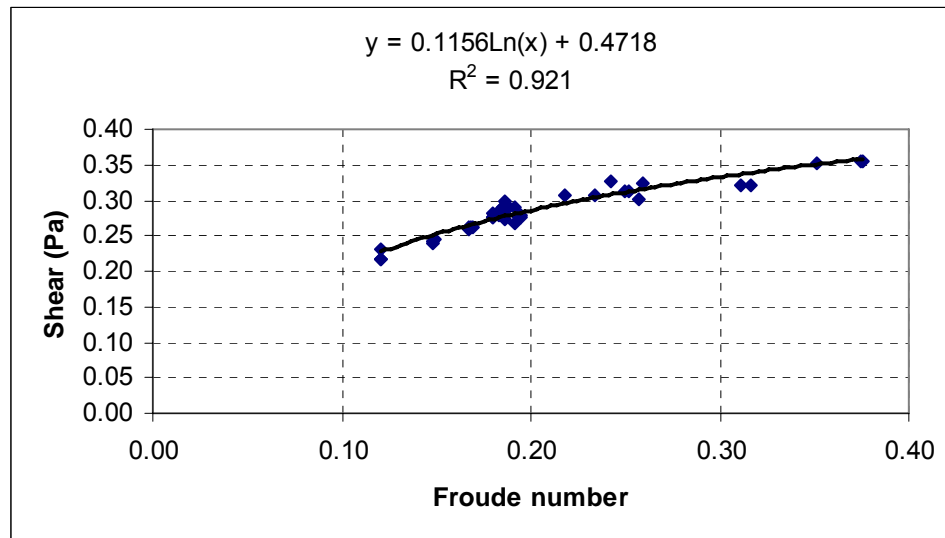


Figure 8.2 – Graph and corresponding best fit trend line with equation and R^2 showing data used from Chapter 7 in order to determine a shear threshold used for statistical analysis

8.3 Shear Measurements

A total of 60 experiments were completed for this part of the analysis. Each trial consisted of recording a total of 12,000 data points in front of a pier for duration of one minute. A typical plot of the results is shown in Figure 8.3, which shows the shear to fluctuate much like that of a turbulent velocity signal. The straight line on the plot indicates the shear threshold ascertained from the equation presented in Figure 8.2. Analysis of the measurements will focus primarily on those times when the shear exceeds the threshold. This will be accomplished with the use of “level crossing statistics,” described in Section 8.4.

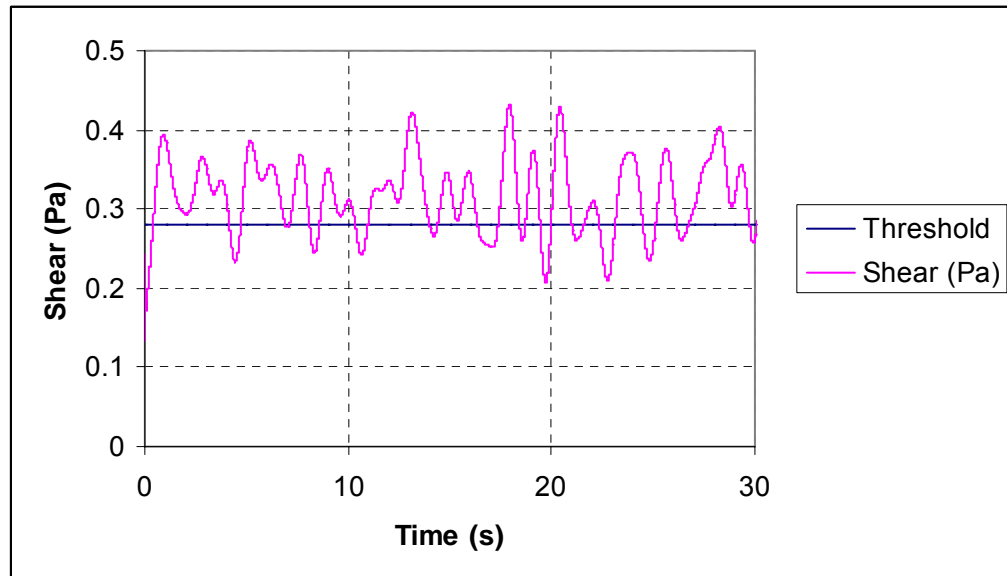


Figure 8.3 – Typical time variation of shear stress in front of pier

8.4 Level Crossing Statistics

Level crossing statistics have been used extensively in the field of earthquake engineering. The premise of this type of statistical analysis in earthquake engineering is to ascertain predictions for the potential failure of a building or other design component, based on its response to vibrations, induced by earthquakes, exceeding a threshold for stability as stipulated by the designer. The major focus of the analysis is on determining: (a) whether the response of the building has a periodic signature, (b) how often the vibration causes the building to exceed a tolerance threshold for vibrations in any given second, (c) the typical duration which the threshold is exceeded, and (d) the probability that the threshold will be exceeded.

When viewing the time series of shear stress fluctuations over the shear sensor, it is apparent that there is at least a quasi-periodic distribution similar to that of earthquake vibrations (Figure 8.3). By extension, a grain of sediment can be analogous to a building and the variation of shear stresses over time can be analogous to the vibrations induced by earthquakes, suggesting that this type of level crossing analysis can be used to predict the potential for a grain of sediment to scour due to variations of shear stress above a predefined threshold. Two thresholds will be evaluated in this analysis: (1) the mean approach flow shear stress, as predicted in Chapter 7, which will be used to show whether the insertion of a vertical object in the path of the flow leads to any increase of shear stress at all; and (2) four times the approach flow shear stress, which will be used

to evaluate the potential for the sediment to scour due solely to an increase in shear stress and verify the proposed hypothesis.

8.4.1 Spectral Density Function/Frequency Content

Determining if the signal measured with the shear sensor has any periodicity is a way of interpreting if the vortex can be felt on the channel bottom. In order to determine this, the frequency with which the threshold is reached and exceeded must be known. This analysis can be accomplished by mapping the time signal of shear stress values into a frequency domain, via a Fast Fourier Transform of the data string. The result of this transform is known as the spectral density function. Any peaks that are present, when plotting the spectral density function, show the dominant frequencies of the shear signal. The presence of a single, multiple or no peaks then can be used to ascertain if the signal is random, quasi-periodic, or periodic, where a random signal would indicate the lack of the vortex, since it has been shown to oscillate in front of the pier whenever present. A purely periodic signal would indicate the pure presence of the oscillating vortex. The degree to which the signal is random or periodic can be determined through its frequency content, which is a dimensionless ratio between zero and one and calculated based on the zero, first and second order moments of the spectral density function (Equation 16).

$$\delta_y = \sqrt{1 - \frac{\lambda_{1,y}^2}{\lambda_{0,y}\lambda_{2,y}}} \quad (16)$$

where: δ = Frequency content
 $\lambda_{1,y}$ = First order moment of spectral density function
 $\lambda_{0,y}$ = Zero order moment of spectral density function
 $\lambda_{2,y}$ = Second order moment of spectral density function

and

$$\lambda_{i,y} = \int_0^{\infty} \omega^i G(\omega) d\omega \quad (17)$$

where: $\lambda_{i,y}$ = Spectral density moment
 ω = Frequency (Hz)
 $G(\omega)$ = Spectral density function

The frequency content of each data set was found and plotted as a function of the approach flow Froude number (Figure 8.4).

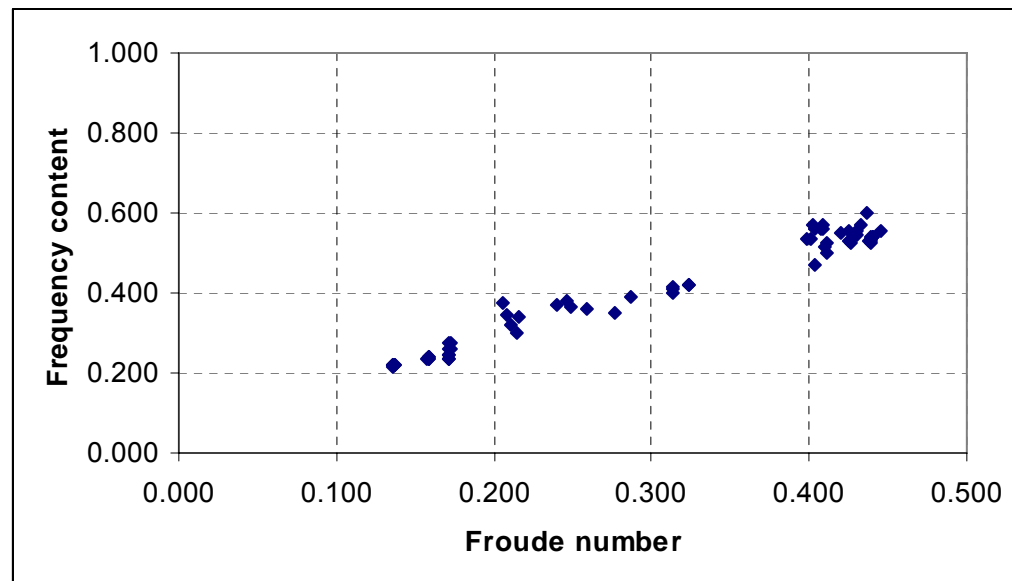


Figure 8.4 – Frequency content from each data set vs. approach flow Froude number

8.4.1.1 Analysis

A frequency content equal to 0 indicates a pure sine wave in which all the measurements are centered on one central frequency. A frequency content equal to 1 is found when there is no dominant frequency, and all of the frequencies are equally distributed. The vortex (when present) has been shown by many investigators (Shen et al. 1966a, Melville and Raudkivi 1977, Baker 1980, etc.) to be quasi-periodic. If the vortex were purely periodic (oscillated back and forth in front of the pier and never shed) it would produce a shear signal, over a small area in front of the pier, very similar to that of a sine wave (Figure 8.5). If the vortex was quasi-periodic (formed, moved upstream, then shed downstream), it would theoretically produce a time signature similar to Figure 8.6. If the vortex was not present at all, or if its presence was not felt on the channel bottom, then the shear stress time signature would be similar to Figure 8.7.

The frequency content can be used as a tool to distinguish between which of the two mechanisms is dominating at the base of the pier, the vortex or the diving current. Figure 8.4 shows the frequency content of each experiment to be highly dependent on the approach flow Froude number, and that as the Froude number increases, the time signal of the shear measurements transitions from being nearly periodic to quasi-periodic, based on the definition of frequency content and its range. The diminishing periodicity of the signal can be caused by one of three scenarios: (a) the vortex is becoming unsteady, leading to oscillations around multiple frequencies; (b) the vortex's existence is sparse and

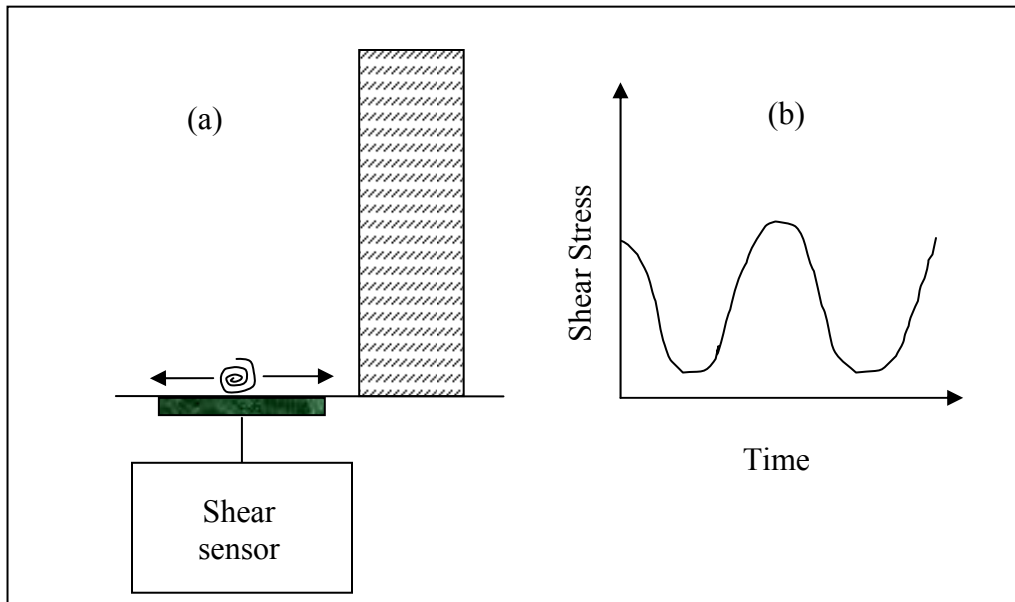


Figure 8.5 – (a) Hypothetical depiction of the vortex at the base of a pier oscillating back and forth and never shedding downstream; (b) associated time variation of shear stress due to vortex as read by shear sensor resulting in a frequency content of 0

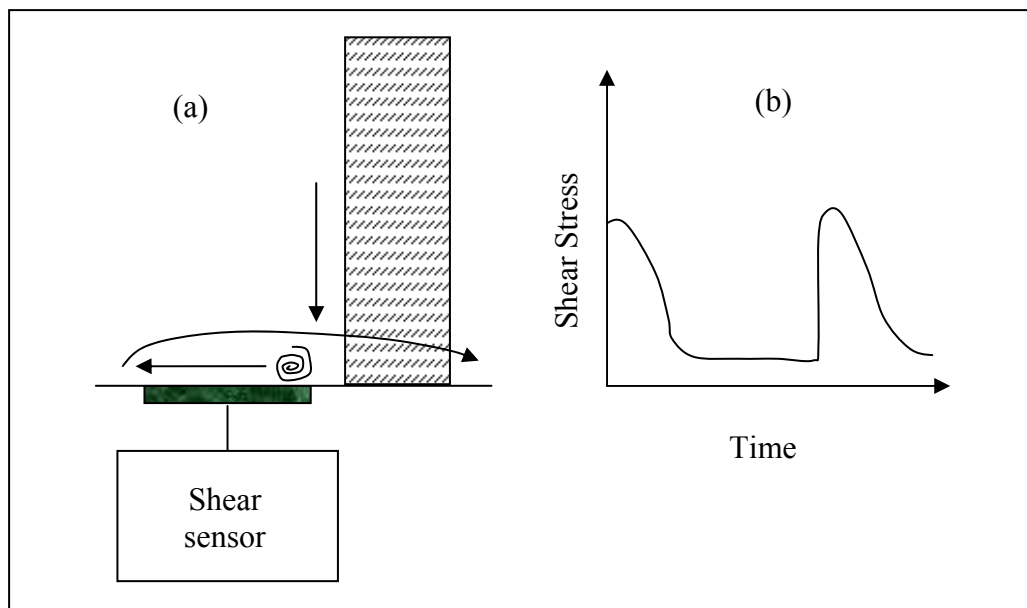


Figure 8.6 – (a) Hypothetical depiction of the diving current and a quasi-periodic vortex at the base of a pier moving upstream then shedding downstream; (b) associated time variation of shear stress due to the diving current and the vortex, as read by shear sensor, resulting in frequency content greater than 0 but less than 1

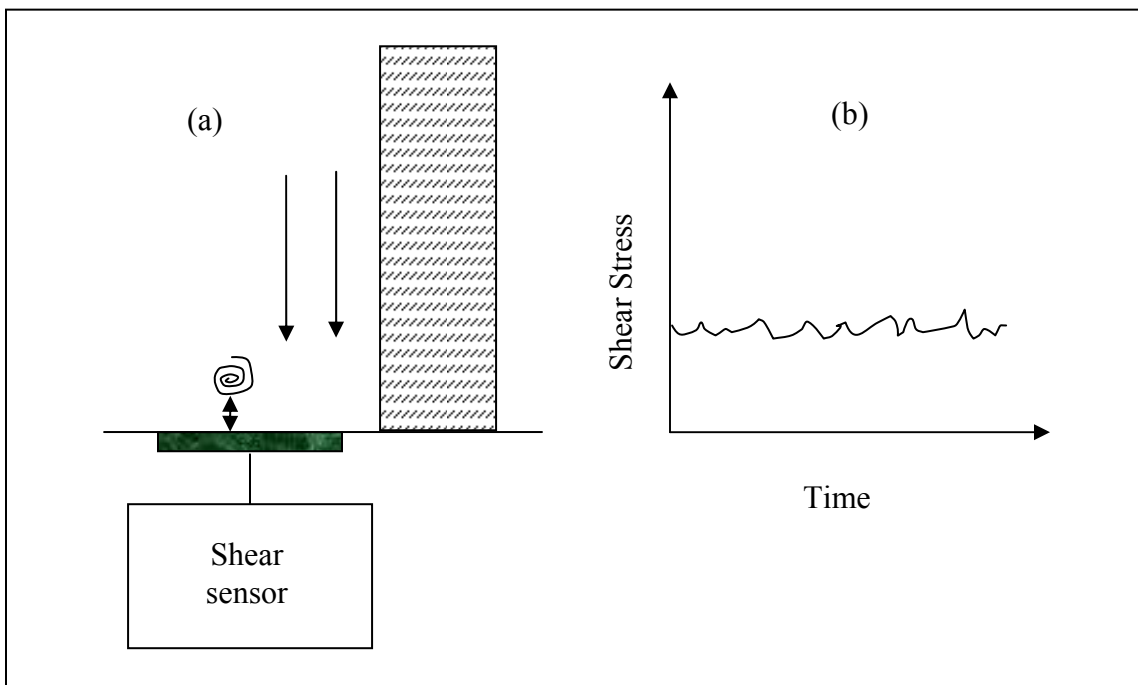


Figure 8.7 – (a) Hypothetical depiction of the diving current and vortex not felt on the channel bottom thereby not leading to any significant variation of shear stress with time; (b) associated time variation of shear stress as read by shear sensor, resulting in a frequency content of 1

the flow field is dominated by the presence of the diving current; or (c) the vortex is present but its affects are not being felt on the channel bottom. Because measurements were taken on the channel bottom, no conclusions can be drawn as to whether or not the vortex is not being felt on the channel bottom at these higher Froude numbers. Also, because the frequency content at higher Froude numbers is still in a quasi-periodic range and not close to a value of one, the likelihood that the flow field is dominated by the diving current is small. The conclusion, therefore, is that the vortex becomes unsteady as the Froude number increases. This conclusion is supported by the work of Grecco (1990), who

showed that the vortex undergoes a series of stages based on approach flow conditions, with two of the stages being simple oscillation and irregular unsteady motion. The final stage is the complete washing away of the vortex.

To summarize, the results of the frequency content analysis show that at lower Froude numbers, the shear measurements have an almost purely periodic signal which can be interpreted that the vortex is present. However, as the Froude number increases, the signal becomes quasi-periodic, leading to the conclusion that the vortex is becoming unsteady or possibly non-existent if the Froude number becomes high enough.

8.4.2 Probability of Exceedence

The probability that the approach shear will be exceeded can be computed once the statistical distribution of the data string is known. A commercial software package known as “BestFit” (Palisade Corporation 2002) was used to analyze the data and ultimately determine the most common statistical distribution of the data. The “BestFit” program uses several statistical methods for determining the best distribution of the data. The results from each method are displayed and a ranking of each distribution is given for each testing method. In each data set, the normal distribution was shown to rank either first or second for the best fit of the data, with approximately 90 percent of the time being the best rank. A typical distribution is shown in Figure 8.8.

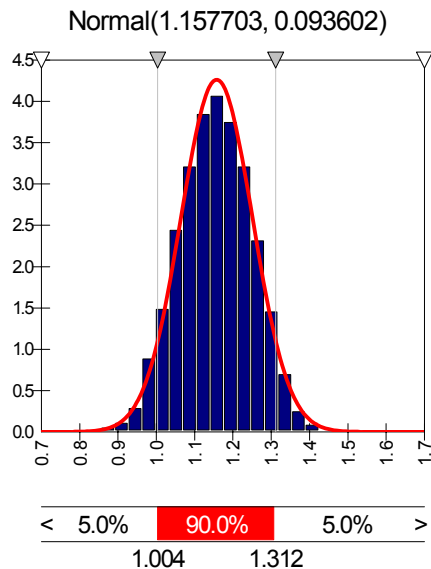


Figure 8.8 – Histogram of a representative data set showing a typical normal distribution with corresponding mean and standard deviation

Two statistical parameters are used in order to validate a normal distribution: skewness and Kurtosis. The skewness of a data set identifies whether the data, after being arranged into a histogram, is more heavily weighted to either the right (negative) or left (positive) side of the mean value. A skewness of zero would indicate that there is the same number of data points both below and above the mean value of the data. The skewness for each data set was calculated and varied between -0.1 and +0.3. This range of skewness shows that the data centers very well around the mean value, which is expected according to the Central Limit Theorem.

The Kurtosis is another parameter which helps to identify if the data string has a normal distribution. A Kurtosis of 3 represents a perfect normal distribution. The Kurtosis for each data set was evaluated and showed to vary

from 2.6 to 3.3. This is a narrow range and therefore supports the use of normal distribution equations for calculating exceedence probabilities.

The probability that a single shear value out of an entire data string from an experimental data set having a normal distribution will exceed the established threshold is based on the standard normal variant, which can be calculated using Equation (18).

$$\phi = \frac{\tau_{threshold} - \tau_{mean(data_set)}}{\tau_{st.dev.(data_set)}} \quad (18)$$

Where: Φ = Standard normal variant
 $\tau_{threshold}$ = Approach flow shear stress (Pa)
 τ_{mean} = Mean shear stress of data string (Pa)
 $\tau_{st.dev.}$ = Standard deviation of data string (Pa)

Once the standard normal variant is known, normal distribution tables are used to determine the corresponding probability. The probability of exceedence of a single measurement above the threshold, for each trial as a function of the approach flow Froude number, was determined based on the standard normal variant of each data set (Figure 8.9).

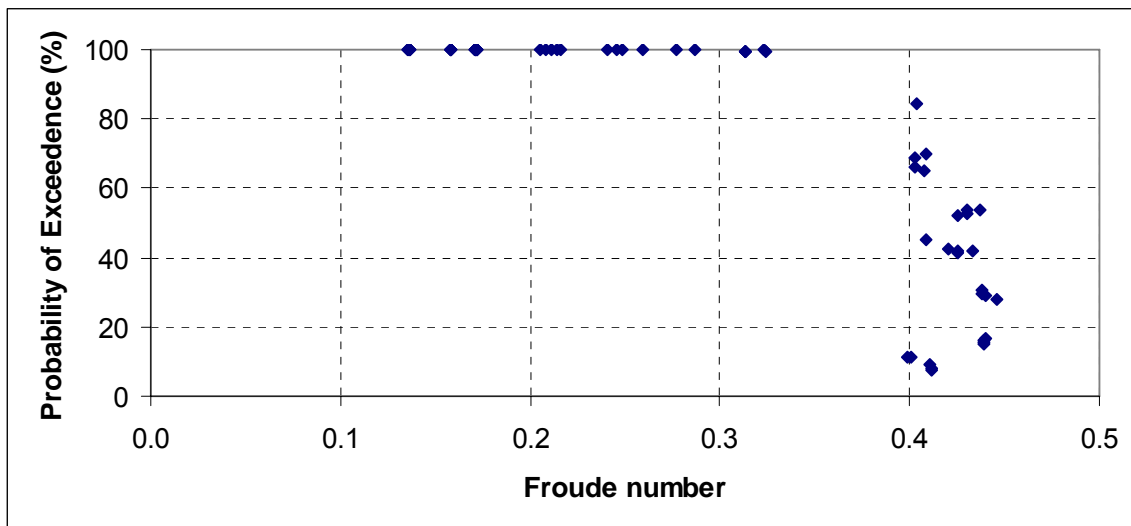


Figure 8.9 - Probability that a single shear measurement from each data set will exceed the approach flow shear threshold

8.4.2.1 Analysis

Two distinct trends are observed when analyzing Figure 8.9. For Froude numbers less than 0.33, the probability that the threshold will be exceeded is nearly 100 percent. However, for Froude numbers greater than 0.40, a very sharp drop-off occurs and the exceedence probability appears to be independent of Froude number. The presence of two independent trends was not expected so the hydraulic conditions of each trial were evaluated to determine if a similar shallow depth phenomenon was occurring which was observed during the unobstructed flow experiments discussed in Chapter 7. The probabilities were plotted as a function of the depth of flow for each trial (Figure 8.10). The results show that the depth of water never drops below the 1 inch threshold explained in Chapter 7, ruling out the possibility that the shear

measurements were being distorted due to increased surface tension caused by the shallow depths. However, it is interesting to note that there is a strong increasing correlation between depth and the probability of exceedence for depths ranging from 1 inch to 1.5 inches. Once the depth reaches approximately 1.75 inches, the probability of exceedence stays at nearly 100 percent. In terms of a dimensionless length ratio (depth/pier width), 1.75 inches corresponds to approximately 0.6 (Figure 8.11).

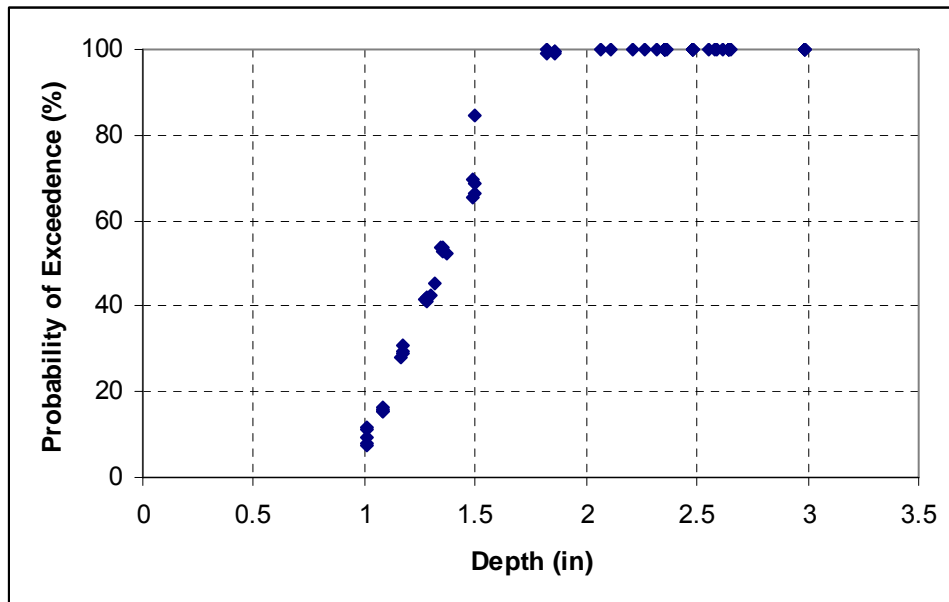


Figure 8.10 – Probability that a single measurement will exceed the approach flow shear threshold as a function of depth

The sudden drop off of exceedence probability at lower depths is due to what is known as a “wide pier” effect. A wide pier is one where the pier width is sufficiently wide compared to the water depth which in turn does not allow the system of vortices to fully develop. The phenomenon typically is accepted to

occur when the length ratio of depth to pier width is less than 0.8 (Johnson 1999). The threshold ratio observed as part of this study actually is less than 0.8 and closer to 0.6. Regardless, the wide pier phenomenon appears to be present for Froude numbers greater than 0.4 ($Y/B < 0.6$) and explains the presence of the two trends observed in Figure 8.9 – at lower Froude numbers, the vortex is completely developed and increases shear on the channel bottom nearly all of the time; at higher Froude numbers the vortex only partially develops, and increases of shear stress above the threshold are felt during times when a vortex is present.

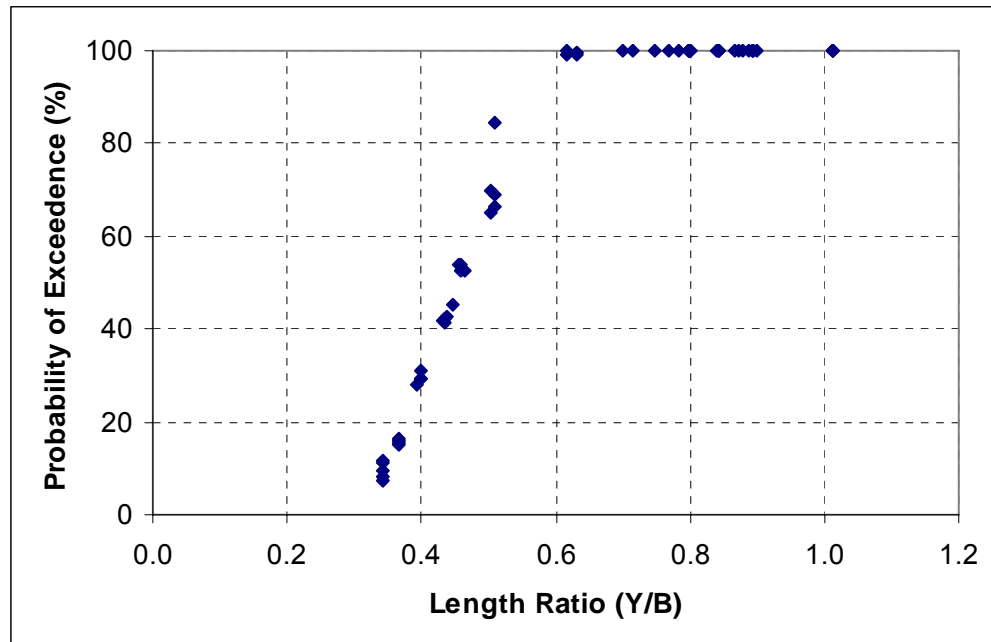


Figure 8.11 – Probability of exceedence of one shear measurement exceeding the threshold as a function of the length ratio of depth of flow to pier width, showing the presence of the wide pier phenomenon to occur at $Y/B < 0.6$

Because the wide pier phenomenon inhibits the full formation of the vortex system at the base of the pier, and since the intent of this work is to determine if the vortex alone is capable of initiating scour, the following results sections will analyze only data from Froude numbers ranging up to 0.33, where it is assumed that the vortex system is fully developed. This will eliminate possible distortions in analysis (and subsequent conclusions) caused by the wide pier phenomenon.

8.4.3 Percent of Time Threshold is Exceeded

The rate of threshold exceedence is a measure of how often the shear signal exceeds the threshold in any given second. It can be found by summing the total number of times a single measurement exceeds the threshold and then dividing this number by duration of the entire measurement (60 seconds). Because this value is sampling rate dependent, a better evaluator of threshold exceedence is the percentage of time the threshold is exceeded. This percentage can be found by dividing the rate of threshold exceedence by the sampling rate of the measurements (200 samples per second). Table 8.1 lists the hydraulic properties for each obstructed flow experiment with corresponding time percentage exceedence. Figure 8.12 shows the time percentage of shear exceedence above the threshold as a function of the approach flow Froude number.

Table 8.1 – Obstructed flow hydraulic conditions with time percentage of threshold exceedence

Trial Name	Flow (lps)	Depth (cm)	Velocity (cm/s)	Fr #	Threshold Shear (Pa)	# Samples above Threshold	Time %
60_7H	2.8	6.0	10.4	0.14	0.24	12000	100
60_5H	2.8	6.0	10.4	0.14	0.24	12000	100
60_4H	2.8	6.0	10.4	0.14	0.24	12000	100
60_6H	2.9	6.0	10.5	0.14	0.24	12000	100
60_8H	2.9	6.0	10.5	0.14	0.24	12000	100
70_5H	3.6	6.3	12.4	0.16	0.26	12000	100
70_4H	3.6	6.3	12.5	0.16	0.26	12000	100
70_6H	3.6	6.3	12.5	0.16	0.26	12000	100
70_7H	3.6	6.3	12.5	0.16	0.26	12000	100
70_8H	3.6	6.3	12.5	0.16	0.26	12000	100
94_5H	5.1	7.6	14.8	0.17	0.27	12000	100
94_6H	5.1	7.6	14.8	0.17	0.27	12000	100
94_4H	5.1	7.6	14.8	0.17	0.27	12000	100
94_7H	5.1	7.6	14.8	0.17	0.27	12000	100
80_6H	4.3	6.7	13.9	0.17	0.27	12000	100
80_7H	4.3	6.7	13.9	0.17	0.27	12000	100
80_4H	4.3	6.7	14.0	0.17	0.27	12000	100
80_5H	4.3	6.7	14.0	0.17	0.27	12000	100
94_5L	5.1	6.7	16.7	0.21	0.29	12000	100
90_2L	4.9	6.5	16.6	0.21	0.29	12000	100
94_4L	5.2	6.6	17.0	0.21	0.30	12000	100
94_1L	5.2	6.6	17.2	0.21	0.30	12000	100
94_3L	5.2	6.6	17.3	0.22	0.30	12000	100
90_4L	4.9	5.9	18.3	0.24	0.31	12000	100
94_2L	5.2	6.0	18.9	0.25	0.31	12000	100
90_6L	4.9	5.8	18.7	0.25	0.32	12000	100
90_1L	4.9	5.6	19.2	0.26	0.32	12000	100
90_5L	4.9	5.4	20.1	0.28	0.33	12000	100
90_3L	4.9	5.2	20.6	0.29	0.33	12000	100
85_1L	4.6	4.7	21.4	0.31	0.34	11864	99
85_2L	4.6	4.7	21.4	0.31	0.34	11927	99
85_4L	4.6	4.7	21.4	0.31	0.34	11868	99
85_5L	4.6	4.6	21.8	0.32	0.34	11915	99
85_3L	4.6	4.6	21.8	0.32	0.34	11953	100

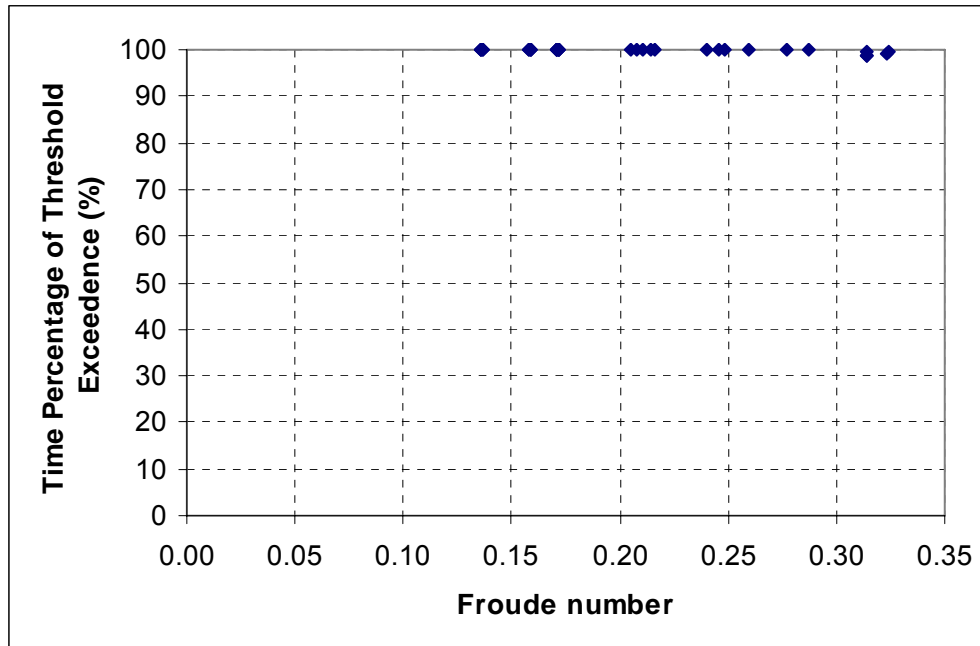


Figure 8.12 – The percentage of time that the approach flow shear stress threshold was exceeded during each experiment as a function of the approach flow Froude number

8.4.3.1 Analysis

As seen in Figure 8.12, the threshold is almost always exceeded for Froude numbers less than 0.33 (no wide pier effect). The fact that the threshold is always exceeded means that the vortex must always be present and felt on the channel bottom. The reason for this is that between the two mechanisms present in front of a pier, the vortex is the only one that can increase shear on the channel bottom. The diving current acts in the normal direction to the channel bottom and therefore is not capable to increasing shear (a tangential quantity).

8.4.4 Mean Clump Time

A group of shear measurements contained between two distinguishable boundaries, most or all of which exceed the threshold can be considered to be a clump (Figure 8.13). A clump of shear measurements exceeding the threshold is much more likely than just a single burst to initiate the displacement of particles. The time at which a clump of measurements surpasses the threshold can be computed by summing the total number of measurements in a particular group and then dividing by the sampling rate of the measurements (200 Hz), or through visual inspection of a time series plot of shear vs. time for each individual trial (Figure 8.13). The average size and time duration of each clump was determined for each data set. The average time per clump for each data set is plotted as a function of the approach flow Froude number in Figure 8.14.

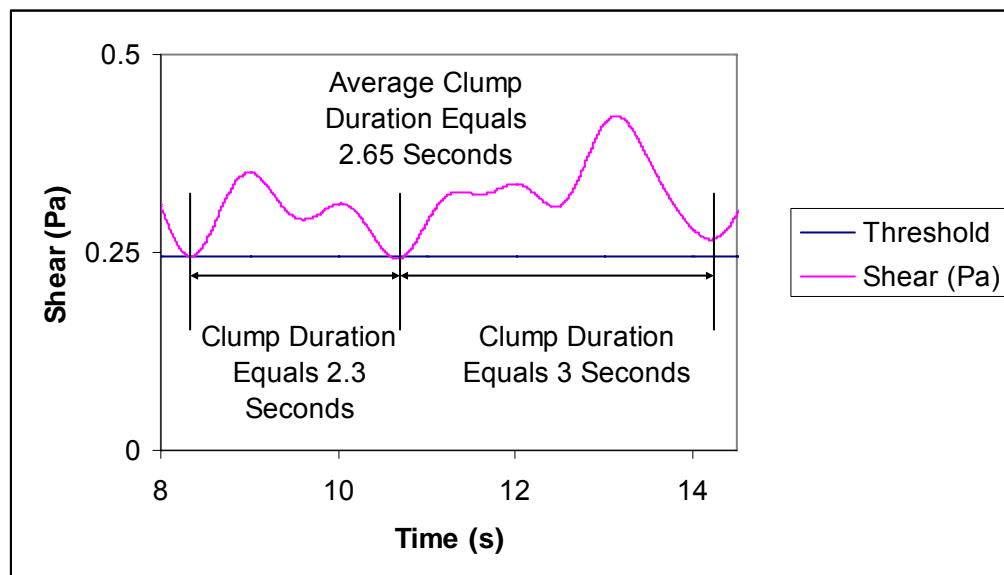


Figure 8.13 –Typical data set showing how the total average duration of a clump of measurements above the threshold was obtained

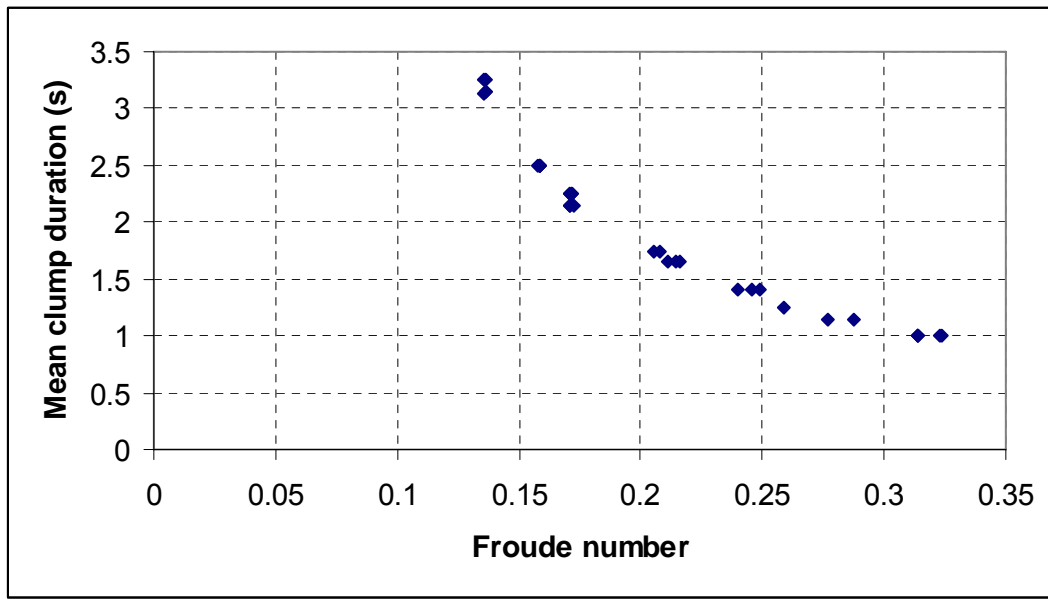


Figure 8.14 – Average duration of all clumps from each individual experiment as a function of the approach flow Froude number

8.4.4.1 Analysis

Figure 8.14 shows a decay function of the mean duration per clump for each data set as a function of the Froude number. At the lower Froude number range, a duration of more than 3 seconds is achieved. A clump lasting 3 seconds is indicative of a strong primary vortex dominating the flow field before eventually shedding downstream. As the Froude number increases to 0.33, the mean duration decays in an exponential manner down to approximately 1 second. The transition of the decaying duration of each clump indicates that the vortex begins to oscillate at a faster pace as the Froude number is increased. Additionally, the average time for each clump can be considered analogous to the duration which a particular vortex oscillates in front of the pier and over the shear sensor before eventually shedding downstream. This would indicate that

the shedding frequency for Froude numbers ranging from 0.13 to 0.33 is on the order of .33 to 1.0 cycles per second. This is in good agreement with the results of Vautier (1972), who reported a typical shedding frequency of 0.25 to 0.50 cycles per second for each primary vortex.

8.5 Shear Amplification

The preceding sections have shown the vortex to be present nearly 100 percent of the time, if the pier is not wide compared to the depth of flow. The question that arises is whether the vortex creates enough shear stress on the channel bottom to initiate scour. In order to answer this question, the amount of shear amplification between the approach flow threshold and the values measured in front of the obstruction need to be assessed. Two parameters were evaluated: (1) the average shear intensity amplification above the threshold (described below), and (2) the typical peak shear amplification.

The average shear intensity is a measure of a typical or average shear value above the approach flow threshold (Figure 8.15). Its importance stems from the recognition that while a single burst of shear (peak shear) may cause a few particles of sediment to transport, it is a prolonged increase of shear (average shear intensity) which has the potential to sustain the scouring mechanism over time. The average shear intensity can be computed based on a formula used to calculate the average turbulence intensity, used in finding turbulence dispersion rates. The formula is shown in Equation (19). The average shear intensity amplification then would be equal to the average shear intensity divided by the

predefined shear threshold (Equation 20). The peak shear amplification is then the “typical peak” shear (Figure 8.16) divided by the threshold (Equation 21). The “typical peak” shear is the average of the highest peak shear values from each clump and was used because it best represents the peak shear encountered for each trial rather than the absolute maximum peak shear value.

$$\tau_{avg_int} = \frac{\sqrt{\tau'^2}}{\tau_{threshold}} \quad (19)$$

where: τ_{avg_int} = Average shear intensity
 τ' = Shear fluctuation above threshold (Pa)
 $\tau_{threshold}$ = Shear threshold (Pa)

$$\tau_{avg_int_amp} = \frac{\tau_{avg_int}}{\tau_{threshold}} \quad (20)$$

where: $\tau_{avg_int_amp}$ = Average shear intensity amplification
 τ_{avg_int} = Average shear intensity (Pa)
 $\tau_{threshold}$ = Approach flow shear threshold (Pa)

$$\tau_{peak_amp} = \frac{\tau_{typical_peak}}{\tau_{threshold}} \quad (21)$$

where: τ_{peak_amp} = Peak shear amplification
 $\tau_{typical_peak}$ = Typical peak shear (Pa)
 $\tau_{threshold}$ = Approach flow shear threshold (Pa)

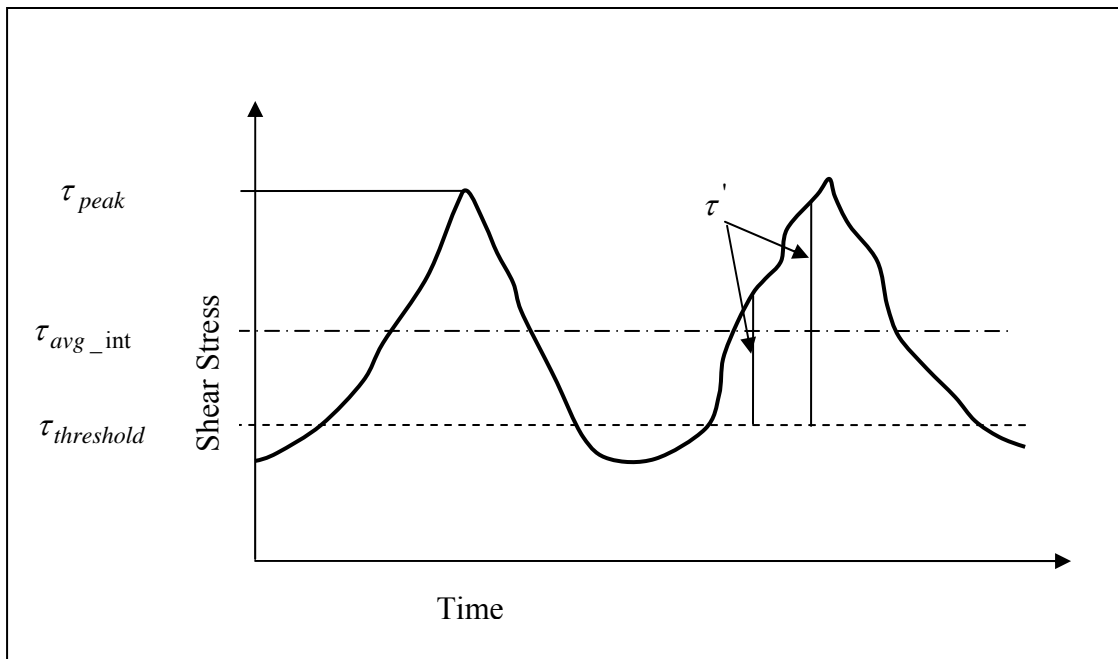


Figure 8.15 – Hypothetical schematic of the variation of shear stress with time showing the differences between peak shear, average shear intensity, shear fluctuation above the threshold and shear threshold

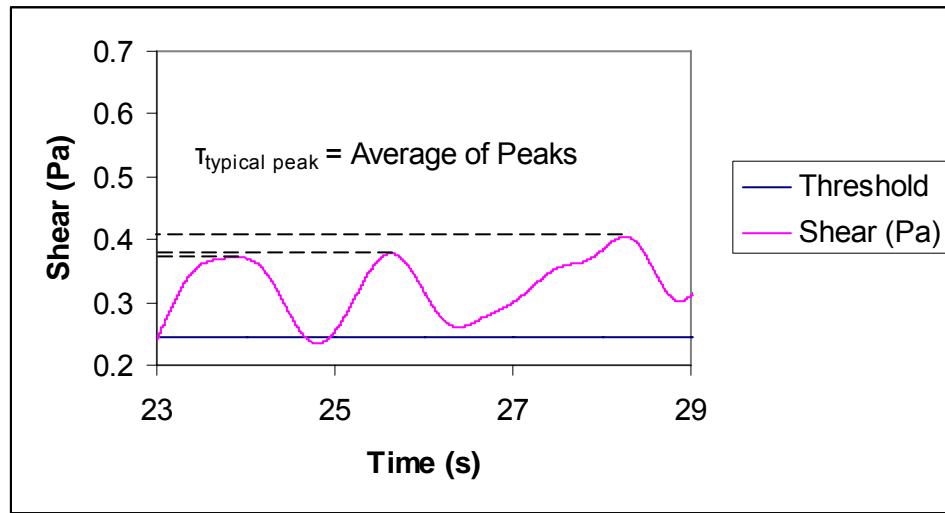


Figure 8.16 – Visual representation of method used to determine the typical peak shear for each trial

The uncertainty of each amplification was also calculated based on Equation (22) (Holman 1989). The typical peak shear amplification and average shear intensity amplification for each trial were found and are plotted in Figure 8.17. The amplifications with corresponding uncertainty are shown in Figures 8.18 and 8.19. The amplifications with corresponding uncertainty are listed in Table 8.2.

$$\Delta y = y \sqrt{\left(\frac{\Delta x_1}{x_1} \right)^2 + \left(\frac{\Delta x_2}{x_2} \right)^2} \quad (22)$$

where:

Δy	= Uncertainty of amplification
y	= Amplification value
Δx_1	= Maximum error of measurement = 0.05 Pa
x_1	= Shear measurement (peak or intensity) (Pa)
Δx_2	= Maximum error of shear threshold = 0.05 Pa
x_2	= Shear threshold (Pa)

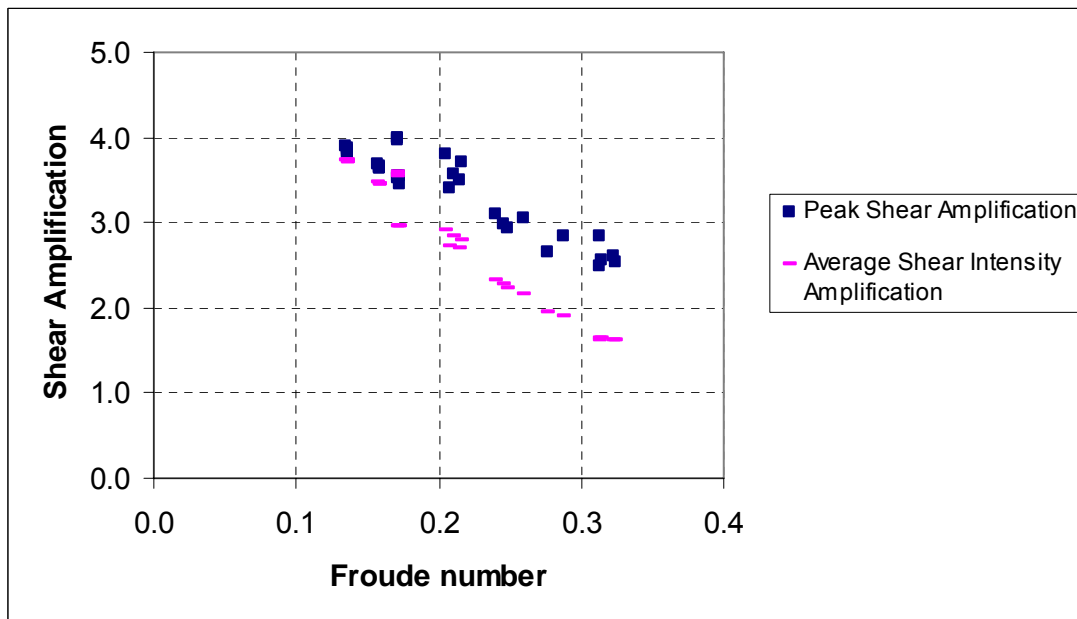


Figure 8.17 – Typical peak shear amplification and average shear intensity amplification of each trial as a function of the approach flow Froude number

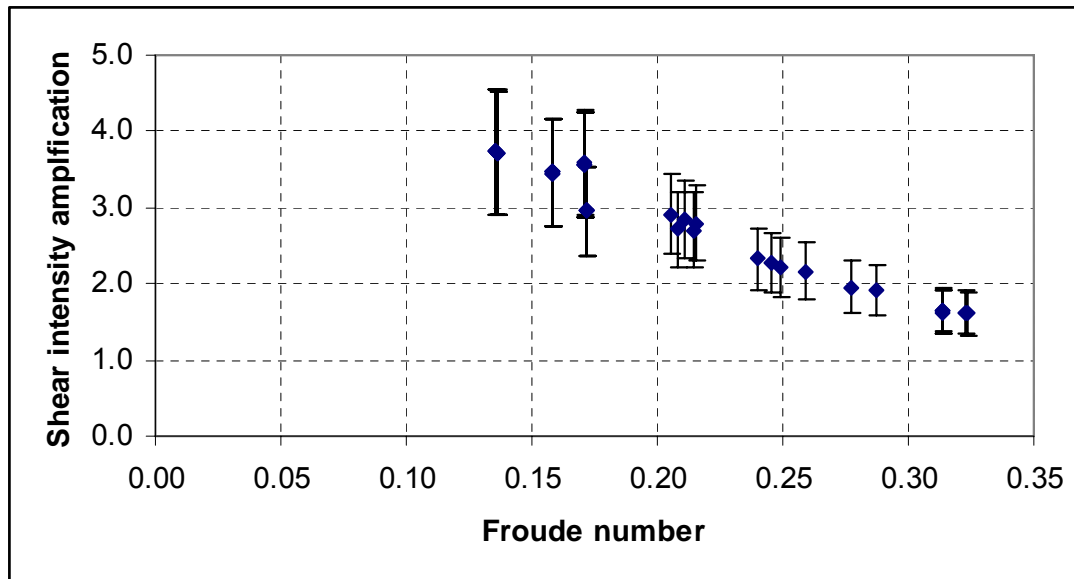


Figure 8.18 – Average shear intensity amplification with corresponding uncertainty

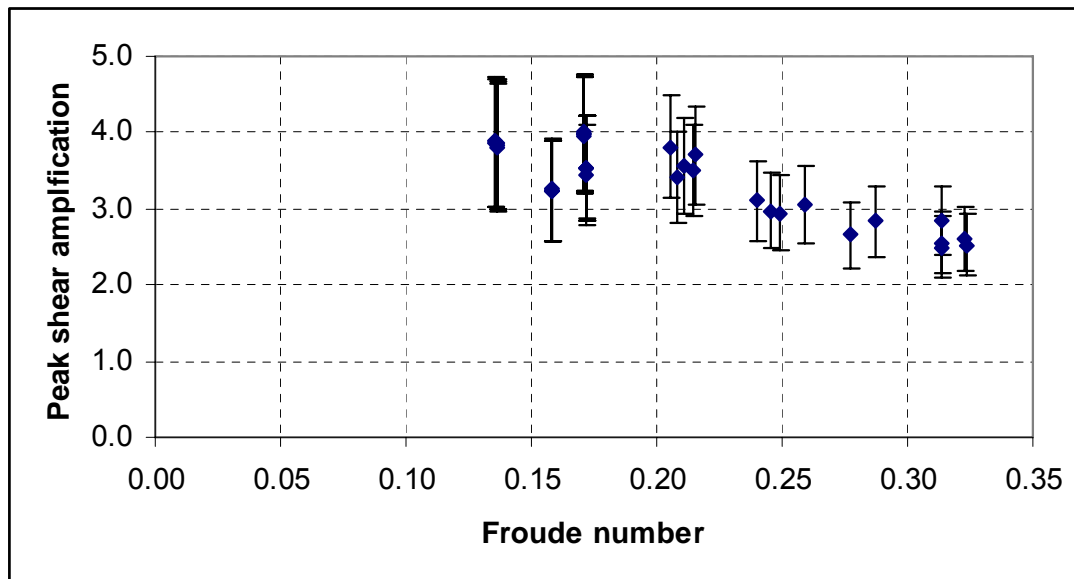


Figure 8.19 – Peak shear amplification with corresponding uncertainty

Table 8.2 – Peak shear and average intensity shear amplifications with corresponding uncertainties

Froude Number	Peak Amplification	Peak Uncertainty	Shear Intensity Amplification	Shear Intensity Uncertainty
0.14	3.9	0.9	3.7	0.8
0.14	3.9	0.8	3.7	0.8
0.14	3.8	0.8	3.7	0.8
0.14	3.8	0.8	3.7	0.8
0.14	3.8	0.8	3.7	0.8
0.16	3.2	0.7	3.5	0.7
0.16	3.2	0.7	3.5	0.7
0.16	3.2	0.7	3.5	0.7
0.16	3.2	0.7	3.5	0.7
0.17	4.0	0.8	3.6	0.7
0.17	4.0	0.8	3.6	0.7
0.17	4.0	0.8	3.6	0.7
0.17	3.5	0.7	3.0	0.6
0.17	3.5	0.7	3.0	0.6
0.17	3.4	0.7	3.0	0.6
0.17	3.5	0.7	3.0	0.6
0.21	3.8	0.7	2.9	0.5
0.21	3.4	0.6	2.7	0.5
0.21	3.6	0.6	2.8	0.5
0.21	3.5	0.6	2.7	0.5
0.22	3.7	0.6	2.8	0.5
0.24	3.1	0.5	2.3	0.4
0.25	3.0	0.5	2.3	0.4
0.25	2.9	0.5	2.2	0.4
0.26	3.1	0.5	2.2	0.4
0.28	2.7	0.4	2.0	0.3
0.29	2.8	0.5	1.9	0.3
0.31	2.5	0.4	1.7	0.3
0.31	2.8	0.4	1.6	0.3
0.31	2.6	0.4	1.6	0.3
0.32	2.6	0.4	1.6	0.3
0.32	2.5	0.4	1.6	0.3

8.5.1 Analysis

Peak shear amplification values vary between 2.5 (+/- 0.4) and just below 4 (+/- 0.9) with a decreasing trend as the Froude number increases. Average shear intensity amplification values vary between 1.6 (+/- 0.3) and 3.7 (+/- 0.8) with a decreasing trend with increasing Froude number. Interestingly, at lower Froude numbers there are only slight variations between the peak value amplification and the average shear intensity amplification (approximately 3.8 vs. 3.7 – Froude number = 0.14). This implies a sustained duration of the peak shear stress values which could be attributed to a relatively slowly oscillating vortex. These results coincide with the findings in Section 8.4.4 (Mean Clump Time), which showed that at lower Froude numbers the duration of each clump (vortex) was longest. Visual inspection of the shear signal also showed a flattened clump peak at lower Froude number trials. As the Froude number increases, the amplification values decrease at different rates, creating a greater disagreement (approximately 2.5 vs. 1.6 – Froude number = 0.323). Visual inspection of the shear signal with time showed a narrower peak occurring for a shorter duration of time at higher Froude numbers, with respect to the shape and duration at lower Froude numbers. This narrower peak with shorter duration suggests that once the vortex is formed it quickly begins to oscillate and shed. Again this result is corroborated by the findings in Section 8.4.4 (Mean Clump Time).

It is worth noting that each of the amplifications is below the 4 times amplification level (disregarding uncertainty) established as the threshold by

which scour would be considered to initiate due to the vortex alone. This will be discussed in greater detail in the “Discussion” section (Section 8.6).

8.5.2 Shear Amplification – Sensor Offset Adjustment

A second shear amplification analysis was performed by adjusting all of the shear measurements by -0.2 Pa. The -0.2 Pa adjustment was made in order to better match the theoretical prediction of shear values in an unobstructed flow as discussed in Section (7.2.1). Equations (19-22) were used for calculating the peak shear amplification, average shear intensity amplification and corresponding uncertainties as in Section 8.5. Figures 8.20 and 8.21 show the results for the average shear intensity amplification with uncertainty and peak shear amplification with uncertainty. The results are also listed in Tables 8.3 and 8.4.

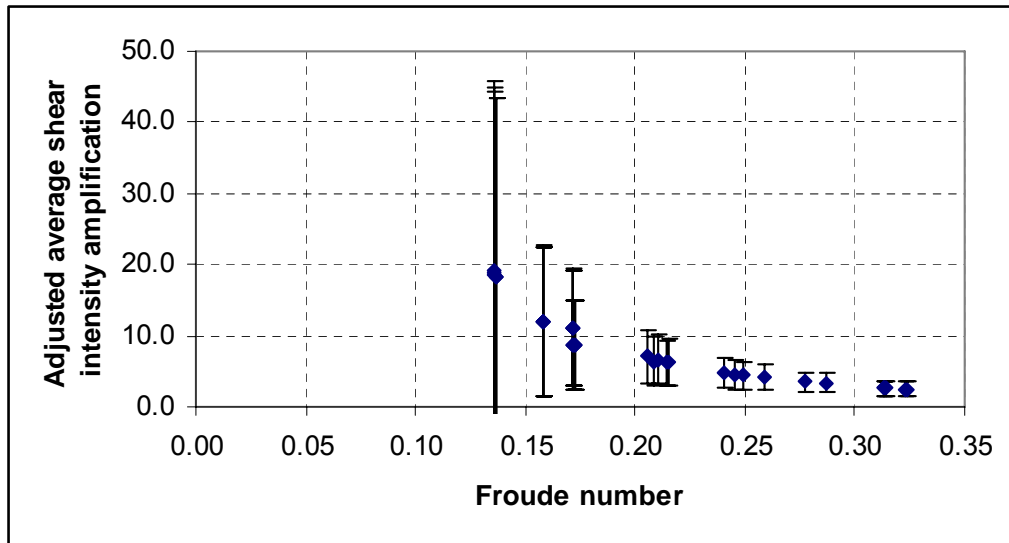


Figure 8.20 – Adjusted average shear intensity amplification with corresponding uncertainty

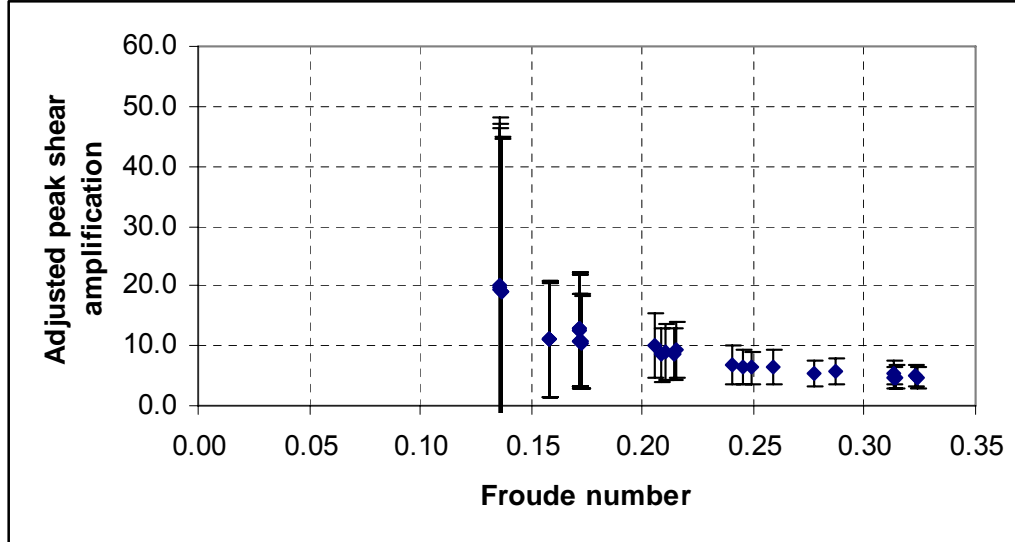


Figure 8.21 – Adjusted peak shear amplification with corresponding uncertainty

Table 8.3 – Adjusted threshold, peak, and average intensity shear values

Froude number	Adjusted threshold	Adjusted peak shear	Adjusted average shear intensity
0.14	0.04	0.72	0.68
0.14	0.04	0.71	0.68
0.14	0.04	0.71	0.68
0.14	0.04	0.71	0.68
0.14	0.04	0.70	0.68
0.16	0.06	0.63	0.60
0.16	0.06	0.63	0.60
0.16	0.06	0.64	0.61
0.16	0.06	0.64	0.61
0.16	0.06	0.63	0.58
0.17	0.07	0.87	0.75
0.17	0.07	0.86	0.76
0.17	0.07	0.87	0.77
0.17	0.07	0.87	0.76
0.17	0.07	0.75	0.60
0.17	0.07	0.75	0.60
0.17	0.07	0.73	0.60
0.17	0.07	0.75	0.60
0.21	0.09	0.92	0.65
0.21	0.09	0.80	0.60
0.21	0.10	0.85	0.64
0.21	0.10	0.84	0.61
0.22	0.10	0.91	0.63
0.24	0.11	0.77	0.53
0.25	0.11	0.73	0.52
0.25	0.12	0.73	0.50
0.26	0.12	0.78	0.49
0.28	0.13	0.67	0.44
0.29	0.13	0.73	0.43
0.31	0.14	0.64	0.36
0.31	0.14	0.75	0.35
0.31	0.14	0.66	0.35
0.32	0.14	0.68	0.35
0.32	0.14	0.66	0.35

Table 8.4 – Adjusted peak shear and average intensity shear amplification with corresponding uncertainty

Froude number	Adjusted Peak Amplification	Adjusted peak uncertainty	Adjusted Shear Intensity Amplification	Adjusted Shear Intensity Uncertainty
0.14	20.1	28.2	19.1	26.8
0.14	19.7	27.3	18.8	26.1
0.14	19.5	26.9	18.7	25.7
0.14	19.1	25.9	18.4	24.9
0.14	19.0	25.7	18.4	24.9
0.16	11.0	9.7	10.1	8.7
0.16	11.0	9.6	10.0	8.5
0.16	11.1	9.6	10.0	8.4
0.16	11.0	9.6	10.0	8.5
0.16	11.0	9.6	10.0	8.4
0.17	12.8	9.4	11.0	8.1
0.17	12.6	9.3	11.1	8.1
0.17	12.8	9.4	11.2	8.2
0.17	12.7	9.3	11.1	8.1
0.17	10.9	7.9	8.6	6.3
0.17	10.9	7.9	8.7	6.3
0.17	10.5	7.6	8.6	6.3
0.17	10.9	7.9	8.6	6.3
0.21	9.9	5.4	7.0	3.8
0.21	8.5	4.5	6.4	3.4
0.21	8.9	4.7	6.7	3.5
0.21	8.6	4.4	6.2	3.2
0.22	9.2	4.7	6.4	3.3
0.24	6.9	3.1	4.7	2.2
0.25	6.4	2.9	4.5	2.0
0.25	6.3	2.8	4.4	1.9
0.26	6.5	2.8	4.1	1.8
0.28	5.3	2.1	3.5	1.4
0.29	5.7	2.2	3.3	1.3
0.31	4.7	1.8	2.6	1.0
0.31	5.5	2.1	2.6	1.0
0.31	4.8	1.8	2.6	1.0
0.32	4.9	1.8	2.5	1.0
0.32	4.7	1.8	2.5	1.0

8.5.2.1 Analysis

Peak shear amplification values vary between 20.1 (+/- 28.2) and 4.7 (+/- 1.8) with a decreasing trend as the Froude number increases. Average shear intensity amplification values vary between 19.1 (+/- 26.8) and 2.5 (+/- 1.0) with a decreasing trend with increasing Froude number. Just as in the case of there being no offset adjustment, the peak value amplification and the average shear intensity amplification are relatively close to one another at lower Froude numbers (approximately 20.1 vs. 19.1 – Froude number = 0.14). There is a more pronounced decrease of shear amplification with increasing Froude number in the adjusted shear value situation as opposed to the non-adjusted case. Interestingly, all of the adjusted peak shear amplification values are above the 4 times amplification criteria set to indicate whether the vortex alone has the potential to solely initiate scour, which is contrary to the results obtained without the offset adjustment.

8.5.3 Comparison to Historical Results

8.5.3.1 Melville and Raudkivi (1977)

Melville and Raudkivi (1977) performed an extensive study of the flow characteristics in the vicinity of vertical obstructions. As part of their investigation they ascertained a shear stress distribution in front of and around a pier at an elevation of 2 mm. The flow characteristics of their study were as follows: mean velocity = 0.25 m/s, uniform flow depth = 0.15 m, Froude number = 0.206, and bed slope = 0.0001. They also reported an approach flow shear velocity equal to

.0121 m/s calculated from Equation (23). Using this value of shear velocity, the approach flow shear stress was calculated according to Equation (10) and found to equal 0.146 Pa.

$$u_* = \sqrt{gy_o S_o} \quad (23)$$

where: u_* = Shear velocity (m/s)
 g = Acceleration of gravity = 9.8 m/s²
 y_o = Uniform flow depth (m)
 S_o = Bed slope (m/m)

Mean shear stress values were calculated at various points in front of and around the pier by Melville and Raudkivi (1977) using Equation (24):

$$\bar{\tau} = K \frac{\bar{\Delta u}}{\Delta y} \quad (24)$$

where: $\bar{\tau}$ = Mean bed shear stress (Pa)
 K = Calibration constant obtained by comparing estimated shear values from Equation (23) with those obtained from the slope of the logarithmic velocity profile of the approach flow = 2
 $\bar{\Delta u}$ = Local mean velocity at 2 mm from bed
 Δy = 2 mm

Melville and Raudkivi (1977) report a decreasing shear stress distribution in front of the pier in the flow direction as the pier is approached. Shear stress values measured ranged from 0.04 Pa to 0.07 Pa, which can be normalized to the approach flow shear stress as 0.27 to 0.47 magnifications. These values are less than the approach flow shear stress and substantially different from the

values recorded as part of this work (approximately 3.5 peak shear magnification factor (non-offset adjustment) at a Froude number equal to 0.21). It was this measured reduction in shear stress that lead Melville and Raudkivi to conclude that scour is caused by the diving current reflecting off the pier and not an increase in shear stress caused by the vortex.

The method of shear stress measurement in front of the pier which Melville and Raudkivi employed is not adequate for such a conclusion. Their method involved using what is essentially Newton's law of viscosity based on an average velocity reading. This method has associated inherent errors. To begin, their method does not result in a shear stress calculation on the channel bottom; it was taken as 2 mm above the channel bottom as indicated earlier. Additionally, the method does not account for the turbulent stresses due to the velocity fluctuations of the flow field which might actually dominate the total shear stress value at this location due to the vortex. Finally, and most importantly, this method assumes that the flow field in front of a pier is constant.

Several investigators, as well as the results from this work, show that this is not the case, as the flow field is constantly changing due to the oscillatory nature of the vortex. Recording an average velocity from an oscillatory mechanism and using this value in a shear stress prediction should produce a diminished shear stress, because on average the velocity would be close to zero due to the velocity profile fluctuating between a positive and negative value due to the motion of the vortex (Figure 8.22). Analysis of the shear stress predictions associated with the greatest change in velocity gradient, instead of the average

velocity gradient, would probably be a better indicator of the shear stress values which might lead to scour and could possibly lead to a better comparison to the shear stress amplifications found in this work.

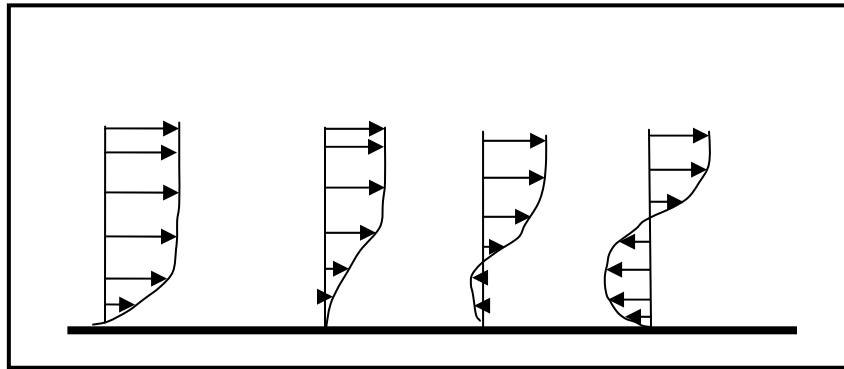


Figure 8.22 – Developing velocity profile due to the formation and oscillation of a vortex

8.5.3.2 Mendoza-Cabralles (1993)

Mendoza-Cabralles developed a $k-\epsilon$ closure model (where k is kinetic energy and ϵ is the energy dissipation rate) in an attempt to ascertain shear stress values on a flat bed around a cylinder. He simulated the experimental setup of Melville and Raudkivi (1977) for comparative purposes. His model predicted shear stress amplification values that were at the lower end of the values reported by Melville and Raudkivi (.27). However, Mendoza-Cabralles concluded that his model was not suitable for shear stress determination in front of an obstruction because, like Melville and Raudkivi's work, it only reports an average shear stress and “the $k-\epsilon$ closure model should be expected to yield

only an adequate description of the bulk flow, not the detailed resolution of the changing stresses" (Mendoza-Cabralles 1993, p 904).

8.5.3.3 Ahmed and Rajaratnam (1998)

Ahmed and Rajaratnam (1998) used a series of two three-tube Yaw probes as Preston probes in an attempt to measure bed shear stresses. The Preston probe gives a velocity profile of the flow, from which Newton's law of viscosity can be used to predict shear stresses. Ahmed and Rajaratnam (1998) do not give exact heights at which the measurements were taken, but claim the measurements are approximately "on the bed." Additionally, they do not state the nature of the velocities used for shear stress prediction (average - similar to Melville and Raudkivi's (1977) technique, or extremes). Measurements were taken both in an unobstructed and obstructed flow. Two experiments were completed using a smooth bed: Experiment 1 - mean velocity = 0.29 m/s, uniform depth = 0.19 m, Froude number = 0.22, approach flow shear stress = 0.18 Pa; Experiment 2 – mean velocity = 0.38 m/s, uniform depth = 0.14 m, Froude number = 0.33, approach flow shear stress = 0.32 Pa. The results of the shear stress measurements in front of the pier then were normalized by dividing by the approach flow (unobstructed) shear stress. The normalized shear stresses were plotted as a function of the distance upstream of the pier. Their results show that at the immediate base of the pier, the shear can be amplified by as much as six times the approach flow shear; within two pier diameters upstream, the shear stress decays but is in the range of 1.5 - 4 times the

approach flow shear value. Past two pier diameters the shear gradually drops off to the approach flow shear value. These results suggest that Ahmed and Rajaratnam (1998) did not use average velocities as part of their analysis, but rather a group of velocities which corresponded to the highest gradient of measurements. Their results at the base of the pier (within two pier widths upstream) compare favorably with the peak and average shear intensity amplifications (1.5–4) found in this work (Section 8.5).

8.5.3.4 – Ali and Karim (2002)

Ali and Karim (2002) used the FLUENT CFD model in an attempt to study the flow field around a cylinder on both a flat bed and in a scour hole. A 45 x 28 non-uniform grid was mapped in the domain cross-section which had limits of three pier diameter widths upstream and six pier diameter widths downstream. Neither the depth of flow nor approach Froude number were given, but a mean velocity of 0.067m/s was used for simulation. The results of the flat bed simulation show an almost complete absence of shear stress at the base of the upstream side of the pier. A shear magnification (shear at pier / approach flow shear) ranging from 0.007 to 0.021 is shown on the bed within one pier diameter upstream of the pier. These results suggest the absence of any vortex upstream of the pier. A visual illustration of the flow field shows this to be true, as the area immediately upstream of the pier is dominated by a diving current only. Downstream visuals, however, show the shedding of several vortices. The lack of the vortex at the upstream side of the pier being simulated with the model,

which has been shown to exist in numerous studies, makes the results of this study unsuitable for comparison.

8.5.3.5 Jones (2002)

Jones (2002) performed experiments using PIV (Particle Image Velocimetry) in order to ascertain the flow field in front of a pier. Based on the flow field, he was able to determine the shear stress averaged over a period of time on the channel bed using Newton's law of viscosity (Equation 25) and the shear stress for several millimeters above the channel bed using a combination of laminar (Equation (25)) and turbulent stresses (Equation (26)).

$$\tau_{lam} = \mu \frac{du}{dy} \quad (25)$$

Where: τ_{lam} = Laminar shear stress (Pa)
 μ = Absolute viscosity (N s/m²)
 $\frac{du}{dy}$ = Gradient of velocity profile

$$\tau_{tur} = \rho \overline{u'v'} \quad (26)$$

Where: τ_{tur} = Turbulent shear stress (Pa)
 ρ = Density of water = 1000 (kg/m³)
 u' = Velocity fluctuation in x-direction (m/s)
 v' = Velocity fluctuation in y-direction (m/s)

From a time average analysis of his PIV recordings, Jones (2002) saw the presence of both a diving current and a vortex upstream of the pier. The shear stress calculated on the bed at the location of the diving current (at the

intersection of the pier and channel bed) was negligible, but under the vortex (location was within one pier diameter upstream) the shear stress was amplified by approximately six times the approach flow value.

While Jones' results do not incorporate the oscillatory motion of the vortex, they do present a shear stress which can be expected to be generated under a stationary vortex close to the channel bottom (0.3 mm). A stationary vortex is likely to yield the maximum shear value, when viewing the time-shear signature of an oscillatory vortex. Therefore, Jones' results are comparable to the peak shear amplification results of this study.

The experimental flow conditions were not presented in the paper but Jones (2002, p 148) states that there is "an inherent assumption that the ratio of shear stresses holds for a wide range of approach flow velocities." Therefore, his results cannot be compared to the results of this study at any particular Froude number, but only over the entire spectrum. Jones' results in general are approximately 50 to 100 percent higher than the peak shear amplification ratios calculated in this study. One possible reason for the lack of agreement is that Jones predicted the shear stress under the vortex by ascertaining the velocity profile through the vortex and then extrapolating the slope of the velocity curve from the lowest measured point (0.3 mm) to the channel bottom, from which he used Newton's law of viscosity to determine the shear stress. This method is only viable if the final few points on the velocity curve, which depict its slope, are within the laminar sublayer of the flow where the velocity change is assumed to be linear. While 0.3 mm is very close to the boundary, rough approximations of

the boundary layer height for the presumed flow conditions (based on personal observation of experimental setup - Froude number = 0.2) result in a boundary layer thickness of about 0.3 – 0.4 mm, meaning that the final few points used to determine the slope of the velocity profile may have been outside the laminar sublayer. Jones realized the potential errors associated with this type of prediction and cautioned that the manner in which the velocity profile was extracted to the channel bottom could have resulted in boundary shear amplification predictions ranging from less than 1 up to 95. A more detailed study using PIV, generating data closer to the boundary (say 0.1 mm) may produce results quantitatively similar to the ones found in this study. Finally, while Jones' (2002) results do not compare favorably to the ones found in this study, they are on the same order of magnitude and suggest that using PIV may be a viable option for shear stress determination under a stationary vortex.

8.6 Discussion of Results

Overall, the results of the previous analyses show the continuous presence of a vortex system upstream of an obstruction. The results from the frequency content analysis show the measurements to be quasi-periodic, which suggests that one vortex did not stay in front of the pier for the entire length of each measurement and that after a certain duration (dependent on Froude number) the vortex shed. A new vortex is suspected to have developed before the original one shed based on the fact that the approach flow shear stress was always exceeded, and the underlying assumption that only the vortex has the

ability to increase the shear stress upstream of a pier. The duration that each vortex stayed in front of the pier before eventually shedding downstream was found to range between 1 and 3 seconds, with a faster shedding frequency associated with higher Froude numbers, suggesting that at lower Froude numbers, a single vortex may dominate the flow field for relatively longer periods of time.

The results of the peak shear amplification analysis are rather contrary when comparing the adjusted shear values to the unadjusted shear values. Peak amplifications vary from 3.9 for the unadjusted analysis to 20.1 for the adjusted analysis. These differences in amplification can lead to drastically different conclusions when trying to ascertain if the vortex increasing shear has the potential to solely initiate scour. It is the authors' opinion that the unadjusted shear amplification results better represent a more accurate assessment of the shear amplification results. This is based on the fact that the mechanics of the flow field are quite different between the unobstructed and obstructed flow situations, and therefore does not seem legitimate to adjust the obstructed flow results to coincide with a theoretical prediction of an entirely different mechanism. Additionally, the unadjusted peak shear amplifications have a better agreement with shear amplifications measured by other investigators such as Ahmed and Rajaratnam (1998) and Jones (2002), suggesting the unadjusted values are more proper.

The question of whether the vortex increases shear enough to solely initiate scour is now addressed. Recall that several investigators witnessed the

initiation of scour at the base of a pier once the approach flow shear velocity reaches half of the critical velocity necessary for a particular sediment to transport. Based on this observation and Equation (10), the original hypothesis was formulated that the increase of shear stress at the base of a pier is at least four times the approach flow value, and that the increase is responsible for initiating scour. The peak shear amplification results show this condition is approached (and possibly exceeded based on the maximum uncertainty of the ratio) at the lower range of Froude numbers tested as part of this study, with peak shear amplifications being as high as 3.9 (+/- 0.9). Additionally, there is an increasing trend of peak shear amplification as the Froude number decreases, implying that if tests had been conducted at Froude numbers smaller than 0.13, the conditions of the hypothesis may have been met based on measurement alone (without uncertainty analysis). As it is, however, the hypothesis condition was not met and the peak shear amplification (disregarding uncertainty) never exceeded the 4 times amplification condition. Interestingly, the amplification value did not stay at a constant level (which has been assumed by various investigators), but instead dropped to as low as 2.5 (+/- 0.4) at the highest Froude numbers tested; the trend suggests that this value would have continued to diminish with increasing Froude number. An analysis of the flow field presented by Raudkivi (1986) and Ahmed and Rajaratnam (1998) can be used to give one possible explanation for the decreasing peak shear amplification with increasing Froude number.

Ahmed and Rajaratnam (1998) conducted experiments at a Froude number of approximately 0.2 and found that the diving current reflecting off the face of a pier reaches approximately 35 percent of the mean approach flow velocity. Raudkivi (1986) conducted experiments at Froude numbers in the range of 0.5 to 0.6 and found the diving current reached approximately 80 percent of the mean approach flow velocity. Comparison of these results shows that as the approach flow velocity (Froude number) increases, the diving current velocity also increases. An increase in diving current velocity is thought to have the potential to create larger disturbances in the flow field due to its greater impact on the channel bottom possibly making the formation and effectiveness of the vortex more difficult. This suggestion is corroborated by the work of Eckerle and Awad (1991), who showed that if the approach flow velocity (Pier Reynolds number) becomes too great that the vortex system will not form at all, but the diving current still will exist.

Therefore, analysis of these three studies as well as the results from this study suggest that the initiation of scour at the upstream face of a pier and the mechanism which causes it may be entirely dependent on approach flow conditions, where scour created in flows which are deep and slow moving (low Froude number) may be initiated and controlled by the shear stress under the vortex, and scour in flows which are shallow and fast (high Froude number) may be initiated by the diving current reflecting off the pier. A further more detailed study involving measurements of both the shear stress under the vortex and the diving current velocity, in a movable bed, is warranted before a definitive final

conclusion can be made about this shifting of controlling mechanism based on approach flow conditions. As for this study in regards to its purpose, the results indicate that scour is most likely not caused by an increase in shear stress alone.

CHAPTER 9

CONCLUSIONS

9.1 Unobstructed Flow/Shear Sensor

A shear measuring device has been designed and implemented which uses a series of four strain gages to measure the amount of tangential force occurring over a flat plate mounted flush to a channel bottom. The force, leading to a displacement of the measuring plate, is calibrated to yield an applied shear stress over the surface. This device was used to ascertain a relationship between a uniform flow Froude number and an applied shear stress. A total of 69 experiments were completed.

The results from the sensor were compared to two theoretical equations. Each of these equations stems from different assumptions and is independent in the derivation. The equations produced similar results to one another, but in general under-predicted the values measured from the shear sensor by an average of 0.2 Pa. The trends obtained from both equations and the measuring sensor were agreeable, implying that the sensor was in working order. Additionally, the sensor showed a rapid increase in shear once the depth of flow dropped below 1 inch. This increase was expected based on the work of Ettema (2000), who stated that once the depth flow falls beneath approximately 1 inch, additional forces due to surface tension (which normally are not present) can begin to dominate. Overall, the sensor is considered to be in working order and a viable device which can be used for boundary shear stress measurements.

9.2 Obstructed Flow

The results of this study show the constant presence of a vortex system at the base of a blunt nosed obstruction in a fluid flow. This is evidenced by a continuous increase in shear stress at the base of the obstruction, above the approach flow threshold. The vortex is shown to shed at a higher frequency with respect to increased Froude numbers (as indicated by the average duration of each clump and an assumption that each clump is equivalent to one vortex), but at no point in the shedding process is there a lack of increased shear stress at the base of the obstruction, implying that a new vortex is formed prior to the previous one shedding. The amount of shear amplification is on the order of 2.6 (+/- 0.4) – 3.9 (+/- 0.9) times the approach flow shear value. This amplification value at its higher end borders on the established criteria (greater than or equal to 4 times the approach flow shear value) for the possibility of scour being initiated solely by an increase in shear stress due to the vortex. As flow conditions changed, however, and the approach flow increased faster with respect to changes in depth, the amplification value diminished, suggesting increased shear stress may play less of a role in initiating scour at these flow conditions.

Based on experimental observations conducted by numerous other investigators, scour initiates once the shear velocity reaches approximately one-half the critical velocity for a particular sediment to transport. This observation in combination with Equation (10) implies that the shear stress at the base of an obstruction is amplified by 4 times the approach flow value. The measurements

conducted as part of this study, however, show this not to be the case. Therefore, it is concluded that scour is most likely not caused by increases in shear stress alone. The more likely scenario is that scour is caused by a combination of both a reduced pressure field around the particles caused by the generation of a diving current impacting the channel bed normally, and an increase in shear stress caused by the formation of a vortex system.

Based on the results of this work and conclusions mentioned previously, the question still remains: "Should the current scour equations be modified to include a shear stress parameter?" The simplest answer is YES, due to the fact that there are definite increases in shear stress; however, it may not be possible due to the following reason. As it is, in a non-uniform flow, shear stress predictions on a channel bottom are adequate at best. This is because shear stress is a function of multiple variables which are constantly changing from one section to the next in a natural environment due to irregularities along the channel bottom both laterally and in the flow direction. Therefore, the prediction of an accurate approach flow shear stress and a corresponding shear amplification value at the base of a pier is not obtained easily. Additionally, simply adding a shear stress variable to the current scour equations still does not account for the inherent presence of the diving current and its effect on initiating scour and its role in determining an ultimate scour depth.

Possibly a better solution would be to experimentally determine the overall relationship between approach flow conditions, the diving current reflecting off the pier, the increase in shear stress due to the vortex, and the associated effect

on a maximum depth of scour. Then, with this detailed knowledge of all four factors, methods for predicting scour depths could be developed, in lieu of just ascertaining a regression equation based on flow conditions and a scour depth, as is typically done. Until researchers gain a better understanding of each of the above-named mechanisms and their relationship to one another, scour predictions based on current methods will be adequate at best.

As a final note, it is interesting to observe the development of the wide pier phenomenon. Although this effect generally has been accepted to occur once the ratio of depth of flow to pier width falls below 0.8, this work has shown it to occur for ratios less than 0.6. More experimental work in this area is warranted to quantify an exact value at which this phenomenon occurs.

9.3 Engineering Significance / Recommendations

This work can prove to be very beneficial to the practicing engineering community. Much research has been completed and subsequent debates have arisen about the scouring process at the base of blunt-nosed piers. The results of this research show that the scouring process is a complex phenomenon which is driven by two components. With this knowledge, the results can be used to engineer new and better designs of piers, their foundations, and corresponding protective structures (flow arrestors, riprap, etc.). The new designs would have to incorporate devices which can be used to abolish the downflow component. Additionally, appropriate sized riprap or other shear protective measures would have to be implemented based on the results of the peak shear amplification

analysis. It is recommended that these protective measures be based on an increase in shear of at least four times the undisturbed value.

Finally, the results of this work can prove to be paramount in the current research being conducted on scour of cohesive soils at the base of piers. Most of the research is centered on finding an exact shear amplification factor as well as a time rate of scour factor. The overall findings of this research show a functional relationship of shear amplification vs. Froude number. Additionally, the results of each trial of this research deliver a relationship of shear vs. time at various Froude numbers. An analysis of the data from each trial can be very helpful in quantifying the frequency with which the shear exceeds a given threshold, and therefore help in the determination of an appropriate decay function depicting a time rate of scour for various soil types.

9.4 Future Work

While the completion of this work has provided valuable insight into the mechanism which leads to the initiation of scour, much more research could be completed in order to fully maximize the resourcefulness of the sensor. The following tasks are recommended:

- Experiments which include the simulation of various bed roughnesses should be completed both with and without the presence of the pier to determine what affect bed roughness has on the amplification of shear in front of an obstruction.

- Experiments should be completed using both different sized and different shaped piers in order to verify whether either of these two parameters has a significant impact on the results of this research.
- Experiments should be conducted which include mobile sediment to determine at which flow conditions and corresponding shear stress does scour actually initiate.
- Experiments should be conducted simultaneously using both the shear sensor to quantify shear values, and a visual method such as PIV, to quantify the flow field and associated magnitude of the diving current, in order to determine a relationship between these two mechanisms and the relative effect each has on initiating scour at various flow conditions.
- More experiments should be conducted at shallow depths to better quantify an exact depth of flow to pier width ratio which the vortex has trouble forming, leading to the generation of a wide pier situation.

REFERENCES

- Abed, L.M., 1991, "Local Scour around Bridge Piers in Pressure Flow," Dissertation, Civil Engineering Dept., Colorado State University, Fort Collins, CO.
- Abed, L., and Gasser, M., 1993, "Model Study of Local Scour Downstream Bridge Piers," ASCE Hydraulic Engineering, Proc. 1993 National Conference, 1738-1743.
- Ahmed, F., and Rajaratnam, N., 1998, "Flow Around Bridge Piers," Journal of Hydraulic Engineering, Vol. 124, No. 3, 288-300.
- Ali, K.H.M., and Karim, O.A., 2002, "Simulation of Flow Around Piers," Journal of Hydraulic Research, Vol. 40, No. 2, 161-174.
- Ali, K.H.M., and Lim, S.Y., 1986, "Local Scour Caused by Submerged Wall-Jets," Proceedings of the Institution of Civil Engineers, London, England, Vol. 81, No. 2, 607-645.
- Annandale, G.W., 1999, "Calculation of Pier Scour using the Erodibility Index Method," Draft notes for a short course presented to the Maryland State Highway Administration.
- Ansari, S.A., et al., 2002, "Influence of Cohesion on Scour Around Bridge Piers," Journal of Hydraulic Research, Vol. 40, No. 6, 717-729.
- Baker, C.J., 1980, "Theoretical Approach to Prediction of Local Scour Around Bridge Piers," Journal of Hydraulic Research, Vol. 18, No. 1, 1-12.
- Breusars, et al., 1977, "Local Scour Around Cylindrical Piers," Journal of Hydraulic Research, Vol. 15, No. 3, 211-252.
- Briaud, J.L., et al., 1999, "SRICOS: Prediction of Scour Rate in Cohesive Soils at Bridge Piers," Journal of Geotechnical and Geoenvironmental Engineering, Vol. 125, 237-246.
- Brice, J.C., and Blodgett, J.C., 1978, "Countermeasures for Hydraulic Problems at Bridges," Vol. 1 and 2, FHWA/RD-78-162&163, Federal Highway Administration, U.S. Department of Transportation, Washington D.C.
- Carstens, M.R., 1966, "Similarity Laws for Localized Scour," Journal of Hydraulic Engineering, Vol. 92, No. 3, 13-36.
- Chabert, J., and Engeldinger, P., 1956, Etude des Affonillements Author des Piles des Ponts, Laboratoire National d'Hydraulique, Chatoe, France.

Chaudhry, M.H., 1993, "Open-Channel Flow," Published by Prentice-Hall, Inc., 263.

Dargahi, B., 1987, "Flow Field and Local Scouring Around a Cylinder," Bulletin No. 37, R. Inst. Tech. Hydr. Lab, Stockholm, Sweden.

Dargahi, B., 1989, "The Turbulent Flow Field Around a Circular Cylinder," Experiments in Fluids, Vol. 8, 1-12.

Dargahi, B., 1990, "Controlling Mechanism of Local Scouring," Journal of Hydraulic Engineering, Vol. 116, No. 10, 1197-1214.

Davis, S.R., 1984, "Case Histories of Scour Problems at Bridges," Transportation Research Record 950, Second Bridge Engineering Conference, Vol. 2, Transportation Research Board, Washington D.C.

Dey, S., et al., 1995, "Clear Water Scour at Circular Piers," Journal of Hydraulic Engineering, Vol. 121, No. 12, 869-876.

Dou, X., 1997, "Numerical Simulation of Three-Dimensional Flow Field and Local Scour at Bridge Crossings," Dissertation, Computational Hydroscience Engineering, University of Mississippi, University, MS.

Eckerle, W.A., and Awad, J.K., 1991, "Effect of Freestream Velocity on the Three-Dimensional Separated Flow Region in Front of a Cylinder," Journal of Fluid Engineering, Vol. 113, 37-44.

Edge, B.L., et al., 1998, "Determination of Velocity in Estuary for Bridge Scour Computations," Journal of Hydraulic Engineering, Vol. 124, No. 6, 619-628.

Ermshaus, R., 1985, "Hot Film Anemometry," Institute of Hydromechanics, University of Karlsruhe, Germany, Seminar Notes (October 4-6).

Ettema, R., 1980, "Scour at Bridge Piers," Rep. No. 216, School of Engineering, University of Auckland, New Zealand.

Ettema, R., 2000, "Hydraulic Modeling – Concepts and Practice," ASCE Manuals and Reports on Engineering Practice No. 97, Published by American Society of Civil Engineers, Reston, VA, 41, 63

Ettema, R., et al., 1998, "Scale Effect in Pier-Scour Experiments," Journal of Hydraulic Engineering, Vol. 124, No. 6, 639-642.

Froehlich, D.C., 1988, "Analysis of On-site Measurements of Scour at Piers," Proceedings of the 1988 National Conference on Hydraulic Engineering, Colorado Springs, Colorado, August 15-19, 1988, American Society of Civil Engineers, New York, NY, 826-831.

Froehlich, D.C., 1996, "Bridge Hydraulic and Scour Analysis using FESWMS-2DH," ASCE, North American Water and Environmental Congress, Washington D.C.

Gradowcyzk, M.H., 1968, "Localized Scour in Erodible Bed Channels," Journal of Hydraulic Research, Vol. 6, No. 4, 289-334.

Graf, W.H., and Istiarto, I., 2002, "Flow Pattern in the Scour Hole around a Cylinder," Journal of Hydraulic Research, Vol. 40, No. 1, 13-20.

Grecco, J.J., 1990 "The Flow Structure in the Vicinity of a Cylinder-Flat Plate Junction: Flow Regimes, Periodicity, and Vortex Interactions," Masters Thesis, Department of Civil Engineering, Lehigh University, Bethlehem, PA.

Hancu, S., 1971, "Sur le Calcul des Affouillements Locaux Dams la Zone des Piles de Ponts," Proc. 14th IAHR Cong., Vol. 3, 299-313.

Holman, J.P., 1989, "Experimental Methods for Engineers", 5th edition, Published by McGraw-Hill, Inc., p. 42

Jain, S.C., 1981, "Maximum Clear-Water Scour Around Circular Piers," Journal of Hydraulic Engineering, Vol. 107, No. 5, 611-626.

Jain, S.C., and Fischer, E.E., 1980, "Scour Around Bridge Piers at High Flow Velocities," Journal of Hydraulic Engineering, Vol. 106, No. 11, 1827-1841.

Johnson, P.A., 1992, "Reliability-Based Pier Scour Engineering," Journal of Hydraulic Engineering, Vol. 118, No. 10, 1344-1357.

Johnson, P.A., 1995, "Comparison of Pier-Scour Equations using Field Data," Journal of Hydraulic Engineering, Vol. 121, No. 8, 626-629.

Johnson, P.A., 1999, "Scour at Wide Piers Relative to Flow Depth," Compendium of ASCE Conference Papers Edited by E.V. Richardson and P.F. Lagasse, 280-287

Johnson, P.A., and Ayyub, B.M., 1992, "Assessing Time-Variant Bridge Reliability Due to Pier Scour," Journal of Hydraulic Engineering, Vol. 118, No. 6, 887-903.

- Johnson, P.A., and Jones, S., 1992, "Shear Stress at Base of Bridge Pier," Transportation Research Record No. 1350, Transportation Research Board, 14-18.
- Johnson, P.A., and Jones, S., 1993, "Merging Laboratory and Field Data in Bridge Scour," Journal of Hydraulic Engineering, Vol. 119, No. 10, 1176-1181.
- Jones, S., 1993, "Preliminary Studies on Pressure Flow Scour," ASCE Hydraulic Engineering, Proc. 1993 National Conference, 916-921.
- Jones, S., 2002, "Indirect Methods of Measuring Shear Stress in the Bottom of a Scour Hole," First International Conference on Scour of Foundations, Conference Proceedings, 140-155.
- Kandasamy, J.K., and Melville, B.W., 1998, "Maximum Local Scour Depth at Bridge Piers and Abutments," Journal of Hydraulic Research, Vol. 36, No. 2, 183-198.
- Karim, O.A., and Ali, K.H.M., 2000, "Prediction of Flow Patterns in Local Scour Holes Caused by Turbulent Water Jets," Journal of Hydraulic Research, Vol. 38, No. 4, 279-288.
- Kirkgoz, M.S., and Ardichoglu, M., 1997, "Velocity Profiles of Developing and Developed Open Channel Flow," Journal of Hydraulic Engineering, Vol. 123, No. 12, 1099-1105.
- Kothyari, U.C., et al., 1992, "Temporal Variation of Scour Around Circular Bridge Piers," Journal of Hydraulic Engineering, Vol. 118, No. 8, 1091-1106.
- Kothyari, U.C., et al., 1993, "Live Bed Scour Around Cylindrical Bridge Piers," Journal of Hydraulic Research, Vol. 30, No. 5, 701-715.
- Kundu, P.K., 1990, "Fluid Mechanics," Oceanographic Center, Nova University, Dania, FL, Academic Press, Inc., 452.
- Larras, J., 1963, "Profondeurs Maximales d'Erosion Des Fonds Mobiles Autour Des Piles En Rivere," Ann. Ponts et Chaussees, Vol. 133, No. 4, 411-424.
- Laursen, E.M., 1960, "Scour at Bridge Crossings," Journal of Hydraulic Engineering, Vol. 86, No. 2, 39-54.
- Laursen, E.M., 1963, "An Analysis of Relief Bridge Scour," Journal of Hydraulic Engineering, Vol. 89, No. 3, 93-118.

- Laursen, E.M., and Toch, A., 1956, "Scour Around Bridge Piers and Abutments," Bulletin No. 4, Iowa Highway Research Board, Ames, IA.
- Lemmin, U., and Rolland, T., 1997, "Acoustic Velocity Profiler for Laboratory and Field Studies," Journal of Hydraulic Engineering, Vol. 123, No. 12, 1089-1098.
- Li, Y., et al., 2002, "Shear Stress Approach to Pier Scour Predictions," First International Conference on Scour of Foundations, Conference Proceedings, 140-155.
- Maull, D.J., and Young, R.A., 1973, "Vortex Shedding from Bluff Bodies in a Shear Flow," Journal of Fluid Mechanics, Vol. 60, Part 2, 401-409.
- Melville, B.W., 1975, "Local Scour at Bridge Sites," Report No. 117, University of Auckland, Auckland, New Zealand.
- Melville, B.W., and Raudkivi, A.J., 1977, "Flow Characteristics in Local Scour at Bridge Piers," Journal of Hydraulic Research, Vol. 15, No. 4, 373-380.
- Melville, B.W., and Sutherland, A.J., 1988, "Design Method for Local Scour at Bridge Piers," Journal of Hydraulic Engineering, Vol. 114, No. 10, 1210-1226.
- Mendoza-Cabralles, C., 1993, "Computation of Flow Past a Cylinder Mounted on a Flat Plate," ASCE Hydraulic Engineering, Proc. 1993 National Conference, 899-904.
- Muller, G., et al., 2001, "Mapping of Bridge Pier Scour with Projection Moire," Journal of Hydraulic Research, Vol. 39, No. 5, 1-7.
- National Transportation Safety Board, Highway Accident Report, 1987, "Collapse of New York Thruway (I-90) Bridge, Schoharie Creek, Near Amsterdam, New York, April 5, 1987."
- Naudascher, E., and Rockwell, D., 1994, "Flow-Induced Vibrations – An Engineering Guide – Hydraulic Structures Design Manual," Published by: A.A. Balkema, Rotterdam, Netherlands, 101-104.
- Neill, C.R., 1964, "River Bed Scour, A Review for Bridge Engineers," Contract No. 281, Res. Council of Alberta, Calgary, Alberta, Canada.
- Nurtjahyo, P., et al., 2002, "Bed Shear Stress around Rectangular Pier: Numerical Approach," First International Conference on Scour of Foundations, Conference Proceedings, 242-256.

- Olsen, N., and Melaaen, M., 1993, "Three-Dimensional Calculation of Scour Around Cylinders," *Journal of Hydraulic Engineering*, Vol. 119, No. 9, 1048-1053.
- Pagan, J., 1991, "Stability of Riprap for Protection at the Toe of Abutments," Publication No. FHWA-RD-91-057, Federal Highway Administration, Office of Research and Development.
- Palisade Corporation, 2002, "Best Fit," Probability Distribution Fitting Commercial Software Package, Version 4.5.2.
- Parola, A.C., 1991, "The Stability of Riprap used to Protect Bridge Piers," Publication No. FHWA-RD-91-063, Federal Highway Administration, Office of Research and Development, Mclean, VA.
- Parola et al., 1996, "Effects of Rectangular Foundation Geometry on Local Pier Scour," *Journal of Hydraulic Engineering*, Vol. 122, No. 1, 35-40.
- Ports, M., et al., 1993, "Practical Comparison of One-Dimensional and Two-Dimensional Hydraulic Analyses for Bridge Scour," *ASCE Hydraulic Engineering*, Proc. 1993 National Conference, 1732-1737.
- Prechtl, H., 2002, "Shear Stress Sensor System – Design and Operation Manual," Austria.
- Raffel, M., Willert, C., and Kompenhans, J., 1998, "Particle Image Velocimetry – A Practical Guide," 1st edition, Springer Publishing, Berlin, Germany.
- Rajaratnam, N.M., 1980, "Erosion by Circular Wall Jets in Cross Flow," *Journal of Hydraulic Engineering*, Vol. 106, No. 11, 1867-1883.
- Raudkivi, A.J., 1986, "Functional Trends of Scour at Bridge Piers," *Journal of Hydraulic Engineering*, Vol. 112, No. 6, 1-13.
- Raudkivi, A.J., and Ettema, R., 1983, "Clear-Water Scour at Cylindrical Piers," *Journal of Hydraulic Engineering*, Vol. 109, No. 3, 338-350.
- Raudkivi, A.J., and Ettema, R., 1985, "Scour at Cylindrical Bridge Piers in Armored Beds," *Journal of Hydraulic Engineering*, Vol. 111, No. 4, 713-731.
- Richardson, E.V., and Abed, L., 1993, "Top Width of Pier Scour Holes in Free and Pressure Flow," *ASCE Hydraulic Engineering*, Proc. 1993 National Conference, 911-915

- Richardson, E.V., Harrison, L.J., and Davis, S.R., 1995, "Evaluating Scour at Bridges," HEC-18, Report FHWA-IP-90-017, Washington D.C.
- Richardson, J.E., and Panchang, V.G., 1998, "Three-Dimensional Simulation of Scour-Inducing Flow at Bridge Piers," Journal of Hydraulic Engineering, Vol. 124, No. 5, 530-540.
- Roshko, A., 1961, "Experiments on the Flow Past a Circular Cylinder at Very High Reynolds Numbers," Journal of Fluid Mechanics, Vol. 10, 345-356.
- Schwind, R.G., 1962, "The Three-Dimensional Boundary Layer Near a Strut," Gas Turbine Laboratory Report No. 67, Massachusetts Institute of Technology, Boston, MA.
- Shen, H.W., et al., 1966a, "Mechanics of Local Scour," Reference No. CER66HWS-22, In-house Publication – Colorado State University, Fort Collins, CO.
- Shen, H.W., et al., 1966b, "Mechanics of Local Scour – Supplement," Reference No. CER66HWS-36, In-house Publication – Colorado State University, Fort Collins, CO.
- Shen, H.W., et al., 1969, "Local Scour Around Bridge Piers," Journal of Hydraulic Engineering, Vol. 95, No. 6, 1919-1940.
- Shields, A., 1936, "Application of Similarity Principles and Turbulence Research to Bed-Load Movement," California Institute of Technology, Pasadena, CA.
- Smart, G.M., 1999, "Turbulent Velocity Profiles and Boundary Shear in Gravel Bed Rivers," Journal of Hydraulic Engineering, Vol. 125, No. 2, 106-116.
- Stevens, M.A., et al., 1991, "Wake Vortex Scour at Bridge Piers," Journal of Hydraulic Engineering, Vol. 117, No. 7, 891-904.
- Varadan, V.V., et al., 1990, "Measurement of Skin Friction Associated with Turbulent Flows in Air and Water using SAW Devices," IEEE Ultrasonics Symposium, Proc. 1990 National Conference, 303-306.
- Vautier, E.W., 1972, "Flow Around a Cylindrical Pier with Scour Hole Formation," M.E. Thesis, Civil Engineering Dept., Univ. of Auckland, New Zealand.
- Wen,F. M., et al., 1993, "The Separated Flow Around a Circular Bridge Pier," ASCE Hydraulic Engineering, Proc. 1993 National Conference, 905-910.

- Wu, S., and Rajaratnam, N., 1995, "Free Jumps, Submerged Jumps and Wall Jets," *Journal of Hydraulic Research*, Vol. 33, No. 2, 197-212.
- Wu, S., and Rajaratnam, N., 2000, "A Simple Method for Measuring Shear Stress on Rough Boundaries," *Journal of Hydraulic Research*, Vol. 38, No. 5, 399-400.
- Yanmaz, A.M., and Altinbilek, H.D., 1991, "Study of Time Dependent Local Scour Around Bridge Piers," *Journal of Hydraulic Engineering*, Vol. 117, No. 10, 1247-1267.
- Yarnell, D.L., and Nagler, F.A., 1931, "A Report Upon a Hydraulic Investigation of North Carolina Standard Reinforced Concrete Bridge Pier Number P-401-R and Modifications Thereof," Iowa Institute of Hydraulic Research, University of Iowa, Iowa City, IA.
- Zaghoul, N.A., and McCorquodale, J.A., 1975, "A Stable Numerical Model for Local Scour," *Journal of Hydraulic Research*, Vol. 13, No. 4, 425-444.

APPENDIX A

UNOBSTRUCTED FLOW SUMMARY TABLES

Trial Name	Q (lps)	Depth (cm)	Velocity (cm/s)	Froude #	Shear avg (Pa)	Shear St. Dev. (Pa)	Shear var
40_1H	2.0	5.2	8.6	0.12	0.23	0.02	0.00
40_2H	2.0	5.2	8.6	0.12	0.22	0.02	0.00
40_3H	2.0	5.2	8.6	0.12	0.22	0.02	0.00
40_1L	2.2	2.0	24.8	0.56	0.57	0.07	0.00
40_2L	2.2	2.0	24.6	0.56	0.51	0.06	0.00
40_3L	2.2	2.0	24.7	0.56	0.53	0.06	0.00
45_1L	2.6	2.2	25.9	0.56	0.52	0.05	0.00
45_2L	2.6	2.2	25.9	0.56	0.53	0.04	0.00
45_3L	2.6	2.2	26.0	0.56	0.53	0.04	0.00
50_1H	2.8	5.6	11.0	0.15	0.24	0.02	0.00
50_2H	2.8	5.6	11.0	0.15	0.24	0.02	0.00
50_3H	2.8	5.6	11.0	0.15	0.24	0.02	0.00
50_2L	2.9	2.4	26.3	0.54	0.47	0.05	0.00
50_4L	2.9	2.5	26.0	0.53	0.38	0.11	0.01
50_5L	2.9	2.5	25.7	0.52	0.46	0.09	0.01
50_6L	2.9	2.5	26.1	0.53	0.38	0.11	0.01
55_1L	3.3	2.8	25.1	0.48	0.35	0.05	0.00
55_2L	3.3	2.8	25.4	0.48	0.32	0.05	0.00
55_3L	3.2	2.9	24.8	0.47	0.32	0.05	0.00
55_6L	3.2	2.8	25.3	0.48	0.38	0.08	0.01
60_1H	3.5	6.0	12.8	0.17	0.26	0.03	0.00
60_2H	3.5	5.9	12.9	0.17	0.26	0.02	0.00
60_4H	3.5	5.9	12.8	0.17	0.26	0.02	0.00
60_5H	3.5	6.0	12.9	0.17	0.26	0.03	0.00
60_1L	3.6	3.1	25.0	0.45	0.33	0.04	0.00
60_2L	3.6	3.1	24.8	0.45	0.33	0.05	0.00
60_3L	3.6	3.2	24.3	0.43	0.33	0.04	0.00
60_4L	3.5	3.2	24.2	0.43	0.32	0.04	0.00
65_1L	3.9	3.4	25.1	0.44	0.39	0.08	0.01
65_2L	3.8	3.4	24.7	0.43	0.37	0.08	0.01
65_3L	3.8	3.4	24.7	0.43	0.37	0.08	0.01
67_1L	4.0	4.0	21.9	0.35	0.35	0.02	0.00
67_2L	4.0	3.8	23.0	0.38	0.36	0.02	0.00
67_3L	4.0	3.8	22.9	0.37	0.36	0.02	0.00
70_1H	4.1	6.3	14.2	0.18	0.28	0.02	0.00
70_2H	4.1	6.3	14.3	0.18	0.28	0.02	0.00
70_3H	4.1	6.3	14.1	0.18	0.28	0.02	0.00
70_4H	4.1	6.3	14.1	0.18	0.28	0.04	0.00
70_1L	4.1	3.2	28.6	0.51	0.36	0.08	0.01
70_2L	4.2	3.2	28.7	0.51	0.38	0.10	0.01

Trial Name	Q (lps)	Depth (cm)	Velocity (cm/s)	Froude #	Shear avg (Pa)	Shear St. Dev. (Pa)	Shear var
70_3L	4.1	3.4	26.6	0.46	0.39	0.08	0.01
75_4L	4.4	3.4	28.7	0.50	0.36	0.07	0.00
75_5L	4.4	3.4	28.7	0.50	0.37	0.07	0.00
75_6L	4.4	3.4	28.9	0.50	0.34	0.07	0.01
75_7L	4.4	3.4	29.0	0.51	0.35	0.07	0.00
80_1H	4.7	6.6	15.7	0.19	0.28	0.02	0.00
80_2H	4.7	6.6	15.7	0.19	0.28	0.03	0.00
80_8H	4.7	6.6	15.6	0.19	0.28	0.02	0.00
80_9H	4.7	6.6	15.5	0.19	0.29	0.03	0.00
80_10H	4.7	6.8	15.2	0.19	0.27	0.03	0.00
80_11H	4.7	6.6	15.5	0.19	0.27	0.02	0.00
80_1L	4.7	3.9	26.7	0.43	0.35	0.04	0.00
80_2L	4.7	3.9	26.7	0.43	0.36	0.04	0.00
80_3L	4.7	3.9	26.7	0.43	0.35	0.04	0.00
85_1L	5.0	5.0	21.8	0.31	0.32	0.03	0.00
85_2L	5.0	5.8	19.0	0.25	0.31	0.03	0.00
85_3L	5.0	5.0	22.1	0.32	0.32	0.04	0.00
90_1H	5.3	7.3	15.9	0.19	0.29	0.03	0.00
90_2H	5.3	7.3	15.8	0.19	0.29	0.02	0.00
90_3H	5.3	7.3	15.8	0.19	0.29	0.03	0.00
90_1L	5.3	5.9	19.7	0.26	0.32	0.04	0.00
90_2L	5.3	5.9	19.6	0.26	0.30	0.04	0.00
90_3L	5.3	6.0	19.2	0.25	0.31	0.04	0.00
94_1H	5.5	7.5	16.0	0.19	0.30	0.03	0.00
94_2H	5.5	7.6	15.9	0.18	0.29	0.03	0.00
94_3H	5.5	7.5	16.0	0.19	0.29	0.03	0.00
94_1L	5.5	6.8	17.8	0.22	0.31	0.04	0.00
94_2L	5.5	6.5	18.6	0.23	0.31	0.04	0.00
94_3L	5.5	6.3	19.1	0.24	0.33	0.04	0.00

Trial Name	friction slope	Shear (control vol.) (Pa)	Shear (theory - log law) (Pa)	shear velocity (cm/s)
40_1H	5E-05	0.02	0.03	0.5
40_2H	5E-05	0.02	0.03	0.5
40_3H	5E-05	0.02	0.03	0.5
40_1L	1E-03	0.23	0.23	1.5
40_2L	1E-03	0.22	0.23	1.5
40_3L	1E-03	0.23	0.23	1.5
45_1L	1E-03	0.24	0.24	1.5
45_2L	1E-03	0.24	0.24	1.5
45_3L	1E-03	0.24	0.24	1.6
50_1H	7E-05	0.03	0.04	0.6
50_2H	8E-05	0.03	0.04	0.7
50_3H	8E-05	0.03	0.04	0.6
50_2L	1E-03	0.24	0.24	1.6
50_4L	1E-03	0.23	0.24	1.5
50_5L	1E-03	0.23	0.23	1.5
50_6L	1E-03	0.24	0.23	1.5
55_1L	8E-04	0.21	0.21	1.5
55_2L	9E-04	0.21	0.22	1.5
55_3L	8E-04	0.20	0.21	1.4
55_6L	9E-04	0.21	0.22	1.5
60_1H	1E-04	0.04	0.05	0.7
60_2H	1E-04	0.05	0.06	0.7
60_4H	9E-05	0.04	0.05	0.7
60_5H	1E-04	0.04	0.05	0.7
60_1L	8E-04	0.20	0.21	1.4
60_2L	7E-04	0.20	0.20	1.4
60_3L	7E-04	0.19	0.20	1.4
60_4L	7E-04	0.19	0.19	1.4
65_1L	7E-04	0.20	0.21	1.4
65_2L	7E-04	0.19	0.20	1.4
65_3L	7E-04	0.19	0.20	1.4
67_1L	4E-04	0.15	0.16	1.3
67_2L	5E-04	0.16	0.17	1.3
67_3L	5E-04	0.16	0.17	1.3
70_1H	1E-04	0.05	0.06	0.8
70_2H	1E-04	0.05	0.07	0.8
70_3H	1E-04	0.05	0.06	0.8
70_4H	1E-04	0.05	0.06	0.8
70_1L	1E-03	0.26	0.26	1.6
70_2L	1E-03	0.26	0.26	1.6
70_3L	8E-04	0.22	0.23	1.5

Trial Name	friction slope	Shear (control vol.) (Pa)	Shear (theory - log law) (Pa)	shear velocity (cm/s)
75_4L	9E-04	0.26	0.26	1.6
75_5L	9E-04	0.26	0.26	1.6
75_6L	9E-04	0.27	0.26	1.6
75_7L	9E-04	0.27	0.26	1.6
80_1H	1E-04	0.06	0.08	0.9
80_2H	1E-04	0.06	0.08	0.9
80_8H	1E-04	0.06	0.07	0.9
80_9H	1E-04	0.06	0.07	0.9
80_10H	1E-04	0.06	0.07	0.8
80_11H	1E-04	0.06	0.07	0.9
80_1L	7E-04	0.22	0.22	1.5
80_2L	7E-04	0.22	0.22	1.5
80_3L	7E-04	0.22	0.22	1.5
85_1L	3E-04	0.13	0.15	1.2
85_2L	2E-04	0.10	0.11	1.0
85_3L	3E-04	0.14	0.15	1.2
90_1H	1E-04	0.06	0.08	0.9
90_2H	1E-04	0.06	0.08	0.9
90_3H	1E-04	0.06	0.08	0.9
90_1L	2E-04	0.10	0.12	1.1
90_2L	2E-04	0.10	0.12	1.1
90_3L	2E-04	0.10	0.11	1.1
94_1H	1E-04	0.06	0.08	0.9
94_2H	1E-04	0.06	0.08	0.9
94_3H	1E-04	0.06	0.08	0.9
94_1L	2E-04	0.08	0.09	1.0
94_2L	2E-04	0.09	0.10	1.0
94_3L	2E-04	0.10	0.11	1.0

APPENDIX B

OBSTRUCTED FLOW SUMMARY TABLES

Trial Name	Q (lps)	Depth (cm)	Velocity (cm/s)	Froude #	Length Ratio (y/b)	Shear avg (Pa)	Shear St. Dev (Pa)	Shear var
55_1L	2.3	0.1	0.7	0.40	0.34	0.14	0.17	0.03
55_2L	2.4	0.1	0.7	0.41	0.34	0.13	0.16	0.03
55_3L	2.4	0.1	0.7	0.41	0.34	0.14	0.15	0.02
55_4L	2.4	0.1	0.7	0.41	0.34	0.14	0.16	0.03
55_6L	2.3	0.1	0.7	0.40	0.34	0.14	0.17	0.03
60_1L	2.9	0.1	0.7	0.44	0.37	0.21	0.15	0.02
60_2L	2.9	0.1	0.7	0.44	0.37	0.19	0.16	0.03
60_3L	2.9	0.1	0.7	0.44	0.37	0.20	0.15	0.02
60_4L	2.9	0.1	0.7	0.44	0.37	0.20	0.15	0.02
60_4H	2.8	0.2	0.3	0.14	0.80	0.64	0.03	0.00
60_5H	2.8	0.2	0.3	0.14	0.80	0.64	0.02	0.00
60_6H	2.9	0.2	0.3	0.14	0.80	0.64	0.03	0.00
60_7H	2.8	0.2	0.3	0.14	0.80	0.64	0.03	0.00
60_8H	2.9	0.2	0.3	0.14	0.80	0.64	0.03	0.00
65_1L	3.2	0.1	0.8	0.44	0.40	0.26	0.17	0.03
65_2L	3.2	0.1	0.8	0.44	0.40	0.27	0.17	0.03
65_3L	3.2	0.1	0.8	0.45	0.39	0.25	0.18	0.03
65_4L	3.3	0.1	0.8	0.44	0.40	0.26	0.18	0.03
70_1L	3.6	0.1	0.8	0.43	0.43	0.32	0.19	0.04
70_2L	3.6	0.1	0.8	0.43	0.43	0.32	0.17	0.03
70_3L	3.6	0.1	0.8	0.41	0.45	0.33	0.16	0.03
70_4L	3.6	0.1	0.8	0.43	0.43	0.32	0.17	0.03
70_5L	3.6	0.1	0.8	0.42	0.44	0.32	0.17	0.03
70_4H	3.6	0.2	0.4	0.16	0.84	0.71	0.03	0.00
70_5H	3.6	0.2	0.4	0.16	0.84	0.71	0.03	0.00
70_6H	3.6	0.2	0.4	0.16	0.84	0.71	0.03	0.00
70_7H	3.6	0.2	0.4	0.16	0.84	0.71	0.03	0.00
70_8H	3.6	0.2	0.4	0.16	0.84	0.71	0.03	0.00
75_1L	3.9	0.1	0.8	0.44	0.46	0.37	0.19	0.04
75_2L	3.9	0.1	0.8	0.43	0.46	0.36	0.17	0.03
75_3L	3.9	0.1	0.8	0.43	0.46	0.37	0.16	0.03
75_4L	3.9	0.1	0.8	0.43	0.46	0.37	0.17	0.03
80_1L	4.3	0.1	0.8	0.40	0.51	0.47	0.12	0.01
80_2L	4.3	0.1	0.8	0.40	0.51	0.44	0.18	0.03
80_3L	4.3	0.1	0.8	0.41	0.50	0.42	0.18	0.03
80_4L	4.3	0.1	0.8	0.40	0.51	0.43	0.19	0.04
80_5L	4.3	0.1	0.8	0.41	0.50	0.44	0.18	0.03
80_4H	4.3	0.2	0.5	0.17	0.89	0.80	0.04	0.00
80_5H	4.3	0.2	0.5	0.17	0.89	0.79	0.04	0.00
80_6H	4.3	0.2	0.5	0.17	0.89	0.80	0.04	0.00
80_7H	4.3	0.2	0.5	0.17	0.89	0.80	0.04	0.00

Trial Name	Q (lps)	Depth (cm)	Velocity (cm/s)	Froude #	Length Ratio (y/b)	Shear avg (Pa)	Shear St. Dev (Pa)	Shear var
85_1L	4.6	0.2	0.7	0.31	0.63	0.55	0.09	0.01
85_2L	4.6	0.2	0.7	0.31	0.63	0.54	0.08	0.01
85_3L	4.6	0.2	0.7	0.32	0.62	0.54	0.09	0.01
85_4L	4.6	0.2	0.7	0.31	0.63	0.54	0.09	0.01
85_5L	4.6	0.2	0.7	0.32	0.62	0.54	0.09	0.01
90_1L	4.9	0.2	0.6	0.26	0.75	0.69	0.07	0.00
90_2L	4.9	0.2	0.5	0.21	0.87	0.80	0.06	0.00
90_3L	4.9	0.2	0.7	0.29	0.70	0.62	0.08	0.01
90_4L	4.9	0.2	0.6	0.24	0.78	0.72	0.07	0.00
90_5L	4.9	0.2	0.7	0.28	0.72	0.63	0.06	0.00
90_6L	4.9	0.2	0.6	0.25	0.77	0.70	0.07	0.00
94_1L	5.2	0.2	0.6	0.21	0.88	0.81	0.05	0.00
94_2L	5.2	0.2	0.6	0.25	0.80	0.71	0.07	0.01
94_3L	5.2	0.2	0.6	0.22	0.87	0.83	0.06	0.00
94_4L	5.2	0.2	0.6	0.21	0.89	0.84	0.05	0.00
94_5L	5.1	0.2	0.5	0.21	0.90	0.85	0.07	0.00
94_4H	5.1	0.2	0.5	0.17	1.01	0.97	0.03	0.00
94_5H	5.1	0.2	0.5	0.17	1.01	0.96	0.03	0.00
94_6H	5.1	0.2	0.5	0.17	1.01	0.96	0.03	0.00
94_7H	5.1	0.2	0.5	0.17	1.01	0.97	0.03	0.00

Trial Name	Threshold (Pa)	Omega	Frequency Content	Max Shear (Pa)	Average Shear Intensity (Pa)	Peak Shear Amplification	Avgerrage Shear Intensity Amp
55_1L	0.35	13.60	0.54	0.91	0.45	2.6	1.3
55_2L	0.35	14.28	0.50	0.79	0.46	2.2	1.3
55_3L	0.35	13.82	0.53	0.65	0.44	1.8	1.2
55_4L	0.35	13.82	0.52	0.77	0.45	2.2	1.3
55_6L	0.35	13.65	0.54	0.80	0.46	2.3	1.3
60_1L	0.36	13.82	0.54	0.94	0.44	2.6	1.2
60_2L	0.36	13.65	0.54	0.81	0.46	2.3	1.3
60_3L	0.36	13.97	0.53	0.90	0.46	2.5	1.3
60_4L	0.36	13.70	0.53	0.85	0.45	2.4	1.3
60_4H	0.24	17.31	0.22	0.91	0.88	3.8	3.7
60_5H	0.24	17.40	0.21	0.91	0.88	3.9	3.7
60_6H	0.24	17.35	0.22	0.91	0.88	3.8	3.7
60_7H	0.24	17.36	0.22	0.92	0.88	3.9	3.7
60_8H	0.24	17.31	0.22	0.90	0.88	3.8	3.7
65_1L	0.36	13.79	0.53	0.97	0.48	2.7	1.4
65_2L	0.36	14.00	0.53	0.97	0.49	2.7	1.4
65_3L	0.36	13.22	0.56	0.91	0.49	2.6	1.4
65_4L	0.36	13.65	0.54	0.93	0.49	2.6	1.4
70_1L	0.35	13.33	0.57	0.99	0.52	2.8	1.5
70_2L	0.35	13.81	0.53	0.96	0.50	2.7	1.4
70_3L	0.35	13.38	0.57	1.06	0.49	3.0	1.4
70_4L	0.35	14.09	0.53	0.96	0.49	2.7	1.4
70_5L	0.35	13.89	0.55	0.98	0.50	2.8	1.4
70_4H	0.26	17.19	0.24	0.83	0.89	3.2	3.5
70_5H	0.26	17.27	0.23	0.83	0.89	3.2	3.5
70_6H	0.26	17.21	0.24	0.84	0.89	3.2	3.5
70_7H	0.26	17.22	0.24	0.84	0.89	3.2	3.5
70_8H	0.26	17.20	0.24	0.83	0.89	3.2	3.5
75_1L	0.36	12.68	0.60	0.96	0.53	2.7	1.5
75_2L	0.35	13.69	0.55	1.20	0.52	3.4	1.5
75_3L	0.35	13.51	0.55	0.92	0.50	2.6	1.4
75_4L	0.35	13.47	0.55	0.96	0.52	2.7	1.5
80_1L	0.35	14.84	0.47	0.97	0.51	2.8	1.4
80_2L	0.35	13.45	0.56	1.12	0.55	3.2	1.6
80_3L	0.35	13.49	0.56	1.10	0.55	3.1	1.6
80_4L	0.35	13.29	0.57	1.19	0.55	3.4	1.6
80_5L	0.35	13.49	0.56	1.12	0.55	3.2	1.6
80_4H	0.27	16.92	0.28	0.93	0.80	3.4	3.0
80_5H	0.27	17.07	0.26	0.95	0.80	3.5	3.0

Trial Name	Threshold (Pa)	Omega	Frequency Content	Max Shear (Pa)	Average Shear Intensity (Pa)	Peak Shear Amplification	Avggerage Shear Intensity Amp
80_6H	0.27	17.01	0.26	0.95	0.80	3.5	3.0
80_7H	0.27	17.06	0.28	0.95	0.80	3.5	3.0
85_1L	0.34	15.78	0.41	0.84	0.56	2.5	1.7
85_2L	0.34	15.99	0.40	0.95	0.55	2.8	1.6
85_3L	0.34	15.88	0.42	0.86	0.55	2.5	1.6
85_4L	0.34	15.91	0.41	0.86	0.55	2.6	1.6
85_5L	0.34	15.89	0.42	0.88	0.55	2.6	1.6
90_1L	0.32	16.52	0.36	0.98	0.69	3.1	2.2
90_2L	0.29	16.65	0.34	1.00	0.80	3.4	2.7
90_3L	0.33	16.03	0.39	0.93	0.63	2.8	1.9
90_4L	0.31	16.39	0.37	0.97	0.73	3.1	2.3
90_5L	0.33	16.22	0.35	0.87	0.64	2.7	2.0
90_6L	0.32	16.39	0.36	0.93	0.70	2.9	2.2
94_1L	0.30	16.89	0.30	1.04	0.81	3.5	2.7
94_2L	0.31	16.13	0.38	0.93	0.72	3.0	2.3
94_3L	0.30	16.41	0.34	1.11	0.83	3.7	2.8
94_4L	0.30	16.77	0.32	1.05	0.84	3.6	2.8
94_5L	0.29	16.12	0.37	1.12	0.85	3.8	2.9
94_4H	0.27	17.17	0.24	1.07	0.97	4.0	3.6
94_5H	0.27	17.17	0.24	1.07	0.95	4.0	3.6
94_6H	0.27	17.18	0.24	1.06	0.96	4.0	3.6
94_7H	0.27	17.18	0.24	1.07	0.96	4.0	3.6

Trial Name	Probability of Exceedence	phi ()	phi (tables)	time (%)	rate of up-crossings (samples/s)	time of up-crossings (s)	mean clump size (samples)	mean duration of clump (s)
55_1L	11.5	1.20	0.885	11.30	22.61	6.78	23.00	0.12
55_2L	8.1	1.40	0.919	7.71	15.43	4.63	16.00	0.08
55_3L	7.4	1.45	0.926	7.18	14.36	4.31	15.00	0.08
55_4L	9.4	1.32	0.906	7.95	15.89	4.77	16.00	0.08
55_6L	11.1	1.22	0.889	8.85	17.70	5.31	18.00	0.09
60_1L	16.4	0.98	0.836	16.20	32.40	9.72	35.00	0.18
60_2L	16.1	0.99	0.839	15.70	31.40	9.42	35.00	0.18
60_3L	15.4	1.02	0.846	14.49	28.98	8.69	30.00	0.15
60_4L	15.2	1.03	0.848	14.65	29.30	8.79	30.00	0.15
60_4H	99.9	-14.96	0.001	100.00	200.00	60.00	625.00	3.13
60_5H	99.9	-16.58	0.001	100.00	200.00	60.00	650.00	3.25
60_6H	99.9	-15.90	0.001	100.00	200.00	60.00	650.00	3.25
60_7H	99.9	-15.66	0.001	100.00	200.00	60.00	625.00	3.13
60_8H	99.9	-14.83	0.001	100.00	200.00	60.00	625.00	3.13
65_1L	29.5	0.54	0.705	27.64	55.27	16.58	55.00	0.28
65_2L	30.9	0.50	0.691	28.09	56.18	16.85	60.00	0.30
65_3L	28.1	0.58	0.719	26.29	52.59	15.78	55.00	0.28
65_4L	29.1	0.55	0.709	27.23	54.47	16.34	55.00	0.28
70_1L	41.7	0.21	0.583	38.38	76.76	23.03	75.00	0.38
70_2L	41.3	0.22	0.587	37.01	74.02	22.21	75.00	0.38
70_3L	45.3	0.12	0.547	43.13	86.25	25.88	85.00	0.43
70_4L	42.1	0.20	0.579	40.80	81.59	24.48	85.00	0.43
70_5L	42.5	0.19	0.575	41.83	83.67	25.10	85.00	0.43
70_4H	99.9	-13.61	0.001	100.00	200.00	60.00	500.00	2.50
70_5H	99.9	-14.04	0.001	100.00	200.00	60.00	500.00	2.50
70_6H	99.9	-13.83	0.001	100.00	200.00	60.00	500.00	2.50
70_7H	99.9	-13.99	0.001	100.00	200.00	60.00	500.00	2.50
70_8H	99.9	-14.10	0.001	100.00	200.00	60.00	500.00	2.50
75_1L	53.9	-0.10	0.461	54.46	108.91	32.67	110.00	0.55
75_2L	52.4	-0.06	0.476	49.61	99.22	29.77	100.00	0.50
75_3L	53.9	-0.10	0.461	52.66	105.32	31.60	110.00	0.55
75_4L	52.8	-0.07	0.472	51.93	103.86	31.16	110.00	0.55
80_1L	84.4	-1.01	0.156	85.91	171.83	51.55	175.00	0.88
80_2L	68.8	-0.49	0.312	67.09	134.18	40.25	135.00	0.68
80_3L	65.2	-0.39	0.348	67.42	134.84	40.45	135.00	0.68
80_4L	66.3	-0.42	0.337	66.13	132.25	39.68	135.00	0.68
80_5L	69.8	-0.52	0.302	68.02	136.04	40.81	140.00	0.70
80_4H	99.9	-14.01	0.001	100.00	200.00	60.00	450.00	2.25
80_5H	99.9	-13.94	0.001	100.00	200.00	60.00	425.00	2.13

Trial Name	Probability of Exceedence	phi ()	phi (tables)	time (%)	rate of up-crossings (samples/s)	time of up-crossings (s)	mean clump size (samples)	mean duration of clump (s)
80_6H	99.9	-14.00	0.001	100.00	200.00	60.00	450.00	2.25
80_7H	99.9	-13.97	0.001	100.00	200.00	60.00	450.00	2.25
85_1L	99.2	-2.41	0.008	98.86	197.73	59.32	200.00	1.00
85_2L	99.4	-2.52	0.006	99.39	198.78	59.63	195.00	0.98
85_3L	89.9	-2.32	0.101	99.61	199.22	59.77	200.00	1.00
85_4L	91.1	-2.39	0.089	98.90	197.80	59.34	200.00	1.00
85_5L	91.1	-2.39	0.089	99.29	198.58	59.58	200.00	1.00
90_1L	99.9	-5.48	0.001	100.00	200.00	60.00	250.00	1.25
90_2L	99.9	-8.61	0.001	100.00	200.00	60.00	350.00	1.75
90_3L	99.9	-3.81	0.001	100.00	200.00	60.00	225.00	1.13
90_4L	99.9	-6.12	0.001	100.00	200.00	60.00	275.00	1.38
90_5L	99.9	-4.77	0.001	100.00	200.00	60.00	230.00	1.15
90_6L	99.9	-5.55	0.001	100.00	200.00	60.00	275.00	1.38
94_1L	99.9	-10.55	0.001	100.00	200.00	60.00	325.00	1.63
94_2L	99.9	-5.43	0.001	100.00	200.00	60.00	275.00	1.38
94_3L	99.9	-8.76	0.001	100.00	200.00	60.00	325.00	1.63
94_4L	99.9	-9.99	0.001	100.00	200.00	60.00	325.00	1.63
94_5L	99.9	-8.16	0.001	100.00	200.00	60.00	350.00	1.75
94_4H	99.9	-21.18	0.001	100.00	200.00	60.00	425.00	2.13
94_5H	99.9	-20.47	0.001	100.00	200.00	60.00	450.00	2.25
94_6H	99.9	-20.94	0.001	100.00	200.00	60.00	450.00	2.25
94_7H	99.9	-21.28	0.001	100.00	200.00	60.00	425.00	2.13

VITAE – Michael W. Horst

EDUCATION:

Current	The Pennsylvania State University - University Park, PA Ph.D. - Civil Engineering (water resources) <i>Focus:</i> Time Variation of Shear Stress Measurements at the Base of Rectangular Piers Advisor: Arthur C. Miller, Ph.D., P.E.
May 1999	M.Eng - Civil Engineering (water resources) Advisor: Arthur C. Miller, Ph.D., P.E.
May 1996	B.S. – Civil Engineering Minor – Environmental Engineering

TEACHING EXPERIENCE:

Fall 1999 - Current	The Pennsylvania State University – University Park, PA Lecturer: “Applied Hydraulic Engineering” (C.E. 362) Lecturer: “Introduction to Fluid Mechanics” (C.E. 360) Co-Lecturer: “Open Channel Hydraulics” (C.E. 462) Instructor: “Applied Fluid Mechanics Laboratory” (C.E. 363) Co-Instructor: “Engineering Hydrology” (C.E. 361) Teaching Assistant: “Waterways Engineering” (C.E. 465)
May 1998 - Current	Continuing Education Courses Basic Hydrology, Advanced Hydrology, HEC-1, HEC-HMS, HEC-RAS, Advanced Topics in HEC-RAS, Unsteady Flow Modeling using HEC-RAS

PUBLICATIONS:

- Johnson, P.A., Hey, R.D., Horst, M.W., Hess, A.J., “Aggradation at Bridges,” Journal of Hydraulic Engineering, February 2001, Vol. 127, No. 2, 154-157.
- Horst, M.W., and Miller, A.C., “Hydrologic Modeling Using GIS Applications,” Proceeding of the 2001 ASDSO Annual Conference, Snowbird, UT.
- Horst, M.W., and Miller, A.C., “Unsteady Flow Routing Utilizing HEC-RAS (3.0),” Proceeding of the 2000 ASDSO Annual Conference, Providence, RI.
- Horst, M.W., and Miller, A.C., “Uncertainty in the Variables Used to Calculate the PMF for Small Watersheds,” Proceedings of the 1999 ASDSO Annual Conference, St. Louis, MO.